Stony Brook University

Local Chemical and Nanostructural Properties of Rat Cortical Bone are Altered by Osteoporosis and Pharmaceutical Treatments

A Dissertation Presented

by

Alvin Samuel Acerbo

to

The Graduate School

in Partial Fulfillment of the

Requirements

for the Degree of

Doctor of Philosophy

in

Biomedical Engineering

Stony Brook University

August 2012

Stony Brook University
The Graduate School

Alvin Samuel Acerbo

We, the dissertation committee for the above candidate for the

Doctor of Philosophy degree, hereby recommend

acceptance of this dissertation.

Lisa M. Miller, PhD - Dissertation Advisor
Adjunct Assistant Professor, Department of Biomedical Engineering

Stefan Judex, PhD - Chairperson of Defense
Professor, Department of Biomedical Engineering

Helmut Strey, PhD
Associate Professor, Department of Biomedical Engineering

G. Lawrence Carr, PhD
Physicist, Photon Sciences, Brookhaven National Laboratory

This dissertation is accepted by the Graduate School

Charles Taber
Interim Dean of the Graduate School

Abstract of the Dissertation

Local Chemical and Nanostructural Properties of Rat Cortical Bone are Altered by Osteoporosis and Pharmaceutical Treatments

by

Alvin Samuel Acerbo

Doctor of Philosophy

in

Biomedical Engineering

Stony Brook University

2012

The tissue level mechanical properties of bone are a product of bone quantity and quality. Although bone quantity is easily defined, bone quality is much harder to define as it includes contributions from both bone chemistry and structure. This study investigated the chemical and nanostructural properties of rat cortical bone in order to determine how they are altered by osteoporosis and subsequent pharmaceutical treatments, including sodium fluoride, alendronate and parathyroid hormone. As part of this study, reflection-based Fourier Transform Infrared Microspectroscopy was developed to enable spatially resolved imaging of the chemical properties of bone specimens in the form of polished blocks. In addition, simultaneous microbeam Small and Wide Angle X-ray Scattering mapping was developed to investigate the collagen orientation, degree of orientation, *D*-spacing, and the apatite crystal geometry in bone specimens. Results from cortices of rat femurs showed that tissue mineralization and mineral crystallinity differed between intracortical and circumferential bone on both endosteal and

periosteal surfaces, but no differences in nanostructural properties between these two types of bone were found. In osteoporotic bone, greater differences in mineralization and carbonate substitution were observed between intracortical and periosteal bone. Additionally, the collagen fibrils in intracortical bone were found to have an unusually high alignment and changes were found in the geometry of the mineral crystals of newly formed periosteal bone. Upon treatment with sodium fluoride, newly formed bone had greater carbonate substitution and crystallinity of apatite compared to osteoporotic bone, suggesting that sodium fluoride affects the rate of mineral maturation in newly formed bone. Changes to the collagen alignment induced by osteoporosis were mitigated by sodium fluoride and alendronate, but not by parathyroid hormone. However, both alendronate and parathyroid hormone mitigated alterations to the crystal geometry. Together, these results show that osteoporosis and pharmaceutical treatments affect the chemical composition and nanostructural properties of rat cortical bone. A further understanding between the interplay of the parameters that define bone quality, the ultimate tissue level mechanical properties, and fracture resistance of bone may lead to more potent pharmaceutical drugs to recuperate compromised bone quality.

TABLE OF CONTENTS

LIST OF FIGURES

LIST OF TABLES

LIST OF ABBREVIATIONS

Aln	Alendronate
BMD	Bone mineral density
BNL	Brookhaven National Laboratory
BSE	Backscatter Electron Imaging
CT	Computed Tomography
CTRL	Control
DDE	Dynamic Data Exchange
DXA	Dual X-ray Absorptiometry
EM	Electron Microscopy
FAP	Fluoroapatite
FTIRI	Fourier Transform Infrared Imaging
FTIRM	Fourier Transform Infrared Microspectroscopy
FPA	Focal Plane Array
FWHM	Full Width at Half Max
GGPP	Geranylgeranyl Diphosphonate
GISAXS	Grazing Incidence Small Angle X-ray Scattering
GPa	Gigapascal
HAP	Hydroxyapatite
HDF	Hierarchical Data Format
IL-6	Interleukin-6
IR	Infrared
KK	Kramers-Kronig
MCT	Mercury Cadmium Telluride

NaF	Sodium Fluoride
NI	Nanoindentation
NSLS	National Synchrotron Light Source
MVA	Mevalonate
OI	Osteogenesis Imperfecta
OVX	Ovariectomy
OPG	Osteoprotegrin
PDO	Projected Degree of Orientation
PMMA	Poly Methyl Methacrylate
PO	Projected Predominant Orientation
PSF	Point Spread Function
PTH	Parathyroid hormone
PTHrP	PTH related Proteins
qBSE	Quantitative Backscatter Electron Imaging
RANK	Receptor Activator of Nuclear Kappa-β
RANKL	RANK Ligand
ROI	Region of Interest
SAXS	Small Angle X-ray Scattering
SEM	Scanning Electron Microscopy
SSRL	Stanford Synchrotron Radiation Laboratory
TEM	Transmission Electron Microscopy
TXM	Transmission X-ray Microscopy
VOI	Volume of Interest
WAXS	Wide Angle X-ray Scattering

ACKNOWLEDGMENTS

I would like to thank my advisor, Dr. Lisa Miller, for giving me the chance to work under her guidance in a world class laboratory. Her knowledge and experience in the field of IR microspectroscopy have inspired me to pursue scientific research and to become a scientist. I would like to thank my committee for providing critical insight and help over the course of my project. Specifically, I would like to thank Dr. Stefan Judex for his insight and suggestions related to experimental design and the statistical aspects of all data analysis, Dr. Helmut Strey for his suggestions on how to prepare samples and analyze the data from the Small and Wide Angle X-ray Scattering experiment, and Dr. Larry Carr for countless conversations and help in the development of reflection-based FTIR but also for teaching me the fundamentals of synchrotron physics and Infrared spectroscopy.

I would like to thank my colleagues Dr. Steve Tommassini and Andrea Kwaczala for their help in preparing the dozens of samples for IR analysis and also scanning them during the many and long weekends and nights at beamlines U2b and U10b. Operating such a complex machine has been a learning process for us all and has not been without hiccups. Your help and patience are truly appreciated.

The help and support of my lab mates has been endless. I would like to thank Randy Smith for his help, encouragement, new ideas and training from the day I joined the lab, Imke Bodendiek and Meghan Faillace for teaching me various essential laboratory techniques, Andreana Leskovjan, Megan Bourassa, Paul Gelfand, Eli Stavitski, Ryan Tappero, and Ruth Pietri for their encouragement and support, and my summer students Sarah Heins, Natalie Delpratt, and Genevieve Kuczewski for their help with IR data analysis. Thanks also to my lab

mate and friend Matthew Engel with whom I spent countless hours studying for exams, and who introduced me to my advisor doctoral Lisa Miller.

I would like to thank countless individuals that keep the equipment running at the National Synchrotron Light Source, the Advanced Photon Source and the Stanford Synchrotron Radiation Lightsource: Lin Yang at NSLS beamline X9, Ryan Tappero and Tony Lanzirotti at NSLS beamline X27A, Francesco De Carlo at APS beamline 2-BM, and Joy Andrews Hayter and Piero Pianetta at SSRL beamline 6-2c. Thanks to Shu Cheung for crafting the IR sample holder and to the machine operators of all three user facilities for providing a stable synchrotron beam.

Finally, I thank my family and friends for being there for me and encouraging me through this challenging process. To Greet (mom) and Sam (dad), thank you for inspiring from my early days to reach the top and that nothing is impossible, and to my girlfriend Cindy Dauria for her endless care and love. Without you, I would surely not have been where I am now. I am tremendously fortunate to have you in my life.

PUBLICATIONS

Acerbo, A. S., Carr, G. L., Judex, S., & Miller, L. M. (2012). Imaging the material properties of bone specimens using reflection-based infrared microspectroscopy. *Anal Chem, 84*(8), 3607-3613.

Bhatia, A., Albazzaz, M., Espinoza Orias, A. A., Inoue, N., Miller, L. M., **Acerbo, A. S.**, et al. (2012). Overexpression of DMP1 accelerates mineralization and alters cortical bone biomechanical properties in vivo. *J Mech Behav Biomed Mater, 5*(1), 1-8.

Tommasini, S. M., Trinward, A., **Acerbo, A. S**., De Carlo, F., Miller, L. M., & Judex, S. (2012). Changes in intracortical microporosities induced by pharmaceutical treatment of osteoporosis as detected by high resolution micro-CT. *Bone, 50*(3), 596-604.

Acerbo, A. S., & Miller, L. M. (2009). Assessment of the chemical changes induced in human melanoma cells by boric acid treatment using infrared imaging. *Analyst, 134*(8), 1669-1674.

CHAPTER 1

INTRODUCTION

1.1 The current state of medical diagnosis of compromised bone quality

Bone tissue is a specialized support tissue characterized by its hardness and rigidity, and together with cartilage makes up the skeletal system. Bone tissue serves several major functions: 1) mechanical and structural support for the shape of the body and compartmentalization for organs, as well as sites for muscle attachment for locomotion; 2) protection of vital organs, joints and bone marrow; 3) storage and regulation of calcium and phosphate ions; and 4) production of blood cells and platelets [1].

Due to the hierarchical structure that exists in bone, the material, mechanical and structure properties of bone may differ depending on which structural level these properties are investigated at. At the anatomical level, bone has a specific morphology and is composed of different tissue types (Figure 1-1). These tissues vary in degree of mineralization and are composed of a variety of combinations of organic and inorganic components. In addition, tissues may have specific planar or three-dimensional layered structures, all of which give rise to different mechanical properties. Material, mechanical and structural differences also exist at the length scale of proteins and mineral crystals, further emphasizing that those macroscale properties may not be directly proportional to microscale and nanoscale properties.

Osteoporosis is a disease characterized by reduced bone matter per square centimeter of bone, a deterioration of the bone microarchitecture and increased bone fragility and fracture risk.

In the US alone, osteoporosis affects more than 10 million people and is responsible for more than 2 million fragility fractures annually, leading to an annual cost of more than $17 billion [2, 3]. Osteoporosis arises from an imbalance between bone deposition by osteoblasts and bone resorption by osteoclasts. Amongst the risk factors involved in this imbalance are aging, estrogen deficiency in postmenopausal women [4], and malnutrition [5], but also genetic and modifiable factors such as Cushing's disease and glucocorticoid-induced osteoporosis, respectively [6].

Although estimating the risk of bone fracture centers on the assessment of bone mass and quality, few clinical tools exist for measuring bone quality [7], the factors that ultimately give rise to the mechanical behavior of bone tissue. As such, the current standard for determination of bone fracture risk is by the measurement of bone mineral density (BMD) using dual x-ray absorptiometry (DXA) [8]. Although DXA is widely used for the measurement of BMD, it has been recognized that this method of determining BMD is a poor indicator of bone mineral density and future fracture risk, as the BMD of adolescent and elderly persons may be similar while the fracture risk in the elderly is higher [9, 10]. Further, a bone without and a bone with a previous fracture may have similar BMD, but the latter will have an increased fracture risk. Due to the low detection rate and high rate of false positives, BMD alone should not be used as an indicator of fracture risk [11].

While BMD is a poor but commonly used predictor of fracture risk, less is known about how the organic and inorganic bone matrix define bone quality [12, 13], although their importance is understood and research in this field is active. For example, microdamage of bone is thought to rupture the collagen cross-linking structure, but an exact mechanism of how this occurs remains unclear [14]. Furthermore, it has been determined that the successive levels of structural hierarchy of bone decouple under high load, and this is thought to act as a load sharing

mechanism [15]. For example, low loads are mostly absorbed by the macro scale structure of bone, while at higher loads also the micro scale structure of bone is affected. However, it is not known how this mechanism is affected by alterations in bone chemistry and nanostructure. A better understanding of the mechanisms of bone microdamage and load sharing are just a few examples that may provide complementary information to BMD and together a more accurate description of bone quality and thus fracture risk.

1.2 The hierarchical structure of bone

Macrostructure

Anatomically, two general types of bones exist in humans. Flat bones are predominantly found in the skull and serve as a protective barrier to vital organs, while long bones are typically more cylindrical and primarily serve to bear skeletal loads. Long bones consist of the epiphyses at the two extremities, the diaphysis in the middle, and the metaphysis between them, which serves as the developmental zone [16]. The physical dimensions of bone, such as the external diameter and cortical thickness, are major contributors to bone strength. Although the geometric properties of long bones contribute to bone strength [17], assessment of mechanical function cannot be solely based on size and shape: bone material composition is also a contributor to bone strength [18].

In both types of bone, the cortex is the outer layer of bone and forms a dense layer of calcified tissue. The internal space surrounded by cortical bone tissue is filled by the more porous and softer trabecular bone: a network of thin trabeculae filled with bone marrow, osteoblasts, osteoclasts, fibroblasts, adipocytes, and macrophages, where the production of blood

cells and platelets occurs [19]. Although both types of bone are composite materials of mineral and organic matrix at a ratio of 1:3 by weight, several factors play a role in defining the exact structure and composition of bone, such as skeletal site, age, sex and mechanical loading [20]. Trabecular bone is structurally different from cortical bone, and is composed of an interconnecting framework of rod- and plate-like structures known as trabeculae.

Trabecular bone in humans is composed of boney trabecular struts of 100 - 200 μm in diameter and marrow filled cavities of 1 mm in diameter. Trabecular bone has a higher surface-to-volume ratio, is metabolically more active and generally has a higher turnover rate than cortical bone, and is therefore younger on average than cortical bone [21]. Consequently, the rates of response to changing environmental factors and also the material properties of trabecular and cortical bone may differ, such as a higher level of mineralization in cortical bone and the presence of small pores (5 - 100 μm^3) and lacunae (100 - 1000 μm^3) in cortical bone [22]. The difference in composition and architecture in turn results in different mechanical properties of cortical and trabecular bone tissues [23]. While the presence of porosities and the degree of tissue mineralization have a marked affect on the mechanical properties of cortical bone, several other factors influence trabecular bone strength, such as trabecular width and connectedness [24]. Thus, any differences in mechanical properties between cortical and trabecular bone tissues cannot be attributed to differences in tissue mineralization, mineral density, or pore structure alone [25]. In fact, cortical and trabecular bone can be considered mechanically different materials [26].

Microstructure

At the microlevel, human cortical bone is structurally composed of concentric sheets of collagen fibers that form osteons, or Haversian systems (Figure 1-1). These structures lay parallel to the long axis of bone and have a diameter of 200 - 250 μm. The collagen sheets are typically referred to as lamellae, and they have a thickness of 5 - 10 μm. A Haversian canal located centrally in the osteons contains and protects blood vessels and nerve fibers, while Volkmann's canals run perpendicular and connect Haversian canals with neighboring osteons. Besides concentric lamellar layers, additional interstitial lamellae exist between Haversian systems [27].

The process of remodeling in cortical bone is similar to the excavation of a tunnel: Bone resorption by osteoclasts creates tunnels called Haversian canals in existing cortical bone tissue. In the subsequent step, osteoblasts line the inside walls of the canal with a layer of cement and a secondary lamellar layer. This process repeats and gives rise to the onion-like cross-section [20, 28]. The orientation of adjacent lamellar layers is thought to alternate such that one layer is longitudinal along the Haversian system, while the next is transverse.

The mechanical function of the concentric arrangement of lamellar layers in Haversian systems is not fully understood, although mathematical modeling suggests that the cylindrical shape and size of Haversian systems might aid in repair of fractures. In contrast to perfectly flat and parallel lamellar layers, a fracture in a Haversian system is more likely to result in two attached halves, or at least two fracture points in close proximity, such that the Haversian structure is better retained, thereby facilitating the repair process [29]. Besides the concentric and

interstitial arrangement of lamellar layers in cortical bone tissue, each lamellar layer is composed of five sub layers [30].

Trabecular bone consists of rod-like trabeculae with a diameter of 50 - 300 μm and larger plate-like trabeculae which are arranged into a three-dimensional structure (Figure 1-2). Although structurally less complex than cortical bone, determination of the mechanical properties of trabecular bone is equally complex as it is modulated by several architectural and material parameters. Since trabecular bone is metabolically more active and has a higher turnover rate, the material, geometric and mechanical properties of trabecular bone are affected by disease much sooner than cortical bone. Fortunately, due to the relatively large size of individual trabeculae, studying them in isolation is possible.

Studies have been performed to elucidate the mechanical properties of trabecular bone tissue [31-33] and the rod-like (Figure 1-2B) and plate-like (Figure 1-2C) trabecular components [34]. Although reported values for elastic moduli span a wide range (1 - 20 GPa), trabecular plates are shown to have a much greater contribution to bone's elastic behavior than trabecular rods [35]. Furthermore, investigations of the effects of bone loss on the volume fraction of these trabecular components suggest that a reduction in bone volume fraction reduces the number of plates and their thickness, while increasing the number of trabecular rods [36].

Nanostructure

The nanoscale structure of bone matrix comprises of 300 nm long and 1.5 nm wide Type I triple helix collagen fibrils which lay parallel in staggered array (Figure 1-3). Hydroxyapatite platelets are intertwined in 40 nm gaps between successive collagen fibrils. The dimensions of these intrafibrillar mineral platelets are 30 - 50 nm long and 1.5 - 2 nm thick, depending on the

degree of mineralization. Typically, the mineral phase is oriented along the collagen plane. The semi-crystalline aggregates of collagen and mineral form collagen fibrils that are typically 50 - 500 nm wide and coated with hydroxyapatite platelets [37, 38]. The next higher level of organization consists of bundles of fibrils that form collagen fibers with a width in the micron range. The organic matrix of bone is composed of mainly collagen and is thought to be a major contributor to bone's tensile strength through collagen cross-link formation [39]. The inorganic matrix of bone is composed of hydroxyapatite mineral, and develops once the collagen matrix has matured [40]. To date, the relationship between nanostructure and both micro- and macro-mechanical properties is largely unknown as well as how osteoporosis treatments affect these properties.

Cortical bone exhibits regional variations in the degree of orientation and direction of collagen fibers, which may represent biomechanical adaptations to different types of mechanical loading (e.g. tension, compression and shear). It has been suggested that a longitudinally oriented collagen matrix is more closely related to tension, while transverse collagen is more closely related to compression forces [41]. The relationship between collagen fiber orientation and mechanical properties further suggests that collagen fiber orientation, followed by mineral density and mineralization, ranks highly as a predictor of the bending properties of bone (e.g. energy absorption), but is less influential on elastic modulus and bone strength where mineral density and tissue mineralization account for more of the observed variability [42-44]. Collagen has also been found to be preferentially oriented with a high degree of orientation parallel to the periosteal surface of newly formed bone. The orientation and degree of orientation of collagen in older bone was found to be irregular, with clusters of collagen (in a 100 x 100 μm area) showing a much higher degree of orientation than seen in newly formed bone [45].

In a study of mineral crystal size in varying degrees of mineralization, it was found that lightly mineralized tissue exhibits a broader distribution but smaller mineral crystal thickness while more mineralized tissues contain thicker mineral crystals with a smaller distribution. The more uniform size in mineralized tissue is due to better packing and alignment of the crystals between to collagen gaps. As mineralization increases, it was found that the spacing between collagen layers also decreased, suggesting a more densely packed collagen matrix [38].

The hierarchical structure of the bone, specifically the fibril array pattern and the mineralized collagen fibers, have been shown to act as a load sharing mechanism for external stress. Under high levels of external stress, it was found that the total stress is decoupled amongst the different hierarchical layers, effectively preventing excessive stress on individual layers. The stiff mineralized fibrils deform under high stress and transfer the stress to neighboring fibrils by shearing. Individual fibrils take up strain by deformation of the collagen fibers and mineral platelets [15, 46, 47].

1.3 Osteoporosis and treatment options

Osteoporotic bone is defined by reduced bone mass [24, 48] and has been correlated with reduced bone strength [17]. A reduction of bone volume has been observed in both cortical and trabecular tissues, with an observed thinning of the cortical shell and a reduction of trabecular architecture most notably in the lumber spine [49, 50]. Further evidence suggests that additional factors are needed to fully characterize this disease. Nonetheless, the effects of reduced bone mass alone on the mechanical properties of cortical bone tissue are marked: fracture toughness is significantly reduced and crack bridging in the wake of a crack is also reduced [51]. In aging of human bone, bone remodeling in the Haversian system eventually leads to a thinning of the

cement lines between lamellar layers, creating a prime site for microcrack formation. Furthermore, the continuous remodeling of cortical bone also increases osteons density and thus also microcrack density. These mechanical changes are directly related to a reduced fracture resistance in bone [20].

A study of the trabecular bone architecture in healthy and osteoporotic bone found that the bone volume fraction, trabecular number and connectedness were lower in osteoporotic bone, although no differences in trabecular thickness were observed [52]. Also the elastic modulus and hardness were found to be lower in osteoporotic bone, consistent with the decrease in bone volume fraction and deteriorated trabecular architecture. It was also found that fractured bone specimens had a more anisotropic trabecular structure parallel to the load axis, suggesting that deterioration was primarily in the transverse axis. An earlier study suggests that architectural deterioration of trabecular bone involves the progressive enlargement of the perforations between trabeculae and the reduction of plates into rods, ultimately leading to a lowered elastic modulus and hardness of trabecular tissue [53].

Several treatment options exist that attempt to remedy the effects of low bone mass and rapid bone loss. These treatments can be sorted into three categories based on their mode of action. Antiresorptive agents such as bisphosphonates and estrogens work by decreasing bone resorption and bone formation, leading to an overall increase in mineralization levels while maintaining the architectural integrity of the bone structure. Anabolic agents such as parathyroid hormone work by increasing primarily bone formation, thus increasing bone mass and strengthening bone architecture. However, the high rate of new bone formation results in a greater fraction of younger bone, thereby decreasing the degree of mineralization which typically goes paired with reduced hardness and increased elasticity of the new tissue. In the third category fall dual acting

agents, such as strontium ranelate, which both reduce bone resorption and increase bone formation, resulting in an increase in bone architecture while maintaining mineralization levels [54]. A combination treatment of anabolic and antiresorptive agents can be used to reduce the resorptive effects of powerful anabolic agents, thereby further increasing bone mass. In summary, these drug treatments have profound effects on bone mass, architecture, and material properties, such as mean age and mineralization.

A major target pathway for maintaining or adjusting bone metastases is the receptor activator of nuclear factor kappa-β ligand (RANKL) pathway, which plays a dominant role in the differentiation, activation and survival of osteoclasts. Parathyroid hormone (PTH) and related proteins (PTHrP) play a leading role in this pathway by binding to PTH receptors on inactive osteoblasts and thereby activate them. Although the activated osteoblasts stimulate bone growth, they also increase production of RANKL, which interacts with the RANK receptors on hematopoietic osteoclast precursors, differentiating them into mature and active osteoclasts. These mature osteoclasts subsequently resorb bone and cause the release of minerals and growth factors such as interleukin 6 (IL-6) and PTHrP, which are related to tumor cell and bone growth. Osteoblast activity also increases the production of osteoprotegerin (OPG), which can bind to and inhibit RANKL [55]. Although overproduction of RANKL is associated with bone loss, OPG has been shown to prevent bone loss associated with overexpression of RANKL. The RANKL/OPG ratio is thus an important factor in maintaining normal bone mass, and several treatment options involve increasing OPG resulting in anti-resorptive effects [56]. This can be accomplished by administering OPG directly, or by activating the Wnt/β-catenin signaling duo, which directly regulate the expression of OPG by osteoblasts. An added advantage of the latter

approach is that activation of Wnt and β-catenin signaling in mesenchymal cells controls their differentiation into osteoblasts and also controls bone formation. [57].

The body naturally produces parathyroid hormone (PTH) in the parathyroid glands in response to low levels of serum Ca^{2+}. This soluble protein binds to and activates osteoblasts and also results in the formation of mature, active osteoclasts that in turn dissolve bone mineral and restore calcium homeostasis. [58]. Besides osteoclast differentiation being a principle target of PTH, intermittent use of PTH has been proposed to increase osteoblast numbers, and thus bone formation, in several stages. Increased osteoblastogenesis is achieved by specific differentiation of multipotential mesenchymal stem cells into osteoblasts by the expression of the transcription factors Runx2 and osterix. Inhibition of osteoblast apoptosis is also a critical determinant of osteoblast number and is mediated through intermittent PTH treatment, but the efficacy of this mechanism is highly dependant on the duration of PTH treatment. PTH treatment has also been proposed to reactivate the matrix synthesizing function of quiescent bone lining cells [59]. Combined, these effects of intermittent PTH treatment may increase osteoblast numbers beyond what is needed to replace bone removed by osteoblasts during remodeling. Indeed, PTH has been found to affect both cortical bone and trabecular bone. An increased cortical thickness has been demonstrated, which in itself is predicted to significantly contribute to bone strength [49]. Further, increased connectedness in trabecular bone has been found, although the implications for bone strength remain unknown [60]. Anti-resorptive co-therapy has been proposed to further block the catabolic effects of intermittent PTH treatment, but the use of several bisphosphonates dulled the effects of PTH. Instead, combined treatment with OPG has shown success in increasing bone volume [56]. At the nanoscale, studies of intermittent PTH treatment suggest that the collagen and mineral composition is newly formed bone tissue is normal; thus the size

and thickness of mineral crystals and collagen alignment were not significantly different from normal bone tissue [61].

Clinically useful synthetic analogs of the inorganic pyrophosphates come in the form of bisphosphonates with structurally different side chains which give these drugs their potency. Although bisphosphonates suppress bone formation by inhibiting mineralization, they are also potent inhibitors of osteoclast-mediated bone resorption and thereby effectively reduce bone turnover [62]. The very high potency of the nitrogen-containing bisphosphonate alendronate is conveyed by the four-carbon amino side chain. Alendronate and other bisphosphonates are thought to act on the isoprenoid biosynthesis pathway from mevalonate (MVA) to geranylgeranyl diphosphonate (GGPP), which is essential to the production of steroids such as cholesterol, and are selectively taken up by osteoclasts during bone resorption [63]. Alendronate has been shown to prevent protein prenylation in the J774 macrophage cell lineage by specifically inhibiting farnesyl disphosphate synthase in the MVA pathway. This interaction disrupts proper cytoskeletal function and vesicular trafficking in osteoclasts, eventually leading to apoptosis [64]. The strong inhibition of bone resorption by alendronate treatment more than offsets the suppression of bone formation and thereby increases bone mass, which has been shown to reduce the risk of osteoporotic fractures. The antiresorptive action of alendronate affects trabecular bone by increasing the uniformity and overall degree of mineralization, most likely because a greater fraction of trabecular matrix reaches higher levels of calcium content. Alendronate also affects cortical bone by decreasing remodeling activity within osteons, thereby leading to a decrease in cortical porosity [65]. This strengthening of the cortical shell is thought to increase antifracture effectiveness [66]. Alendronate has not been found to alter the

nanostructure of bone; the size and thickness of mineral crystals as well as the collagen and mineral matrix are not affected [67].

Although fluoride is not clinically used to treat osteoporosis, it is widely used in research clinics and its effects are well documented. Fluoride stimulates bone formation and has been shown to markedly increase bone volume, primarily by increasing trabecular thickness. However, this restoration in skeletal mass does not lead to a comparable decrease in fracture risk, presumably due to the high incorporation of fluoride into bone and fluoride-associated osteomalacia [68]. Fluoride is the least well understood stimulator of bone formation, but several mechanisms have been proposed by which fluoride achieves increased bone formation and osteoblast number, while not affecting bone resorption. Most of these mechanisms implicate the entry of fluoride into osteoblasts and activation of the Ras-Raf-MAPK signaling transduction pathway, leading to increases in osteoblast proliferation and activity [69]. At the nanoscale, fluoride treatment has been shown to increase the average thickness of mineral crystals as well as change the structure of the collagen and mineral matrix [67]. Presumably, the fluoride ion is incorporated into bone during mineralization, and increases the stability of the mineral lattice but decreases solubility of the mineral crystals. As such, fluoride tends to accumulate in areas where mineralization is highest [70].

1.4 Assessment of bone material properties

Bone mineral density

Dual energy x-ray absorptiometry (DXA) is a widely used technique for the measurement of bone mineral density (BMD). In a DXA measurement, the differential absorption of

monochromatic x-rays is measured and volumetric bone density is calculated for different regions of bone [71]. DXA is clinically used as a predictor of bone fracture risk, although BMD is not the only factor involved in bone strength. Although DXA has high sensitivity, it suffers from low specificity. A normal BMD does not exclude the possibility of fracture; it merely indicates a decreased risk. Conversely, a low BMD does not guarantee fracture, but rather indicates that fracture is more likely [8].

Macro-mechanical material properties

Although the mechanical performance of whole bones is of great interest to researchers and clinicians, the wide range in geometric shapes of bones (e.g. hip is irregular shaped while femur is long) and the range in material properties and distribution thereof across a single bone make the measurement of whole bone performance complex. Such measurements have been performed in vivo on human tibia using implanted strain gauges, but only during moderate and vigorous exercise activities such as walking, running, and jumping [72, 73]. More rigorous and controlled macro-scale mechanical tests can be used to replicate and measure the resistance to compressive, tensile and torsional forces that are exerted on bones on a daily basis [74]. The commonly used three-point bending test generates both compressive and tensile forces. By placing the bone specimen on two holders at both ends, and applying a force at the midpoint the top half of the specimen will undergo compression, while the bottom half will undergo tension. The stress and strain at any point in the specimen along the long axis can be determined. Typically, the load is increased until a break forms in the bone specimen [75]. Torsional testing is accomplished by anchoring both ends of the specimen (e.g. by firmly embedding) and applying a torque to one end while measuring the load and angular deformation to determine the shear modulus [74].

Micro/Nano-mechanical material properties

In nanoindentation, an nm-sized tip is used to probe the mechanical properties of surfaces as small as a few square nanometers. Due to the hierarchical structure of bone as well as the fineness of the interface between the different components of trabecular and cortical bone, nanoindentation is a particularly attractive technique for measuring the mechanical properties of micron-sized components in bone tissues. Characterization of the mechanical behavior of bone at the submicrostructural level allows for the characterization of material properties of individual lamellae and osteons [9].

During the loading phase a nanoindentation, the indenter tip is brought into contact with the sample surface and a constantly increasing force is applied while displacement into the sample is measured (Figure 1-4). After a preset force threshold is reached, the applied force is held constant and further displacement into the sample is measured. During the unloading phase, the applied force is constantly brought back to zero, and again displacement into the sample is measured. In the most common method of calculating hardness H and the modulus E from the load-displacement data, the Oliver-Pharr method [76], deformation during the loading phase is assumed to be both elastic and plastic since permanent hardness impressions form in the material. The unloading phase is assumed to be purely elastic and is used for analysis of material mechanical properties.

A typical elastic-plastic analysis of load-displacement data, such as the Oliver-Pharr method, results in the contact hardness H_c and strain modulus E' [77]. The hardness H is a measure of how resistant solid matter is to permanent deformation when a force is applied, while the elastic modulus E is a measure of a material's tendency to be deformed elastically. It has been noted

that contact hardness is not independent of the elastic modulus in mineralized tissues [10], and is in fact a good predictor of elastic modulus. Furthermore, hardness has been shown to be a good predictor of ultimate stress, the point at which material failure occurs [78] over a range of mineralizations, which makes hardness an indicator to bone strength.

Chemical properties

Using an IR light source, an IR detector and an interferometer, IR spectra are readily obtained that can give qualitative and quantitative information about the chemical makeup of bone specimens. Although in chemically complex specimens such as bone tissue, several absorption bands in an IR spectrum often overlap, giving rise to a complex absorption feature. An absorption feature may consist of as many as 5 absorption bands. Integrations are therefore often performed on absorption features, but will still give relevant information about specific chemical groups. A more careful definition of these integration ranges, based on specific constituents of the absorption features, may further distinguish between chemical groups, for example phosphate into stoichiometric and non-stoichiometric phosphate. In the case of mineralized bone tissues, several specific chemical parameters have been defined, including collagen cross-linking, tissue mineralization, carbonate substitution into the apatite lattice, and mineral crystallinity.

Because of these developments, Fourier Transform Infrared Imaging (FTIRI) has become a widely used technique for spatially resolving the chemical composition of a variety of mineralized specimens, including bone and tooth [79-81]. Several of these investigations have focused on how bone diseases and pharmaceutical treatments affect bone chemistry [82, 83], but also how bone chemistry varies with the type of bone [81] and age [84, 85]. A higher spatial

resolution analysis of the level of tissue mineralization of circumferential lamellae and osteons using FTIR pointed out that these two types of bone mineralize at different rates and to different endpoints. Raman spectroscopy, which relies on the inelastic scattering of a laser source focused on the sample surface, has also been successfully used to probe various chemical parameters related to bone quality. For example, the high spatial resolution that can be achieved with Raman spectroscopy readily facilitates the chemical characterization of individual lamellar layers in osteons [86], while an other study using whole, wet and bones demonstrates that Raman spectroscopy can be used on dried and wet samples alike [87, 88].

A commonly used technique to determine tissue mineralization uses the mean atomic number as measured by backscattered electron imaging (BSE) of a highly polished, flat surface of bone [89]. The typical spatial resolution that can be achieved is around 1 μm, and data acquisition rates when combined with a scanning electron microscope (SEM) surpass IR spectroscopy. The application of BSE on bone block surfaces can be combined with other surface techniques, such as nanoindentation [90]. Additionally, the use of a mineral standard allows quantitation of the data (quantitative backscatter electron imaging, or qBSE), and thus tissue mineralization levels. In an analysis of Osteogenesis Imperfecta (OI), it was found that average mineralization densities were greater compared to age- and site-matched controls, and that mean mineralization density was correlated with disease severity [91].

Microstructural properties

It is widely accepted that changes in bone structural characteristics lead to changes in bone mechanical properties. Structural parameters such as connectedness of the trabecular structure and cortical porosity are readily assessed using 3D computed micro-tomography (μCT). A μCT

system uses a microfocused x-ray beam as a source and rotates the sample relative to the x-ray source. Attenuation of x-rays by the specimen at various angles is detected by reading out the surviving x-ray photons by a planar 2D detector. A 3D dataset (volumetric) is then constructed from the 2D slices with a voxel size as small as 10 μm^3 in clinical use. Segmentation of μCT data is required to classify what type of tissue each pixel belongs to and is critical to accurate quantification of architectural parameters [92]. Bone volume, cortical density and porosity as well as trabecular thickness and connectedness can be measured with μCT [93]. More recently, synchrotron-based nanoCT has been used to investigate the micron sized porosities in different regions of the cortical shell, in order to determine how their occurrence and size distribution are altered by common osteoporotic treatments. NanoCT has also been used to visualize vascular channels and osteocyte lacunae at micron resolution [94].

Nanostructural properties

Although the mineral and organic phases of bone follow a highly ordered pattern, small deviations in this spatial organization may be observed using x-ray scattering and diffraction techniques. A planar 2D detector is used to capture the angle and orientation of inelastic scattered x-rays from a sample. From the angle and orientation, the projected spatial organization of certain features in the material can be reconstructed. In fact, the angle of the scattered x-ray is proportional to the size of the feature that caused the scattering. As such, the angular range of the detector, denoted as the q-range, dictates the range of feature sizes that may be detected. The typical angular range for SAXS measurements can accommodate measurements of 10 to 100 nm sized features, while SAXS measurements resolve features with a size of 0.1 to 10 nm. The spatial organization of the collagen phase can be determined from the SAXS pattern. This

includes the projected orientation and degree of orientation of the collagen phase, as well as the *D*-spacing. The WAXS pattern may be used to elucidate more details regarding the mineral phase, including parameters such as the crystal lattice spacing, crystal length, width, thickness, deformity and crystallinity. Simultaneous SAXS and WAXS data collection is a particular powerful combination as one can learn from both the mineral and organic phases at a single location.

Transmission X-ray microscopy (TXM) can be used to visualize the micro- and nanostructure of bone thin sections at a high spatial resolution (30 - 40 nm) defined by the size of the incident beam, focusing optics, and effective pixel size of the detector. Three-dimensional tomography can be performed to more accurately visualize these structures in relatively thick sections of bone tissue (>50 μm). At this spatial resolution, small vascular networks (canalicular networks) are evident, and the rod- and plate-like components of trabecular bone can visualized. An appropriate absorption standard can be used to approximate mineral density in the tissue [95].

One of the highest spatial resolution imaging techniques (>2 nm) for direct imaging of mineral crystal shape, size and orientation in intact bone, is transmission electron microscopy (TEM). This technique typically requires ultrathin bone sections (<1 μm), and been used to accurately measure mineral crystal geometry in normal and diseased bone tissue as well [96]. In addition, the orientation of collagen fibrils can be visualized with respect to the mineral crystal geometry and orientation to determine if any patterns exist, such as circularly oriented or parallel, ordered layers. Additionally, high spatial resolution allows for direction imaging of the bone-hydroxylapatite interface [97], which can be useful for analyzing the interface between bone and a coated implant.

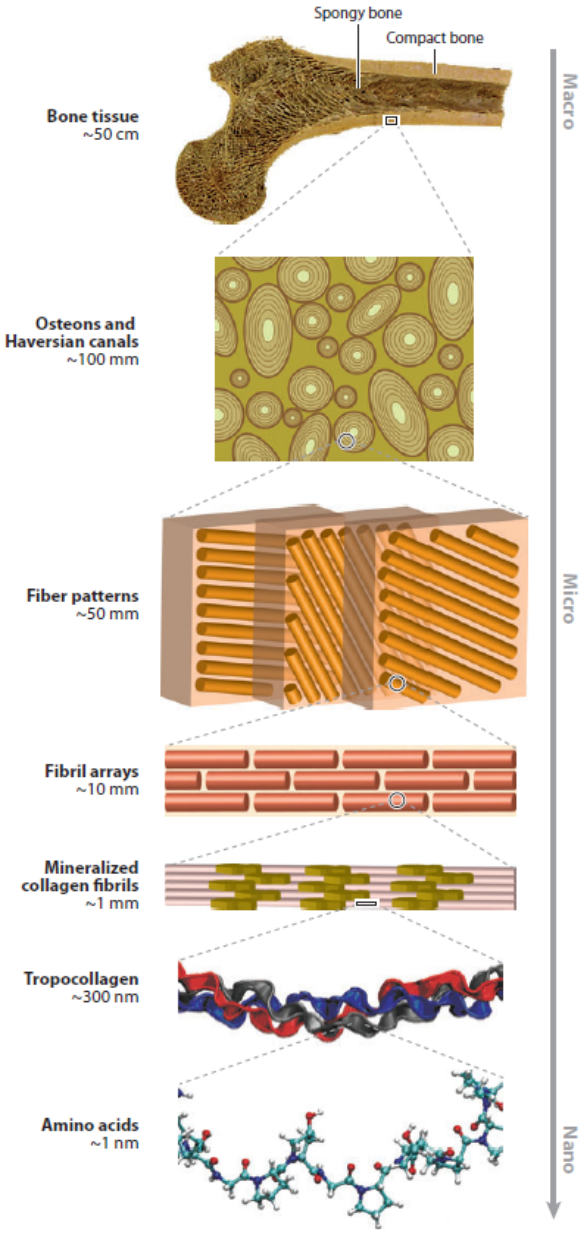

Figure 1-1: Hierarchical structure of bone. At the anatomical level, bone is composed of compact (cortical) and spongy (trabecular) bone. Cortical bone is composed of osteons and Haversian channels that line and protect blood vessels. The microscale lamellar structure in osteons arises from the layered arrangement of collagen fibers, which are composed of the smaller collagen fibrils. A staggered array of mineralized tropocollagen makes up the nanoscale arrangement of collagen fibrils [27].

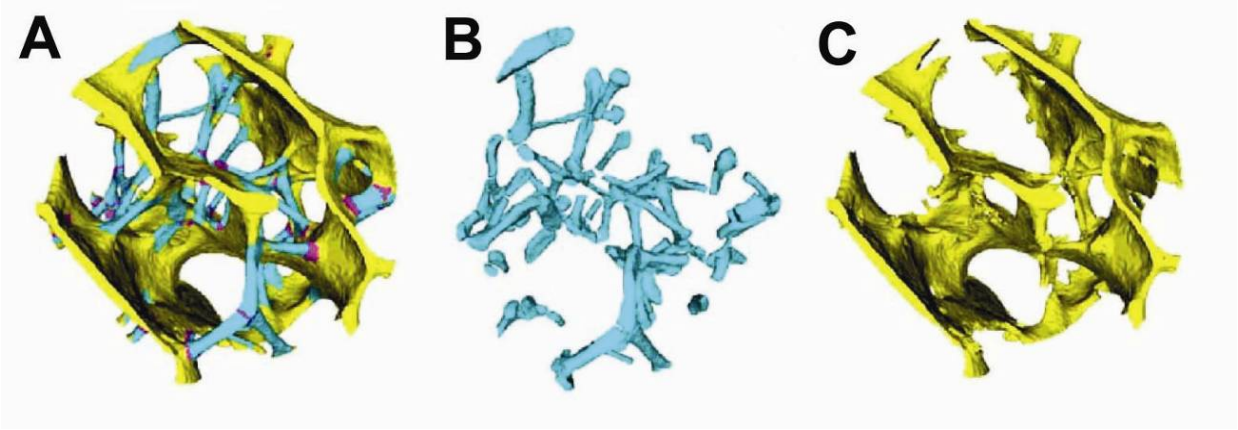

Figure 1-2: Schematic of the rod-like a plate-like composition of trabecular bone. A) Total trabecular composition of showing rod-like (cyan), plate-like (yellow) and junctions (red) components. B) After removal of all non rod-like trabecular, the rod-like trabecular with a diameter of 50 - 250 μm are clearly visible. C) After removal of all non plate-like trabecula, the interconnected network of plate-like trabecular is clearly visible [36].

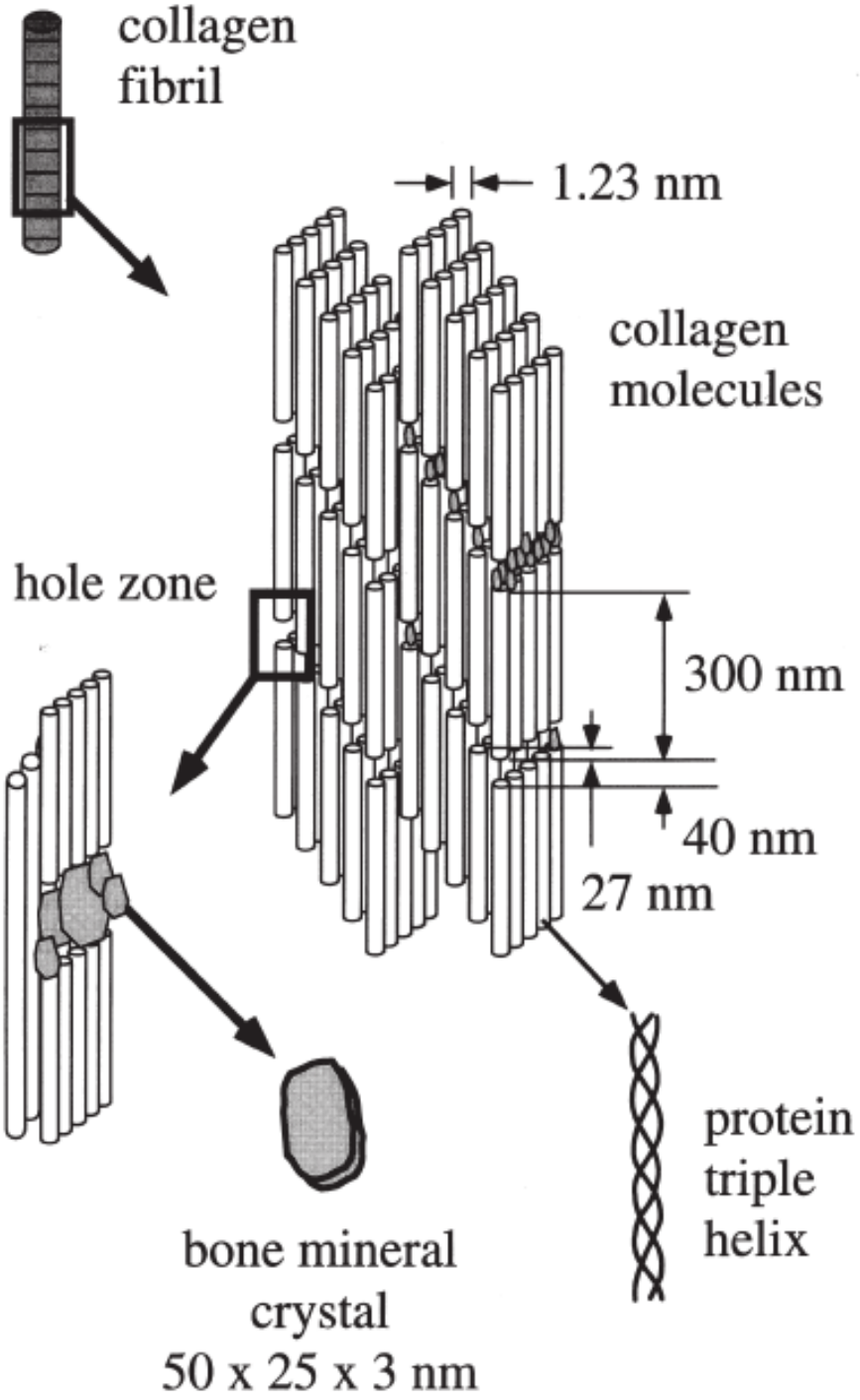

Figure 1-3: Schematic illustrating the assembly of triple helix collagen proteins into collagen fibrils and fibers. The characteristic 67 nm collagen periodicity is a result of the gap between successive collagens and a smaller overlap region [23].

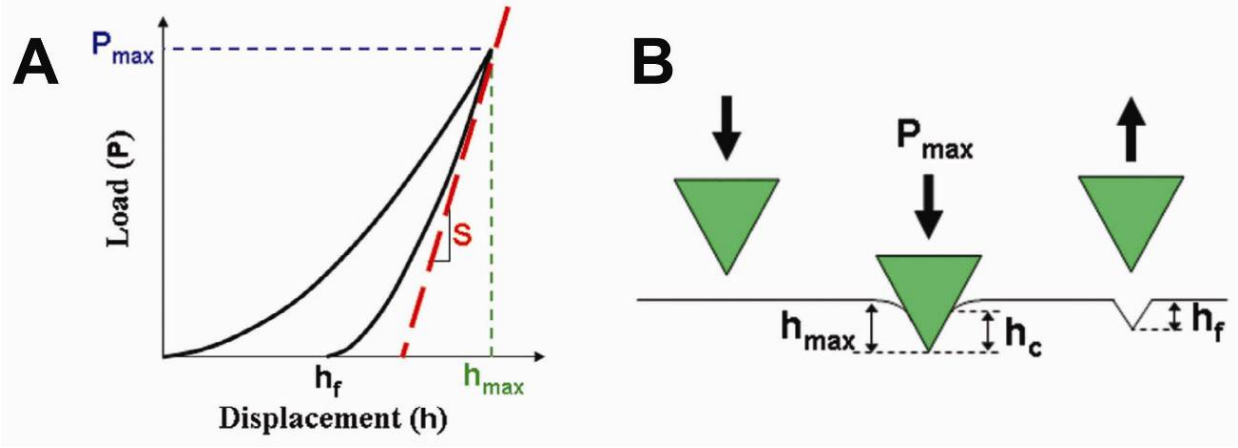

Figure 1-4: A) Load-displacement curve in a two-phase nanoindentation experiment. During the loading phase, elastic and plastic deformation occurs. The unloading phase is purely elastic and is used for analysis purposes. B) The maximum force, P_{max}, at which maximum displacement of the indenter tip occurs, h_{max}, as well as the permanent deformation, h_f, are used to compute hardness H and elastic modulus E [98].

CHAPTER 2

IMAGING THE MATERIAL PROPERTIES OF BONE SPECIMENS USING REFLECTION-BASED INFRARED MICROSPECTROSCOPY

2.1 Abstract

Fourier Transform InfraRed Microspectroscopy (FTIRM) is a widely used method for mapping the material properties of bone and other mineralized tissues, including mineralization, crystallinity, carbonate substitution, and collagen cross-linking. This technique is traditionally performed in a transmission-based geometry, which requires the preparation of plastic-embedded thin sections, limiting its functionality. Here, we theoretically and empirically demonstrate the development of reflection-based FTIRM as an alternative to the widely adopted transmission-based FTIRM, which reduces specimen preparation time and broadens the range of specimens that can be imaged. In this study, mature mouse femurs were plastic-embedded and longitudinal sections were cut at a thickness of 4 μm for transmission-based FTIRM measurements. The remaining bone blocks were polished for specular reflectance-based FTIRM measurements on regions immediately adjacent to the transmission sections. Kramers-Kronig analysis of the reflectance data yielded the dielectric response from which the absorption coefficients were directly determined. The reflectance-derived absorbance was validated empirically using the transmission spectra from the thin sections. The spectral assignments for mineralization, carbonate substitution, and collagen cross-linking were indistinguishable in transmission and reflection geometries, while the stoichiometric/non-stoichiometric apatite crystallinity parameter shifted from 1032 / 1021 cm^{-1} in transmission-based to 1035 / 1025 cm^{-1} in reflection-based data. This theoretical demonstration and empirical validation of reflection-based FTIRM eliminates

the need for thin sections of bone and more readily facilitates direct correlations with other methods such nanoindentation and quantitative backscatter electron imaging (qBSE) from the same specimen. It provides a unique framework for correlating bone's material and mechanical properties.

2.2 Introduction

The tissue material properties of bone are important contributors to bone quality and fracture risk [99-101]. In particular, mineralization, crystallinity, and collagen cross-linking may play a role in defining bone's mechanical properties. For example, positive correlations have been observed between mineralization and Young's modulus in aging mice [100], newborn rabbits [102], osteons of baboons [103, 104], the secondary mineralization of ewes [105], estrogen and bisphosphonate-treated rats [106], and vitamin D-deficient rats [101]. In humans, fracture risk has recently been associated with mineralization in cortical but not trabecular bone of the iliac crest [13], the latter of which was altered by bisphosphonate treatment [107]. While it is clear that bone's chemical, mechanical, and morphological parameters all contribute to the mechanical behavior of bone, specific relationships are often difficult to identify, in particular when the analytical methods have different constraints related to tissue preparation, and assess bone's complex material properties at different hierarchical levels and in different volumes of the tissue.

Fourier transform infrared microspectroscopy (FTIRM) and imaging (FTIRI) have become the most widely used techniques for determining the spatially-resolved chemical makeup of bone. To date, FTIRM has required thin sections of bone (typically <5 μm) in order to provide sufficient transmission of infrared (IR) light through the tissue. Specimens that are too thick will cause insufficient illumination of the detector and prevent an accurate measurement, making

quantitation impossible. Moreover, thin sections require bones to be embedded in an infiltrating plastic resin that can alter the chemical composition and cause spectral overlap with absorption features of bone [80, 108]. Spectral subtraction can be performed using a pure spectrum of the embedding material, but this can introduce error into the data since the embedding material may not be distributed homogeneously throughout the specimen. But perhaps the most important limitation of transmission-based FTIRM is the inability to perform correlative studies on the same specimen with other biomechanical and morphological methods, e.g. nanoindentation, qBSE, and 2-D surface slices from μCT reconstructions, due to the differences in specimen preparation.

In this work, we demonstrate the theoretical development and empirical validation of reflection-based FTIRM. In a reflection geometry, IR spectra are generated based on the specular reflection of IR light from a polished surface, thereby removing the requirement for thin specimens. The resultant spectra can be transformed into absorbance spectra through a Kramers-Kronig relationship. In addition to the theoretical treatment of this method, we have performed an empirical validation with transmission-based FTIRM on the corresponding thin sections of bone. With this reflection method, FTIRM can now be expanded to the analysis of thick specimens and blocks of bone, enabling direct, pixel-to-pixel correlation on the same specimen with other biomechanical and morphological imaging data.

2.3 Methods

Specimen Preparation

Three poly-methyl methacrylate (PMMA)-embedded mature mouse femurs were provided by Dr. David Burr (Indiana University School of Medicine). From each block, three longitudinal

serial sections were cut from the mediolateral plane at a thickness of 4 μm ± 0.35 μm. The second section for each femur was mounted in a slotted aluminum frame for transmission-based FTIRM. The corresponding bone blocks were first imaged unpolished with reflection-based FTIRM and then polished (Buehler, Lake Bluff, IL) with 1,200 grit carbide paper and a cloth impregnated with diamond suspensions (particle size 3, 1, 0.25, 0.05 μm) for 3 min at each step, removing a total of 54 ± 12 μm of material from the specimen surface. The polished bone blocks were then imaged. Thus, the thin section for transmission was located ~4 μm from the unpolished surface and ~60 μm from the polished surface.

FTIRM Data Collection

FTIRM data were collected using a Nicolet Continuμm IR microscope (Thermo Electron Corp) using the synchrotron infrared source at beamline U2B of the National Synchrotron Light Source at Brookhaven National Laboratory. Spectra were collected in the mid-IR region from 4000 - 650 cm^{-1} using an MCT-A* (Mercury Cadmium Telluride) detector, at a spectral resolution of 8 cm^{-1} and 128 scans/pixel. FTIRM mapping was performed with the synchrotron source, using an aperture size of 15 x 15 μm and a step size of 15 μm. The incident IR beam was measured to be 90% s-polarized onto the specimen. For each femur, a 300 μm longitudinal section of the cortical shell in the mid-diaphysis was imaged with a conventional light microscope, where matching locations were identified for both the bone blocks and the corresponding thin sections. For the thin sections, data were collected in a transmission geometry, where the background spectrum was collected through an empty specimen holder. For the bone blocks, data were collected in a specular reflection geometry from the top surface of the specimen. A polished CsI disk was used as the reflectance background to produce a detector

signal comparable to that from the specimen itself, thereby reducing susceptibility to detector non-linearity. We note that CsI has no spectral features in the spectral range of interest (4000 - 650 cm^{-1}) and that spectra can be readily corrected to a 100% reference value using its known optical properties. For each specimen, 250 - 300 spectra were collected and normalized to the synchrotron beam current.

In order to accurately employ the Kramers-Kronig transformation to the reflection-based data, a template bone IR spectrum was also collected over the far-IR to mid-IR region (4000 - 70 cm^{-1}) from a different polished mouse bone block. The 4000 - 650 cm^{-1} spectral range was collected with the Nicolet Continuμm IR microscope as described above. A Spectra Tech IRμs microscope was used at beamline U12IR at the National Synchrotron Light Source. Both bolometric and photoconductive Ge:Cu detectors were used to obtain data over the 400 - 70 cm^{-1} and 1000 - 200 cm^{-1} spectral ranges, respectively. Reflection-based data were collected from the top surface of the bone block with the synchrotron source and an aperture size of 120 x 120 μm (8 cm^{-1} resolution, 1024 scans/pixel). Overlapping spectral regions were observed to be identical and were manually removed. The three spectra were then appended to produce a continuous template bone IR spectrum from 4000 - 70 cm^{-1}. See Supporting Information for a more detailed explanation of the MATLAB implementation.

Chemical Parameters

Bone chemical composition parameters were determined from the transmission and reflection derived absorbance spectra using Bruker OPUS 6.5 software. Specifically, we determined the degree of mineralization (phosphate / protein ratio) [81], carbonate substitution into the mineral

lattice (carbonate / phosphate ratio) [109], crystallinity (ratio of stoichiometric / non-stoichiometric phosphate) [110], and collagen cross-linking [79] as outlined in Table 2-1.

Statistical Analyses

Means, standard deviations, and the ratio of the standard deviation to the mean (i.e. coefficients of variation) for each integration map were calculated. Edge pixels were identified by overlaying the IR map with the visible light micrograph and were discarded from the data set. Values for percent difference between the thin sections and polished blocks were calculated by dividing the difference between the means by the average of the means.

2.4 Results

Transmission-based FTIRM

IR absorbance spectra of bone were collected in a transmission geometry through 4 μm bone thin sections (Figure 2-1). In most regions, the specimens were cut sufficiently thin to permit at least 10% transmission of the IR light as to ensure a sufficient signal response from the detector. The resultant spectra from these regions showed well-defined absorption peaks. Local regions where the sections were too thick (typically >5 μm) had zero or near-zero transmission, resulting in spectra with truncated or ill-defined absorbance values in spectral regions with high absorbance, most notably the v_1,v_3 PO_4^{3-} region from 1200 - 900 cm^{-1}. Furthermore, several spectra appeared to contain absorption peaks unique to the PMMA embedding material. PMMA has major absorption features that overlap with the protein, carbonate, and mineral phosphate peaks found in bone, and is most easily recognized by a sharp and intense carbonyl ester absorption peak centered at 1745 cm^{-1} (Figure 2-1).

Reflection-based FTIRM

As an alternative to transmission-based FTIRM, the chemical composition of bone was assessed using a specular reflection geometry, where reflected IR light is collected from the bone surface at a near-normal angle. In a specular reflectance spectrum, absorption features have a derivative-like appearance due to a combination of the specimen's dispersive refractive index and extinction coefficient [111] (Figure 2-2A). Although all of the absorption features exist in this spectrum, the conventional analysis method for transmission spectral data is not appropriate. To analyze the reflectance spectral data, we used a standard method based on a Kramers-Kronig relationship to directly extract the specimen's complex refractive index. Other quantities, such as the absorbance, were then calculated and used in the same manner as spectral data from the transmission geometry.

The Kramers-Kronig relationships connect the real and imaginary parts of any physical response function by an integral transform. When a light wave is incident on a surface, a portion is reflected and also shifted in phase. A basic measurement of the reflectance senses the reflected wave amplitude, but not the phase shift. Applying the Kramers-Kronig transformation to the measured reflected wave amplitude yields the phase shift. Knowing both the reflected wave amplitude and phase shift is sufficient to uniquely determine the material's refractive index, from which other quantities, such as the absorption coefficient, can be directly derived. The resulting frequency-dependent absorption coefficient can then be analyzed using methods analogous to those from standard transmission spectroscopy (see Supporting Information).

One challenge of the Kramers-Kronig transform is that it involves integrations over all spectral frequencies from zero to infinity. Fortunately, the contributions from more distant

spectral regions are less significant and simple extrapolations for the reflectance throughout these regions can be used to good accuracy. However, it is important to capture any nearby spectral features; therefore, measurements must cover a sufficiently broad spectral range to ensure this is achieved. For bone, most of the dominant spectral features exist between 2000 and 500 cm^{-1}. In order for the Kramers-Kronig transformation to be applied accurately, each bone spectrum must be extended beyond this spectral range.

Conventional FTIR microscopes use MCT detectors having a good spectral response from approximately 4000 to 650 cm^{-1}. When the Kramers-Kronig transformation was applied to a bone spectrum having a low-frequency cutoff of 650 cm^{-1}, the resulting ν_1,ν_3 PO_4^{3-} absorption peak from 1200 - 900 cm^{-1} had an incorrect (i.e. skewed) baseline (Figure 2-2B). Though the intensity and frequency of the ν_1,ν_3 PO_4^{3-} peak are correct, the skewed baseline can cause significant error during peak integration. Extending the measured spectral range down to 450 cm^{-1} improved the baseline. However, due to the ν_4 PO_4^{3-} peak from 650 - 500 cm^{-1}, the bone spectrum should be extended even further in order to completely account for these absorbance features prior to applying the Kramers-Kronig transformation. Figure 2-2B also shows a bone spectrum that was collected to 70 cm^{-1}. This spectrum clearly shows that the baselines for both the ν_1,ν_3 and the ν_4 PO_4^{3-} peaks are no longer skewed. Thus, in order to generate accurate reflection FTIRM data, the bone spectral range should be at least 4000 - 70 cm^{-1}.

In practice, conventional FTIR microscopes are not equipped with the appropriate detectors for collecting this wide spectral range. However, an a priori knowledge of the absorption features of bone permits an acceptable spectral extrapolation without the need to collect data to 70 cm^{-1} for each and every spectrum. Thus, we collected a reflection spectrum across the mid- and far-IR spectral range (4000 - 70 cm^{-1}) from a different polished bone specimen. This template spectrum

was used to extend the spectral range of spectra collected with the conventional MCT detector from 850 to 70 cm^{-1}. Specifically, a Matlab routine was developed to scale the 4000 - 2500 cm^{-1} baseline region of the template spectrum to match that of the specimen spectra and the ν_1,ν_3 PO_4^{3-} peak intensity at 1035 cm^{-1} of the template was scaled to match that of the specimen spectra. Then, the 850 - 70 cm^{-1} portion of the template spectrum was appended to the specimen spectra, and the 900 - 850 cm^{-1} region of the specimen spectra were replaced with an averaged 900 - 850 cm^{-1} region from the template spectrum and the specimen spectra. The OPUS 6.5 (Bruker Optics, Billerica, MA) Kramers-Kronig transform algorithm was used to calculate the extinction coefficient of extended specimen spectra spanning 4000 - 70 cm^{-1}. From there we determined frequency-dependent absorption coefficient spectra assuming a 4 μm thick specimen (see Supporting Information).

Surface polishing to maximize specular reflectance

Polishing of the specimen surface with a particle grit size of 50 nm yielded an increase in bone reflectance of up to 10% (Figure 2-3A). Most notably, the ν_1,ν_3 PO_4^{3-} region saw an increase in reflection from 5% to 15% after polishing. This gain in reflectance translated into a higher amplitude absorption coefficient spectrum and improved signal-to-noise of the spectral absorption peaks (Figure 2-3B). It is important to note that a poorly polished surface may lead to a mainly diffuse reflecting surface and an overall reduction in the reflected signal, resulting in poor signal-to-noise. However, the relative absorption strengths for the various spectral features were not observably affected, such that accurate relative chemical information could still be obtained. Although polishing has the potential to alter the chemical composition of the bone surface, these changes are likely small and limited to an undetectable fraction of the sampled depth by reflection-based FTIRM.

The effect of angle of incidence & light polarization

The intensity of light reflected back from the bone surface is referred to as the reflection coefficient, which is a function of the refractive index of bone, the angle of incidence, and the polarization of the light. Normal incidence is assumed for the conventional Kramers-Kronig transform algorithm, which is a potential issue for reflectance measurements using a high numerical aperture optic where angles of incidence can approach 40°. To test this issue, the reflection coefficient of fully mineralized bone was estimated as a function of incident angle and polarization using the average refractive index of hydroxyapatite (n = 1.530). For Schwarzschild objectives typically used in IR microscopes (numerical aperture: ~0.6), the incidence half angle range was determined to be 15 - 40° with a median of 37° (Figure 2-4A). Using the Fresnel equations for both s- and p-polarized light, it was determined that the reflection coefficient for hydroxyapatite was sufficiently constant out to 40° that it did not measurably affect the analysis. The other specimen constituents had a smaller refractive index for which the angle dependence was even weaker (Figure 2-4B). Thus, for the standard FTIRM configuration, the angle of incidence was close enough to the normal such that the reflection coefficient remained approximately constant for all types of polarization.

Validation of reflection-based FTIRM with transmission-based FTIRM

Theoretically we demonstrated that reflection-based FTIR microspectroscopic data can be transformed into absorbance-like spectra through spectral extrapolation and a Kramers-Kronig transformation, where factors such as surface polishing, angle of incidence, and IR polarization should be considered. In addition, we validated reflection-based FTIRM empirically by

comparing transmission-based FTIRM results from 4 μm thick bone sections with reflection-based FTIRM data from the matching polished bone blocks (Figure 2-5).

The light micrograph of an imaged area is shown in Figure 2-5B. The mineralization, collagen cross-linking, carbonate substitution and crystallinity profiles of a thin section and matching bone block are shown in Figures 2-5C-F. The peak frequencies and spectral integration parameters (Table 2-1) for the transmission and reflection data were compared using second derivative spectra. Absorption peak frequencies in the 1800 – 1300 cm^{-1} region were shifted by < 2 cm^{-1} between transmission- and reflection-based analyses so the integration ranges for these parameters were not adjusted (Figure 2-6A). However, due to a smaller amount of line broadening of the ν_3 PO_4^{3-} in the reflection spectra, the non-stoichiometric apatite peak at 1021 cm^{-1} and the stoichiometric apatite peak at 1032 cm^{-1} in the transmission spectra were shifted to 1025 and 1035 cm^{-1} in the reflection spectra, respectively (Figures 2-6B and 2-6C).

When comparing the percent difference between transmission and reflection FTIRM (Table 2-2), the mineralization, carbonate incorporation, and collagen cross-linking varied by 7 - 9%, while the difference in crystallinity was higher at 16%. Table 2-2 shows the coefficients of variation (CV) for each parameter, which represent a measure of specimen-to-specimen variation. For both transmission and reflection FTIRM, the collagen cross-linking, mineralization, and carbonate incorporation showed a 7 - 10% variation between different bone specimens. The crystallinity was much more consistent between specimens, with a CV value of only 2 - 3%.

2.5 Discussion

Fractures of the skeleton are directly related to a deterioration of bone strength. However, it has become clear that fractures cannot be explained as a simple decrease in bone quantity (i.e. bone mineral density), but are also significantly dependent upon bone quality. While a formal definition of bone quality is somewhat elusive, mechanical tissue properties are a critical factor. As these mechanical properties will be greatly influenced by the chemical composition and ultrastructure of the tissue, methods that can readily correlate individual chemical, mechanical, and structural properties are necessary. To date, correlative studies such as these are typically performed across different specimens without performing the correlations on the same volume of tissue. While useful, this approach is limited by inter- and intra-specimen heterogeneity. In this study, we developed and demonstrated reflection-based FTIRM as an alternative approach to transmission-based FTIRM, enabling direct pixel-to-pixel correlations with other high resolution imaging modalities such as nanoindentation and qBSE on a single specimen, thereby providing accurate spatial associations between outcome measures.

We have shown theoretically that spectra produced by reflection-based FTIRM can be transformed into absorbance-like spectra using a Kramers-Kronig transform. These absorbance-like spectra can be analyzed with standard methods used for transmission-based FTIRM. Furthermore, no additional hardware is required for reflection FTIRM beyond what is already available for transmission FTIRM. The Kramers-Kronig transformation relies upon the measurement of the specular (non-diffuse) reflectance from the specimen surface. Specimen preparation consists of polishing the specimen and orienting its surface perpendicular to the normal of the incident IR beam to ensure that spectral data are collected with high signal-to-

noise. In order to ease handling and orient the bone properly for polishing, the specimen may be mounted and/or embedded.

We have shown empirically that reflection-based FTIRM can be used to determine the mineralization, crystallinity, carbonate substitution, and collagen cross-linking parameters that are equivalent to the transmission-based approach. Absorption peaks were shifted by <2 cm^{-1} between the reflection and transmission datasets in the 1800 - 1300 cm^{-1} region. We observed 3 - 4 cm^{-1} shifts in absorbance maxima and a narrowing of the bandwidths for the non-stoichiometric and stoichiometric apatite peaks, suggesting that conventional Gaussian/Lorentzian fits, which are presumed to be the best-fit distribution for standard transmission FTIRM, may not best describe spectral peaks obtained via reflection-based FTIRM. Rather, a more Gaussian-like band shape better describes the reflection data and may be attributed to a reduced natural and/or collision broadening in reflection-based FTIRM [112].

One benefit of reflection-based FTIRM is that the technique does not require thin bone specimens, and thus sample embedding is not strictly required, although it may facilitate the handling of thick bone specimens and small bone blocks. While most human tissue specimens are already embedded for histology or histomorphometry, many specimens from pre-clinical studies are readily available and typically not embedded. For these specimens, a non-infiltrating embedding resin such as epoxy can be used to help orient and polish the sample. This process can be done overnight compared to several weeks for embedding in an infiltrating resin such as PMMA. The use of a non-infiltrating resin also avoids potential spectral overlap between the resin and bone and therefore removes the need for subtracting the resin spectrum at each pixel.

The use of thick bone specimens or small bone blocks also enables true pixel-to-pixel correlations with other imaging modalities such as nanoindentation, qBSE and/or a 2D surface slice from a μCT reconstruction. It can also be correlated with Raman microscopy, which has been successfully used to obtain chemical information on thick bone specimens and small bone blocks, but also on bulk bone and fresh, hydrated specimens. Raman microscopy can provide sub-micron spatial resolution, but data acquisition times are typically longer [113].

Reflection-based FTIRM removes several possible sources of variability that can occur in transmission-based FTIRM, such as those introduced by specimen preparation and the cutting of thin sections. While reflection-based FTIRM provides an attractive alternative to the transmission-based approach, potential sources of error and factors that reduce signal-to-noise must be taken into careful consideration. First, in order to achieve the best signal-to-noise, the angle of incidence provided by the IR optics should be <40°. If this angle is exceeded, or if the median angle approaches this value, the IR polarization should be predominantly s-polarized. Second, the specimen should be polished to a flat and specular reflecting surface. Third, spectral processing of reflection spectra into their equivalent absorption spectra is performed using algorithms in commercially available software, and requires that spectra be extended beyond the peaks of interest. In the case of bone, the ν_1,ν_3 PO_4^{3-} peak will not be properly resolved if this condition is not met.

One limitation of the empirical validation of this study arises from the fact that the regions probed for the transmission and reflection measurements were not identical. Since it was necessary to polish the bone block after cutting the thin sections, the sampled regions were offset by 54 ± 12 μm in the mediolateral plane, a length scale at which chemical variations can exist. Small differences in the homogeneity of biochemical components will lead to small differences

in the spectroscopic data [113]. However, the bones analyzed were from the cortical shell of the mid-diaphysis of mature mouse femurs, which are not undergoing significant bone metabolism, limiting the spatial heterogeneity. Nonetheless, the magnitude of the variations between the sampled regions of the polished bone block and the thin sections was well within the range of inherent bone specimen heterogeneity, both spatially within one specimen and between specimens. Thus, the observed chemical differences between the transmission and reflection measurements were possibly due to the ~54 μm displacement between the sampled regions.

2.6 Conclusion

In summary, we anticipate that reflection-based FTIRM will more readily allow the pixel-to-pixel correlations within a single specimen between bone's material, mechanical, and morphological properties on the micron (and perhaps nano) scale by combining FTIRM with techniques such as nanoindentation, Raman microscopy, qBSE, and 2D surface slices from μCT reconstructions. These investigations may elucidate how region-specific differences in bone chemistry – caused by metabolic, genetic, environmental, or structural influences – affect the microscopic material properties of bone tissue and alter the local mechanical behavior. As such, this spatially-resolved, correlative approach will significantly contribute to a better understanding of the contributors to bone quality and fracture risk.

2.7 Supporting Information

Fourier Transform InfraRed Microspectroscopy (FTIRM) is a spectroscopy technique most frequently used to measure the transmittance through a material. When the measured quantity is

expressed as a transmittance spectrum $T(\omega)$, the ratio of $I(\omega)_{\text{sample}}$ to $I(\omega)_{\text{reference}}$, then the sample's absorbance spectrum $A(\omega)$ can be calculated by:

$$A(\omega) = -\log_{10} T(\omega). \tag{1}$$

For optically thin samples, the absorbance spectrum can be further related to the molar absorptivity $\varepsilon(\omega)$, the thickness of the sample b, and the concentration c by using the Beer-Lambert law:

$$A(\omega) = \varepsilon(\omega) \cdot b \cdot c. \tag{2}$$

Retrieval of Reflected Phase by Kramers-Kronig Analysis

The measured specular reflectance $R(\omega)$ from the front plane of a single interface is related to the modulus of the complex reflectivity squared $r(\omega)^2$, which can also be expressed as the product of the complex reflectivity $r(\omega)$ and its complex conjugate $\overline{r(\omega)}$:

$$R(\omega) = \left|r(\omega)\right|^2 = r(\omega)\left[\overline{r(\omega)}\right]. \tag{3}$$

At normal incidence, Fresnel's equations relate the complex reflectivity $r(\omega)$ and the complex refractive index $N(\omega) = \eta(\omega) + \mathrm{i}\kappa(\omega)$, where $\eta(\omega)$ is the refractive index and $\kappa(\omega)$ is the extinction coefficient, as:

$$r(\omega) = \frac{N(\omega) - 1}{N(\omega) + 1} = \frac{\eta(\omega) - 1 + \mathrm{i}\kappa(\omega)}{\eta(\omega) + 1 + \mathrm{i}\kappa(\omega)}. \tag{4}$$

Further, the reflective amplitude $r(\omega)$ can be written as the complex function:

$$r(\omega) = \sqrt{R(\omega)} \cdot e^{i\theta(\omega)}, \tag{5}$$

where the first term is the amplitude and the second term contains the phase change of the reflected light. Taking the logarithm of Eq.5 one obtains:

$$\ln r(\omega) = \tfrac{1}{2} \ln R(\omega) + \mathrm{i}\theta(\omega) . \tag{6}$$

Further, we may use the principle of relativistic causality and employ the Kramers-Kronig relationship to solve for the imaginary part ln $r(\omega)$ using it's real part:

$$\theta(\omega) - 1 = \frac{2}{\pi} P \int_0^\infty \frac{\ln|r(\omega)|}{\omega^2 - \omega'^2} dw , \tag{7}$$

where P denotes the Cauchy principal value for the singularity of $\omega = \omega'$. Thus, a complete measurement of the reflectance over all ω from a surface provides $|r(\omega)|$ from which the phase shift $\theta(\omega)$ can be determined. The complex refractive index can then be calculated using Eq.4. This is a well-established method for determining the optical response functions of bulk materials [111].

Calculation of Absorption Coefficient Spectrum

With the reflectance measured experimentally and the phase determined using a Kramers-Kronig relationship, we rewrite Eq.5 using Euler's formula, $e^{-\theta} = \cos(\theta) + i \sin(\theta)$, and equate this to Eq.4 to give:

$$\sqrt{\mathrm{R}(\omega)} \cdot (\cos\theta + \mathrm{i}\sin\theta) = \frac{\eta(\omega) - 1 + \mathrm{i}\kappa(\omega)}{\eta(\omega) + 1 + \mathrm{i}\kappa(\omega)} . \tag{8}$$

Solving for $\eta(\omega)$ and $\kappa(\omega)$:

$$\eta(\omega) = \frac{1 - R(\omega)}{1 + R(\omega) - 2\sqrt{R(\omega)} \cdot \cos\theta(\omega)} , \text{ and} \tag{9}$$

(10)

$$\kappa(\omega) = \frac{-2\sqrt{R(\omega)} \cdot \sin\theta(\omega)}{1 + R(\omega) - 2\sqrt{R(\omega)} \cdot \cos\theta(\omega)}.$$

Although the refractive index $\eta(\omega)$ and the extinction coefficient $\kappa(\omega)$ can thus be derived from the measured $R(\omega)$ using a Kramers-Kronig relationship, we can further use $\kappa(\omega)$ to calculate the absorption coefficient spectrum α for a thickness d by considering Eq.2 and that $\kappa(\omega) = \alpha / \bar{\nu} 4\pi$.

$$(\varepsilon\kappa) = \alpha = 4\pi\bar{\nu}d\kappa. \quad (11)$$

Although direct comparisons between reflection-derived absorption coefficient spectra and traditional transmission-derived absorption spectra can be made, more accurate comparisons should take into consideration the reflection losses from the surface of the thin sections in the transmission geometry by:

$$T(\omega) = \frac{(1 - R(\omega))^2 e^{-\alpha(\omega)t}}{1 - R(\omega)^2 e^{-2\alpha(\omega)t}}, \quad (12)$$

where t is the sample thickness. In this equation, the numerator describes the transmission after accounting for the first reflective bounce, and the denominator is the sum of additional reflective bounces. We investigated the difference between reflection-derived absorbance coefficient spectra with and without accounting for reflection losses. We investigated the possibility that the line widths in transmission based absorbance spectra are slightly skewed since reflection losses from a thin section are not considered in standard equations for absorbance. When we calculate an absorbance spectrum that does account for reflection losses, peak maxima do not shift noticeably, so not accounting for reflection losses is not a significant source of error for this class of low n materials (Figure 2-7).

Spectral Extrapolation

The Kramers-Kronig relationship for the phase (Eq.7) contains a semi-infinite integral over ω and thus requires knowledge of the entire bone reflectance spectrum at all ω. Given that spectrometers have a limited detection range, the true Kramers-Kronig integration cannot be achieved. Several alternatives to the original Kramers-Kronig relationships have been suggested, such as singly subtractive [114] and multiply subtractive [115] relationships, both of which rely on anchor points that can be used to control the extrapolation of data beyond the finite data set. Yet another alternative is the more general iterative maximum entropy model that does not rely on near-normal incidence light [116]. Rather than extrapolating, the proposed solution in this work relies on *a priori* knowledge of the absorption features of the sample at an energy range beyond spectral features of interest.

Implementation in MATLAB

A custom written MATLAB program provided data processing capabilities for reflection-based FTIRM data (Overview shown in Figure 2-8). The operator of the software provides the specimen and reference single beam spectra through the MATLAB command line interface. Optionally, the date and time of the measurement can be provided if beam current normalization of the spectrum is desired. The MATLAB program validates the user input and proceeds to current normalization if this is requested. In this step, a beam current history log is accessed and the date and time of the measurement are used to read out the beam current for that measurement. The spectrum is then normalized to 1000 mA. Afterwards, the normalized spectrum is extended into the farIR region using a farIR reference spectrum of bone, which was determined *a-priori* (See Appendix B for actual the MATLAB implementation). The extended

spectrum is then used to calculate an equivalent absorbance spectrum using an external Kramers-Kronig routine, such as provided by Bruker OPUS 6.5 or Thermo Nicolet's Omnic data processing software. The absorbance spectrum is then written to file and is ready for further processing by the user. This MATLAB program can also be used to process entire IR maps, in which case the user inputs the IR map file containing several spectra.

Bone Block Sample Holder for IR Imaging

Confocal microscopes focus light into a focal point, the depth and width of which are defined by the size of the aperture and geometry of the objective. The focal point lies on a plane perpendicular to the incident light, called the focal plane. Raster scanning the focal point across a large portion of a specimen is a common way to perform spatially resolved imaged. In the case of a microscope equipped with a focal plane array, the sample is placed in a out of focus plane, thus creating an unfocused, but larger illuminated spot on the specimen. In either case, the surface of the specimen should be flat and parallel to the focal plane. This is especially important when using high power objectives or objectives with a small aperture as the depth of focus will be smaller, but also when imaging large areas of a specimen. The external geometry of the embedding material around bone blocks can be cut to create a flat bottom, parallel to the front surface. In a reflection mode geometry, where reflected rays enter back into the objective, it is critically important that the focal plane and the reflecting surface of the specimen are aligned. A slight skew between the two surfaces will cause rays to reflect back at the objective at an off-center angle, causing data to appear distorted.

The design of a bone block sample holder for IR microscopy is based on a previous design for a leveling device used for polished microsections [117]. The design should align the

reflecting surface of the specimen parallel to the focal plane to ensure proper reflection of reflected rays back into the objective. To achieve this, a holder with 3 or 4 set screws holds the specimen in place (Figure 2-9). The holder is first placed upside down and around the specimen, which is also upside down, on a flat surface. The screws are then carefully fastened, ensuring that the reflecting surface of the specimen is parallel with the top and bottom surfaces of the sample holder. The holder is then placed right side up on the stage plate, at which point the focal plane and the reflecting surface of the specimen are parallel.

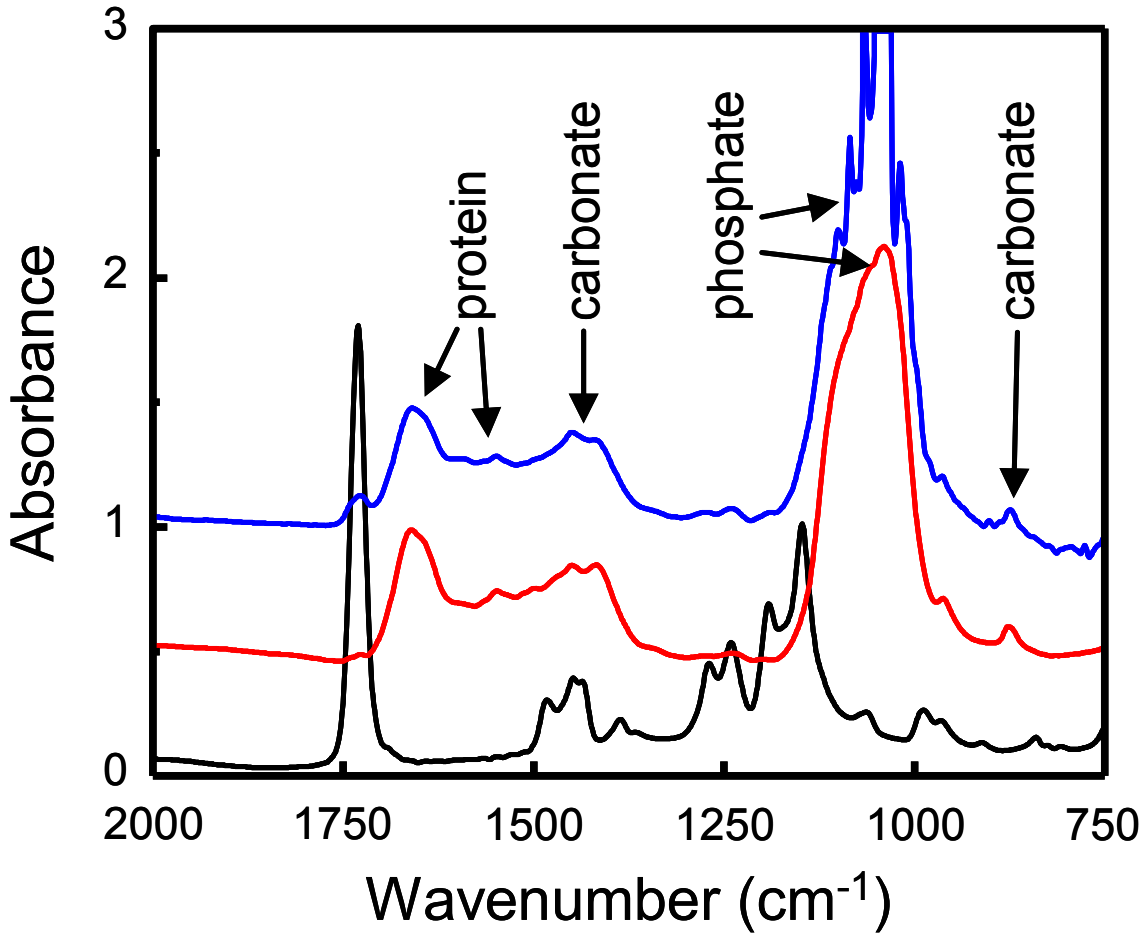

Figure 2-1: (Red) A typical IR spectrum of bone showing the characteristic protein and mineral components. (Blue) A IR spectrum taken from a bone section that is too thick, illustrating detector saturation at the v_1v_3 phosphate peak. (Black) The IR spectrum of the embedding medium PMMA, showing peaks that overlap with the bone spectrum. Spectra were offset by 0.5 absorbance units for clarity.

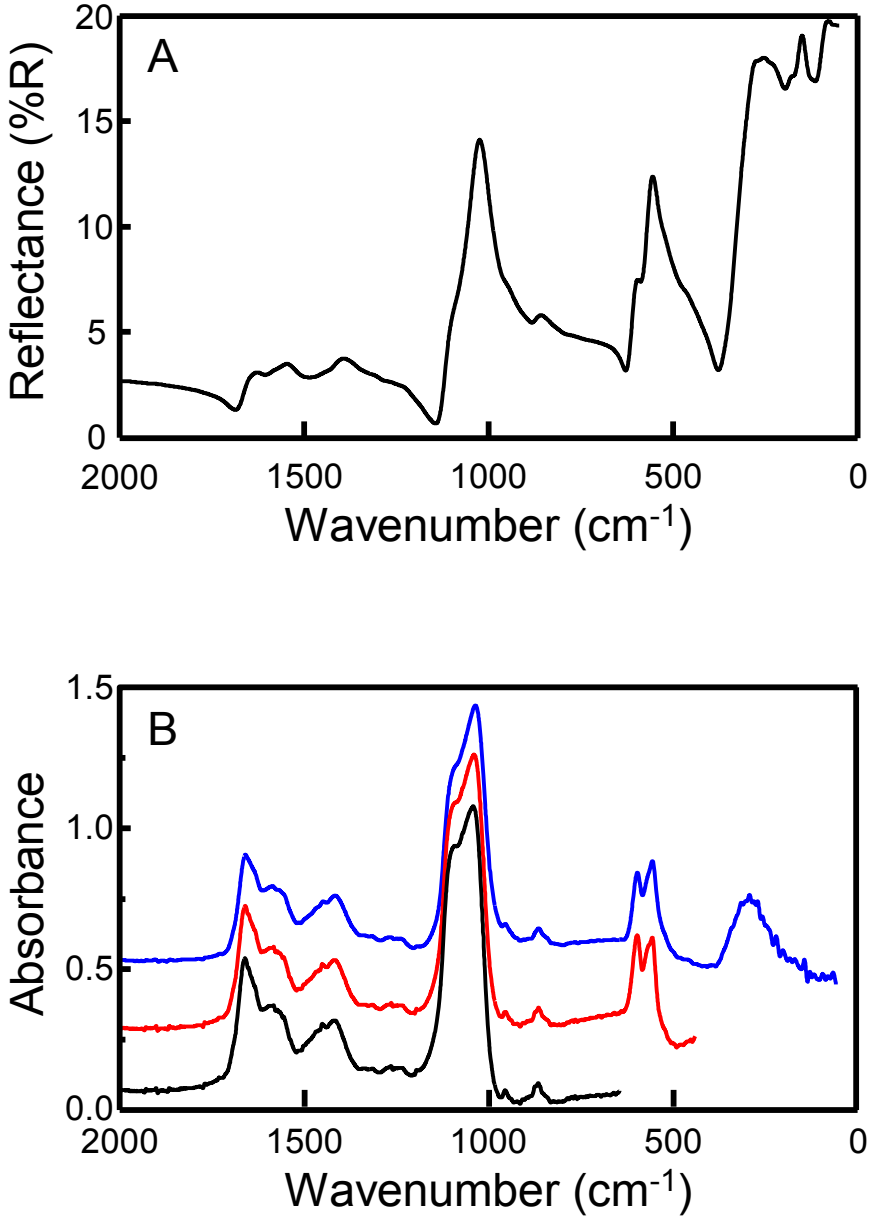

Figure 2-2: (A) An IR spectrum of a mineralized bone block collected in a reflection geometry. (B) IR absorbance spectra calculated from the reflectance data in (A) with a low-frequency cutoff at 650 (black), 400 (red) and 70 cm^{-1} (blue). Spectra were offset by 0.25 absorbance units for clarity.

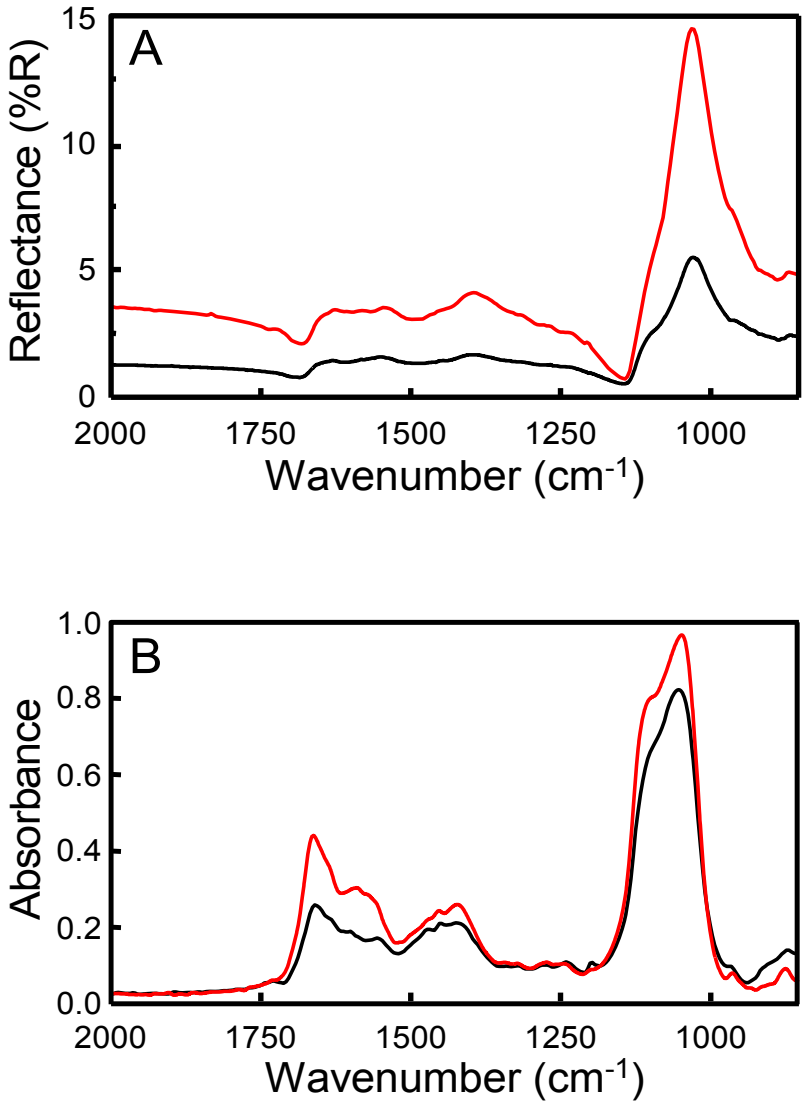

Figure 2-3: (A) IR reflectance spectra of a polished (red) and unpolished (black) bone block. The polished bone block has a net reflectance nearly double that of the unpolished block over the entire range of the spectrum. (B) IR absorbance spectra calculated from the reflectance data in (A). The polished bone block (red) has an overall higher absorbance than the unpolished block (black), consistent with the increased reflectance as seen in (A). However, the relative peak intensities for the spectral integrations relevant to bone are not affected by the quality of polishing.

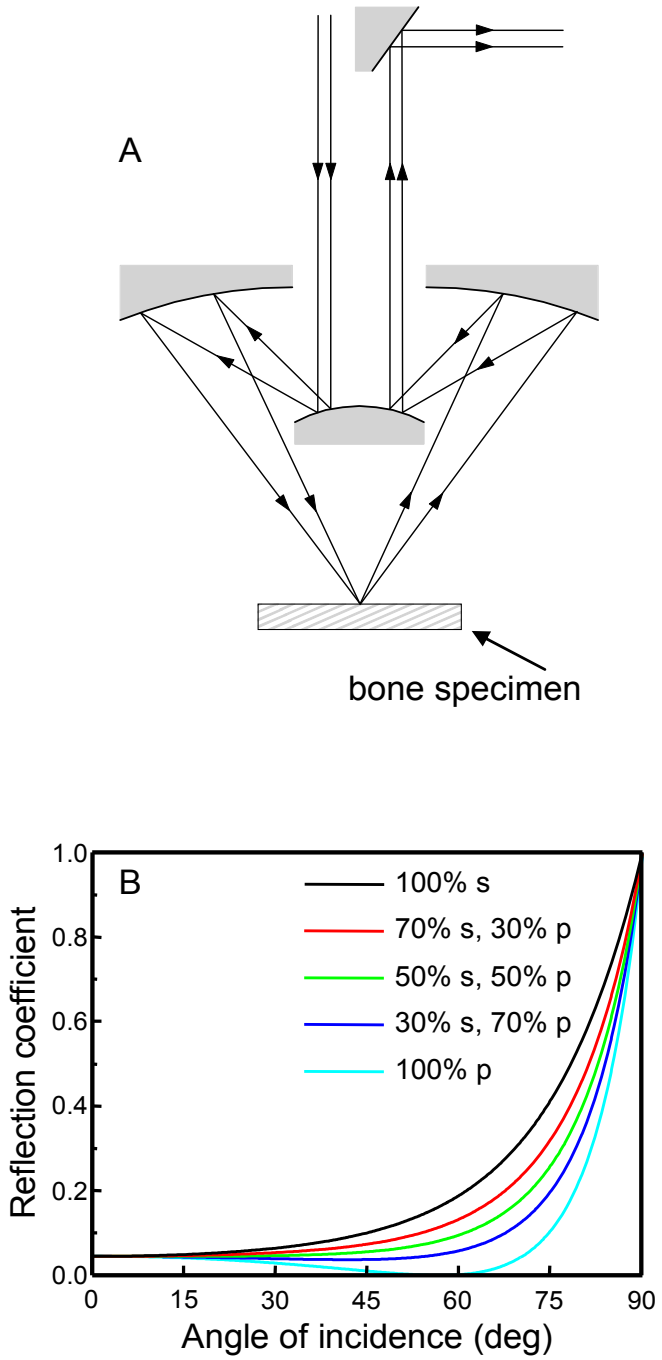

Figure 2-4: (A) Schematic overview of the reflection geometry configuration using a Schwarzschild objective typically employed in IR microscopes. The central obscuration limits the half angle to a range between 15 - 40°. (B) Plot of the reflection coefficient versus angle of incidence as a function of polarization for hydroxyapatite (n = 1.530). The reflection coefficient changes as a function of angle of incidence, but remains sufficiently constant out to 40° such that is does not measurably affect analysis.

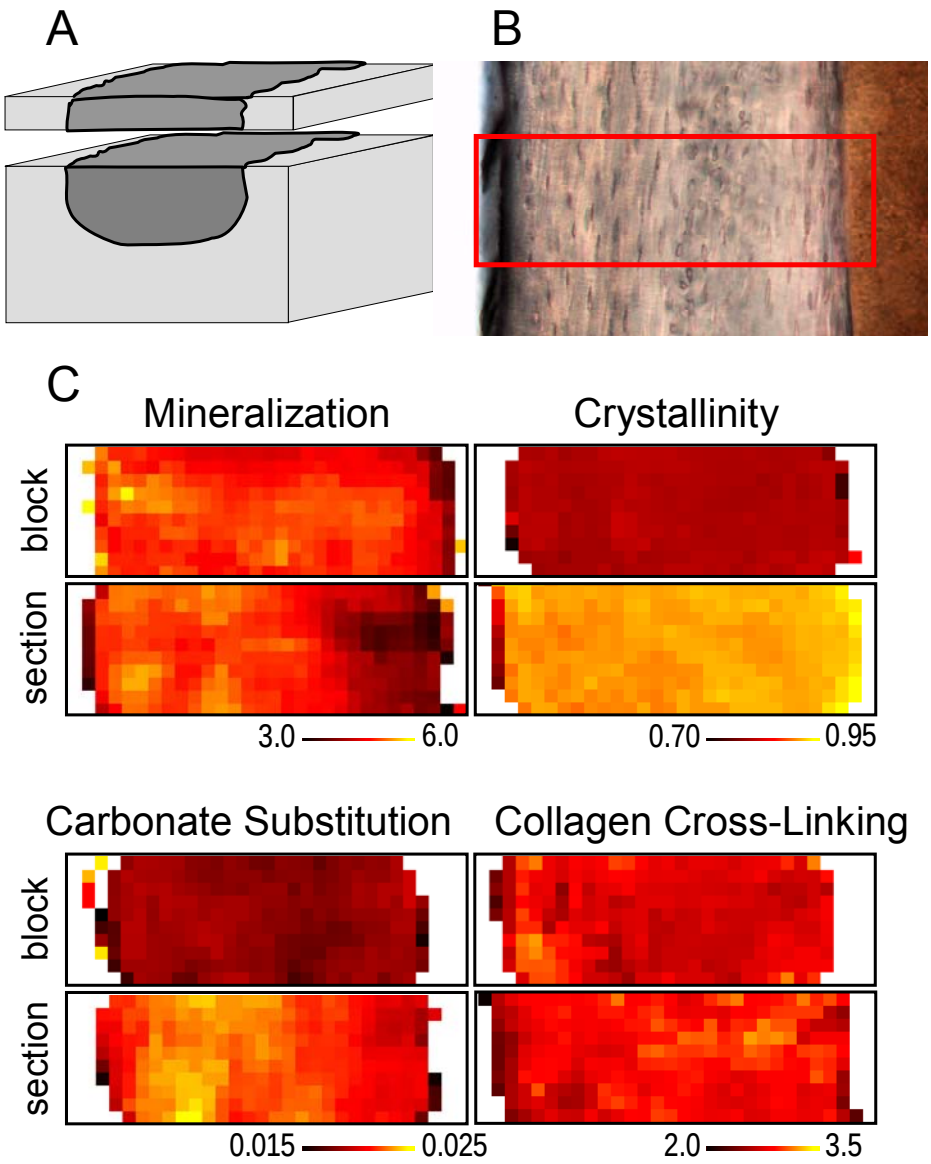

Figure 2-5: (A) Schematic of specimen preparation. Thin sections were cut from the top surface of the bone block and imaged in a transmission geometry. The bone block was then imaged before and after polishing. (B) Light micrograph of an embedded and polished bone specimen with the highlighted area showing the region that was scanned using reflection FTIRM. (C) Integration maps showing the distribution of mineralization, crystallinity, carbonate substitution and collagen cross-linking for matching bone blocks and thin sections.

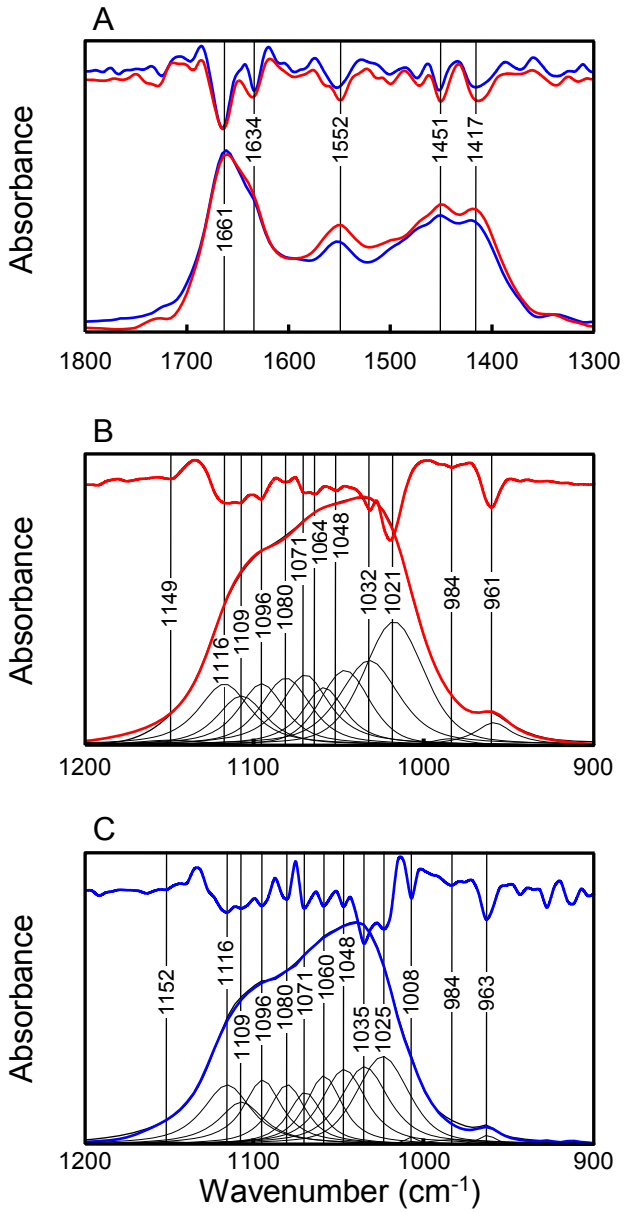

Figure 2-6: (A) Transmission (red) and reflection (blue) IR spectra and second-derivative spectra showing identical peak positions of the amide I, amide II, and CO_3^{2-} bands. (B and C) Curve-fitting of the ν_1,ν_3 PO_4^{3-} domain from (B) transmission and (C) reflection spectra based on peak positions from second-derivative spectra. Individual Gaussian/Lorentzian distributions and the resultant spectrum are also shown (black). The stoichiometric and non-stoichiometric apatite peaks are shifted from 1032 and 1021 cm^{-1} in transmission derived to 1035 and 1025 cm^{-1} in reflection derived absorbance spectra.

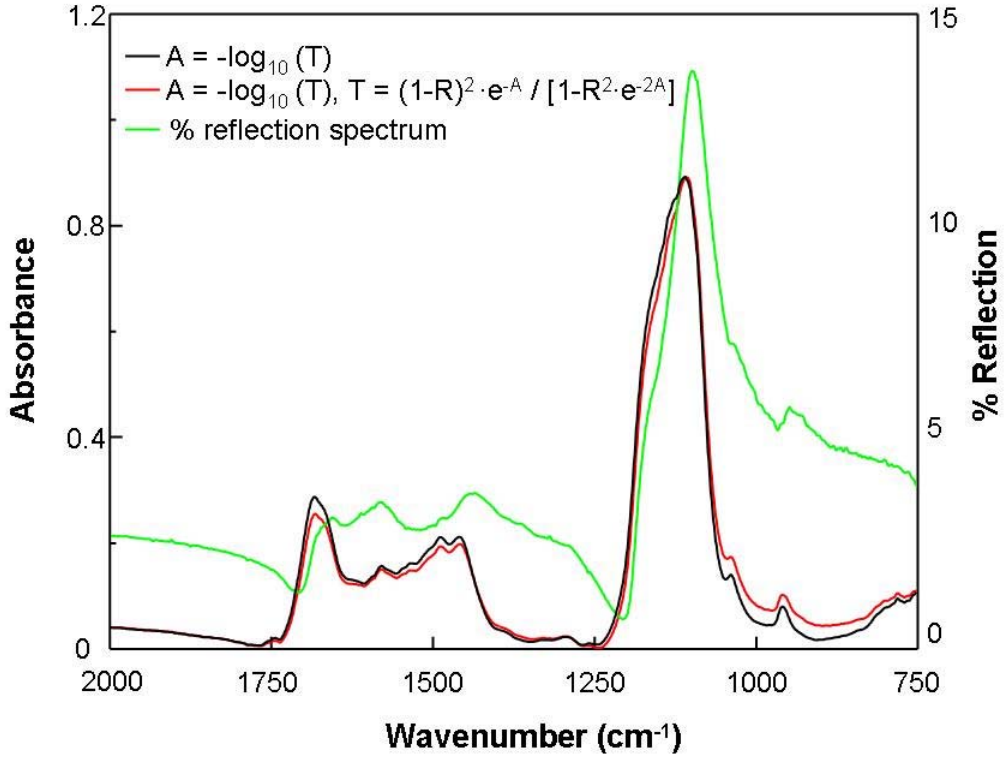

Figure 2-7: Comparison of IR absorbance spectra as calculated using the approximate expression A=-log(T) (black) and after accounting for reflection losses (red) using a single reflection spectrum (green).

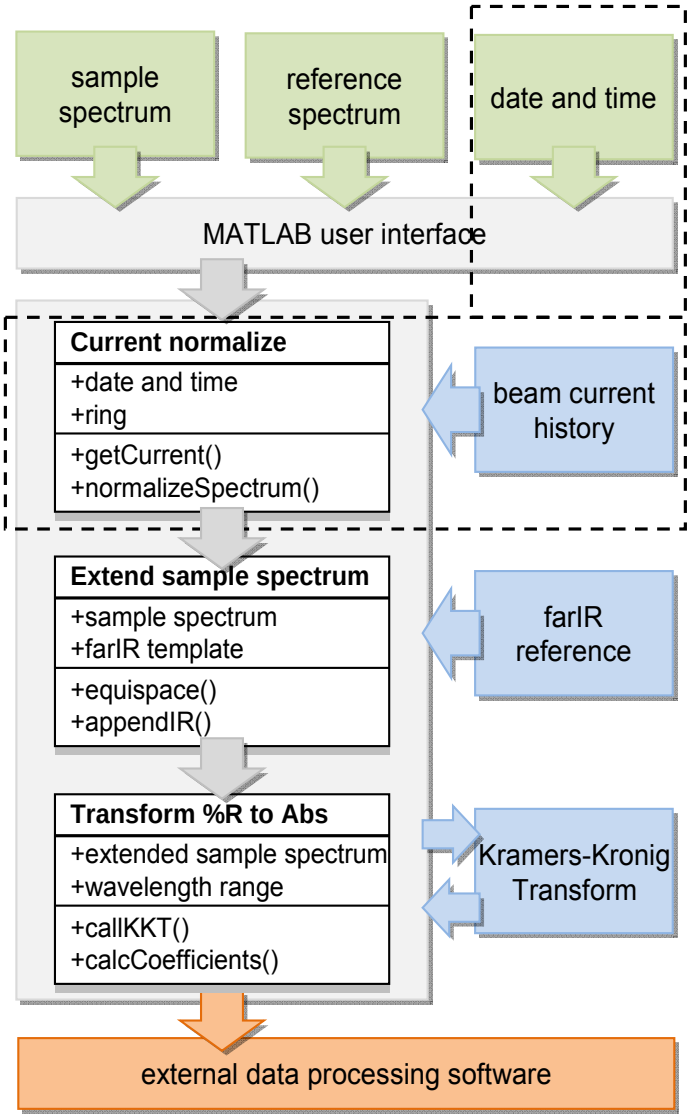

Figure 2-8: The MATLAB implementation for data processing of reflection-based FTIRM data. Optional steps are outlines by a dotted line. The operator provides user input (shown in green) consisting of the sample and reference single beam spectra as well as date and time of the measurement. The main MATLAB program current normalizes the sample spectrum using data from beam current history along with the date and time of the measurement. The normalized spectrum is extended into the farIR region using a farIR reference spectrum of bone. The extended spectrum is then used to calculate an equivalent absorbance spectrum using an external Kramers-Kronig routine. The absorbance spectrum is then written to file and is ready for further processing by the user.

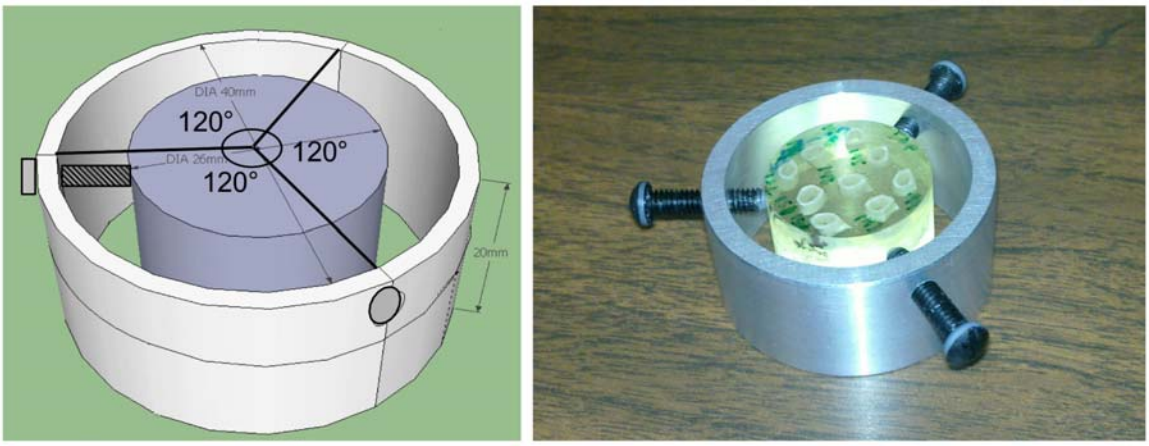

Figure 2-9: Conceptual design (left) and picture (right) of the bone block sample holder for IR imaging. 3 set screws placed at 120° angles hold the round sample in place. This specimen holder ensures that the top (reflective) surface of the specimen is perpendicular with the microscope stage.

Table 2-1: Chemical parameters and associated spectral ranges used for integrating transmission and reflection derived absorbance spectra. Identical baseline ranges were used for both transmission and reflection integrations.

IR parameter	transmission mode integration range (cm^{-1})	reflection mode integration range (cm^{-1})	baseline (cm^{-1})
Collagen cross-linking [79]	(1661-1659) / (1691-1689)	(1661-1659) / (1691-1689)	1800 - 1300
Crystallinity [110]	(1034-1030) / (1023-1019)	(1037-1033) / (1027-1023)	1200 - 900
Protein	1700 - 1600	1700 – 1600	1800 - 1300
Phosphate	1200 - 900	1200 – 900	1200 - 900
Carbonate	1424 - 1414	1424 – 1414	1800 - 1300
Mineralization [81]	phosphate / protein	phosphate / protein	
Carbonate substitution [109]	carbonate / phosphate	carbonate / phosphate	

Table 2-2: Mean values ± standard deviations and CV for FTIRM spectral parameters from transmission FTIRM through a 4 μm bone thin section and reflection FTIRM from the matching bone block.

IR Parameter	Specimen #	Thin section		Polished block		% Difference
		Mean	*CV*	*Mean*	*CV*	
Collagen cross-linking	Specimen 1	2.285 ± 0.158	6.91%	2.671 ± 0.230	8.61%	+16%
	Specimen 2	2.287 ± 0.141	6.17%	2.439 ± 0.201	8.24%	+6%
	Specimen 3	2.438 ± 0.414	16.98%	2.545 ± 0.103	4.05%	+4%
	Average		**10.02%**		**6.97%**	**+9%**
Crystallinity	Specimen 1	1.111 ± 0.031	2.80%	1.214 ± 0.021	1.73%	+9%
	Specimen 2	1.090 ± 0.019	1.74%	1.351 ± 0.028	2.07%	+21%
	Specimen 3	1.072 ± 0.040	3.73%	1.271 ± 0.024	1.89%	+17%
	Average		**2.76%**		**1.90%**	**+16%**
Mineralization	Specimen 1	4.982 ± 0.247	4.96%	4.297 ± 0.231	5.38%	-15%
	Specimen 2	5.203 ± 0.449	8.63%	5.178 ± 0.363	7.01%	-0%
	Specimen 3	5.267 ± 0.474	9.00%	4.973 ± 0.264	5.31%	-6%
	Average		**7.53%**		**5.90%**	**-7%**
Carbonate Substitution	Specimen 1	0.020 ± 0.001	5.00%	0.021 ± 0.001	4.76%	+5%
	Specimen 2	0.022 ± 0.001	4.55%	0.020 ± 0.001	5.00%	-10%
	Specimen 3	0.024 ± 0.003	12.50%	0.019 ± 0.001	5.26%	-23%
	Average		**7.35%**		**5.01%**	**-9%**

CHAPTER 3

CHEMICAL AND MECHANICAL EFFECTS OF FLUORIDE TREATMENT ON CORTICAL BONE AS ASSESSED BY HIGH RESOLUTION FTIR IMAGING AND NANOINDENTATION

3.1 Abstract

Several decades of research have proved that identifying how the chemical and structural parameters contribute to bone quality and ultimately to fracture resistance is a complex task. In this study, we assessed the effects of ovariectomy and subsequent treatment with low (100 ppm) and high (500 ppm) doses of sodium fluoride on the chemical composition of cortical bone in female Sprague Dawley rats. Chemical characterization was performed on polished bone blocks prepared for Fourier transform infrared imaging. From the IR spectra, four chemical parameters were analyzed: Mineralization, crystallinity, carbonate substitution and collagen cross-linking. Fluoride incorporation into the hydroxyapatite lattice did not significantly alter spectral assignments of the ν_1 and ν_3 phosphate peaks. Outer circumferential lamellae were clearly identified by a higher level of mineralization compared to intracortical bone, which correlated with visible differences in structure. Although the periosteum was significantly more mineralized than intracortical bone in the control group, this effect was even more dramatic in all treated groups. Crystallinity and carbonate substitution levels increased due to fluoride treatment in periosteal bone. The increase in bone formation during exposure to fluoride treatments was most evident in the mineral phase of high turnover bone, suggesting that fluoride treatment primarily effects the mineral phase. Smaller, but significant effects were noted in the organic phase. However, no differences were noted in the mechanical properties in these areas within treatments

groups or across treatments. Characterizing the interplay of these parameters can lead to a better understanding of bone quality and fracture risk and may lead to more potent therapeutically drugs to recuperate compromised bone quality.

3.2 Introduction

The mechanical properties of bone are a product of bone quantity and quality [17, 20, 47]. Bone quantity is easily defined as the volume of bone and the occurrence and size of porosities, and is routinely measured in patients in a clinical setting [8, 71, 118]. In contrast, bone quality parameters are much more difficult to establish as less is known about how bone chemistry and structure contributes to the tissue-level mechanical properties and ultimate fracture resistance [39, 107, 119, 120]. However, several decades of research have highlighted the potential significance of bone chemistry, nanostructure and micro- and nano-level mechanical properties on the ultimate tissue-level mechanical properties of bone, which are in turn regulated by complex pathways in response to the natural development, aging and repair of damaged bone tissue [121]. Further characterization of the interplay between these parameters can lead to a better understanding of bone quality and fracture risk, and may lead to more potent therapeutically drugs to recuperate compromised bone quality.

Bone remodeling is a continuous process in response to natural development, aging and repair of damaged bone tissue [122]. In the early stages of cortical bone development, bone remodeling replaces primary (or woven) bone, which was initially laid down by osteoblasts in a rapid, albeit disorganized fashion in order to create bone mass quickly [123]. In most higher vertebrates this remodeling process involves filling in of woven bone with structurally well-defined lamellar bone to form fibrolamellar bone [124] In addition, secondary remodeling takes

place where resorption cavities are produced by osteoclasts followed by deposition of new bone by osteoblasts, producing the characteristic tree ring-like shape of osteons surrounded by osteonal lamellar bone. Under normal conditions, several species such as rats lack osteonal remodeling and therefore primary bone becomes woven bone-like fibrolamellar bone. Further modeling of cortical bone slowly adds circumferential lamellae parallel onto the periosteum and endosteum.

Investigations into the mechanical properties and fracture behavior of osteonal, fibrolamellar, and circumferential lamellar bone point out that the organization of lamellae into extended sheets or osteons accounts for some of the differences in mechanical properties [29], for example that the high anisotropy of fibrolamellar bone reduces crack propagation in the bone microstructure [125]. These differences in structural and mechanical properties may be related to responses to external mechanical stimuli. For example, hyperphysiological bone strain typically leads to woven bone formation while modest levels of strain stimulate lamellar bone formation [126-128]. A more recent work further correlated the changes in hardness between osteonal lamellae and circumferential lamellae with changes in chemical composition, including mineralization, crystallinity and carbonate substitution [129], suggesting that chemical composition also contributes to the mechanical properties of lamellae.

The chemical changes that occur during bone formation [130], maturation [84, 85, 131] and fracture healing have been well documented using Fourier Transform Infrared Imaging (FTIRI) and Raman spectroscopic imaging in attempts to identify the chemical parameters that most contribute to bone quality [13, 107, 120, 132, 133], and to determine how specific therapeutic drugs such as alendronate [82], risedronate [83] and parathyroid hormone [134] affect bone chemistry during remodeling. FTIRI and Raman spectroscopic imaging have also been

successfully used to measure the fibrillar mineralization and orientation in osteons at the micron scale [81, 135, 136]. This study aims to further investigate the chemical and mechanical properties of circumferential lamellar and fibrolamellar bone in rat femurs, and to elucidate how these properties are modulated by estrogen deficiency and fluoride treatment.

3.3 Methods

Experimental design and sample preparation

40 five-month old female Sprague Dawley rats divided into 4 groups (n = 10). Three groups were ovariectomized, while an age-matched control group (CNT) was not. From the ovariectomized animals, one group was left untreated (OVX), one received a 100 ppm dose sodium fluoride (L-NaF), and one received a 500 ppm dose sodium fluoride (H-NaF). At 12 months of age, all animals were euthanized and femurs were harvested. The right femurs were embedded such that the cortical shell of the mid-diaphysis was exposed. The top surface of the bone blocks were polished (Buehler, Lake Bluff, IL) with 1,200 grit carbide paper followed by a cloth impregnated with a sequence of diamond suspensions (particle size 3, 1, 0.25, 0.05 μm) for 3 min at each step. All procedures were approved by the Stony Brook Institutional Animal Care and Use Committee.

FTIR Microspectroscopy

FTIRI was performed using a Hyperion 3000 FTIR microscope (Bruker Optics) equipped with a 64 x 64 element FPA detector. Polished bone blocks samples were mounted such that the surface was parallel to the focal plane produced by the optics. A 15X objective (0.4 numerical aperture) was used for data collection and 4 x 4 binning was applied to yield a 11 μm pixel

resolution. Data were collected with a wavenumber range from 850 to 3900 cm^{-1}, a spectral resolution of 8 cm^{-1} and 32 scans were co-added. A gold coated microscope slide was used as a reference material with 512 co-added scans. For all samples, the entire cortical shell of approximately 3 x 3 mm was imaged, which typically consisted of 450 FPA tiles, or 115,000 spectra. Reflection data were used to calculate absorbance equivalent spectra as described in [137]. A typical absorbance IR spectrum obtained from the bone specimens shows the presence of the protein, carbonate and $\nu_1\nu_3$ PO_4^{3-} absorption modes (Figure 2-1). Individual spectra were integrated to yield the degree of tissue mineralization (phosphate/protein ratio), carbonate substitution into the mineral lattice (carbonate/phosphate ratio), mineral crystallinity (ratio of stoichiometric / non-stoichiometric phosphate), and collagen cross-linking (Table 2-1).

Automated Region-of-Interest Selection

To ensure an unbiased analysis of regions within the IR integration maps of the cortical shell, a MATLAB procedure was developed that automatically recognizes the shape and orientation of the cortical shell, identifies the quadrants (posterior, lateral, anterior and medial) and overlays 3 rectangles in each quadrant (Figure 3-1). First, a low and high cutoff threshold is applied to the IR integration map for mineralization. The resulting bitmap is further filtered to yield an image of the bone, where back pixels correspond to the presence of bone. An outline of the bone's circumference and the weighted center are then used to plot the distance between the center and the circumference, as a function of angle. From this plot, the location (angle) or negative and positive peaks are correlated to the posterior, lateral, anterior and medial directions of the cortical shell. Based on this information, the IR integration map is rotated to have the lateral quadrant on the top. Afterwards, rectangles of a specific size (in this case 100 x 500 μm), are drawn in the quadrants directly on the horizontal and vertical axis. The orientation of these rectangles follows

the angle of the nearest surface, e.g. the periosteal rectangles are angled to match the periosteal surface. More details are provided in Appendix C.

Data analysis and regions-of-interest

A Matlab routine was developed to generate a mask representing the shape of each femur by identifying bone and non-bone pixels based on thresholding of mineralization IR maps. The masks were then rotated and flipped such that the lateral, anterior, medial and periosteal surfaces pointed up, right, down and left, respectively. The routine placed 100 x 500 μm rectangles in the each quadrant of each mask; a first set 50 μm from the periosteum, a second set 50 μm from the endosteum and a third set in between the periosteal and endosteal ROI. The periosteal and endosteal ROI were orientated parallel to their respective surface, while the orientation of the intracortical ROI was an average of the periosteal and endosteal ROIs in each quadrant (Figure 3-2C). The mask and associated ROI of each specimen were then matrix multiplied with all of the specimen's integration maps, resulting in an average value and standard deviation per ROI per integration map for each specimen. Each ROI contained 500 spectra.

Nanoindentation and Conventional desktop μCT

After mapping the right femurs with FTIR, nanoindentation was performed on the same femurs. Highly polished surfaces of cortical bone were indented using a nanoindenter system (Triboindenter; Hysitron, Minneapolis, MN) with a Berkovich indenter tip. Bone was indented using a trapezoidal load function with a constant loading and unloading rate of 1000 μN/s and a 10 second hold period between loading and unloading phases to dissipate the tissue's viscoelastic response. The elastic response was automatically calculated from the initial portion of the unloading curve using calculations previously described (Ozcivici, 2009). Each bone sample was

indented 48 times spaced throughout the diaphyseal cortex. Four indents were performed for each region of interest which included a band within the periosteal, intracortical and endosteal regions each within the anterior, medial, posterior and lateral quadrants for a total of 12 regions per bone. Indent locations were visually selected to avoid contact with large pore or cracked surfaces at a distance no less than 20 μm from another. Tissue elastic modulus (N/mm) and tissue hardness were determined for each indent. Four indents per region were averaged and reported with their standard deviations. Any indents outside of 2 SD were removed. Left femoral diaphyses were analyzed using desktop μCT at 36 μm resolution as described in [22]. Tissue Mineral Density (TMD) values were calculated for a 1.8-mm long volume of interest (VOI).

Statistical analysis

Percent differences were calculated by the ratio of the difference to the average. ROI within treatment groups were compared using a one-way ANOVA followed up with a Tukey Post-Hoc test (GraphPad Prism 3.0). Spearman rho correlations were calculated for chemical and mechanical parameters per treatment per ROI for all animals (4 x 5 x 10). A stepwise regression was performed on the same input to determine the contribution of the chemical parameters on elasticity and hardness (SPSS 14). Significance was set at 0.05.

3.4 Results

Fluoride incorporation into the apatite lattice does not significantly alter the spectroscopic assignments of the v_1v_3 phosphate absorption band

To investigate potential spectroscopic effects of the incorporation of fluoride ions into the hydroxyapatite lattice, the v_1v_3 phosphate absorption band in IR spectra from CNT and H-NaF

treated groups were analyzed. Based on previous work measuring the incorporation of F into HAP in both rat fetal osteoblast cultures [138] and rats supplemented with 100 ppm fluoride in drinking water [139], an upper limit for the percent incorporation of F into HAP in low turnover bone in the present study is estimated to be <0.5%. Based on treatment length and the age of the animals in this study, most of the F incorporation is likely to have occurred in bone formed during the treatment, i.e. on the periosteal surface, while a lesser amount of incorporation likely took place in intracortical bone. To account for potential different mechanisms and rates of incorporation between bone formed before and during the treatment, spectra from both circumferential lamellar bone and intracortical bone were analyzed (Figure 3-3). A 2nd derivative analysis of the v_1v_3 phosphate band did not reveal differences in the wavenumber assignments in any of the underlying peaks. Four apatite absorption bands were identified, namely the v_1 symmetric stretch at 962 cm^{-1}, the stoichiometric v_3 asymmetric stretches at 1033 and 1111 cm^{-1}, and the vibrational stretch at 1061 cm^{-1}.

Periosteal circumferential lamellae are more mineralized and crystalline than intracortical bone

Periosteal and endosteal circumferential lamellar bone and fibrolamellar bone in the intracortical region were clearly distinguishable in visible light micrographs and IR maps. The visible light image (Figure 3-2A) showed a difference in organizational structure: circumferential bone on the periosteum and endosteum appeared compacted and lamellar, and parallel to its respective surface while intracortical bone appeared less organized with a greater number and larger porosities. A difference in mineralization levels was observed in the IR data (Figure 3-2B) in a pattern similar to the organizational structure observed in the visible light image. These data indicate that the circumferential lamellar bone was more mineralized than the fibrolamellar bone with a well-defined boundary separating the two anatomical regions of the cortical shell.

A more detailed analysis of chemical and mechanical properties across the cortical shell used an unbiased ROI approach (Figure 3-2C) and compared endosteal (all four endosteal ROIs), intracortical (all four intracortical ROIs) and periosteal bone (all four periosteal ROIs) (Figure 3-4). The thickness of the circumferential lamellar layer on the periosteal surface was greatest in the lateral quadrant, and as such the lateral periosteal ROI (hereupon referred to as "circumferential lamellar bone ROI") was also investigated separately from the periosteal bone region. Although a thin circumferential layer could be observed on the endosteal surface, it was not reliably observed in the IR data, presumably due to the spatial resolution of 10 μm of the IR data. Circumferential lamellae in the lateral periosteal quadrant were 10.4% more mineralized than the intracortical bone ($p<0.01$) and 7.9% more mineralized than the endosteal surface ($p<0.05$). No significant regional differences were observed in the crystallinity, collagen cross-linking and carbonate substitution parameters (Table 3-1).

Regional effects of ovariectomy and sodium fluoride on cortical bone chemistry

The effects of OVX on the chemical properties of cortical bone in the various ROI are summarized in Figure 3-5. Similar to observations in CTRL and OVX groups, the well-defined boundary between intracortical and circumferential lamellar bone on the periosteum was also observed in the degree of crystallinity of NaF treated samples, but the boundary was shifted towards the periosteum by 50 - 100 microns depending on the region of the cortical shell. The degree of mineralization in the circumferential lamellar bone ROI was increased due to OVX ($p<0.05$). The differences in mineralization between intracortical and the circumferential lamellar bone ROI rose from 10.9% in CNT ($p<0.05$) to 20.2% in OVX ($p<0.0001$), clearly indicating a highly mineralized circumferential lamellar layer on the periosteum for both groups. Crystallinity in the periosteal ROI was decreased ($p<0.05$), while across all regions the values were

consistently lower by 2.5 - 2.7% ($p<0.001$). Furthermore, collagen cross-linking values were consistently higher by 3.2 - 4.6% in the OVX group ($p<0.001$), suggesting that ovariectomy did not cause changes to the variability in crystallinity and collagen cross-linking between the ROIs (Table 3-1). A difference was observed in the carbonate substitution between the periosteal/lateral and intracortical ROI in OVX ($p<0.01$), while no difference was observed in CNT. No significant differences were observed in the mechanical properties due to OVX.

In fluoride treated rats, the degree of mineralization was significantly increased in the periosteal ($p<0.01$) and circumferential lamellar bone ROI in H-NaF ($p<0.01$), while increasing the difference between the circumferential lamellar and intracortical bone regions by 10.6% ($p<0.001$) and 16.3% ($p<0.0001$) for L-NaF and H-NaF groups, respectively. Crystallinity values were higher in circumferential lamellar bone ROI ($p<0.01$) and periosteal ($p<0.05$) regions for H-NaF, while the difference between circumferential lamellar and intracortical bone rose to 4.9% in L-NaF ($p<0.05$) and 8.0% in H-NaF ($p<0.01$), compared to a non-significant difference in control. Further, carbonate substitution in the H-NaF treated group increased by 5.1% ($p<0.05$) and 5.8% ($p<0.05$) in the periosteal/lateral and periosteal regions compared to control, respectively. Consequently, difference were observed between periosteal/lateral and intracortical bone for low ($p<0.05$) and high ($p<0.01$) doses of fluoride.

No differences were observed in the mechanical properties between similar regions of control, OVX and fluoride treated animals (Figure 3-6), nor between different regions within groups.

Correlations between chemical and mechanical properties, tissue mineral density

No correlations were observed when using the average values for each parameter per treatment group, likely due to the high intergroup variability in the mechanical data. However, when correlating on a per sample basis Figure 3-7, collagen cross-linking was inversely correlated with elasticity (ρ=-0.244, $p<0.01$) and hardness (ρ=-0.183, $p<0.05$), while crystallinity (ρ=0.161, $p<0.05$) and carbonate substitution were positively correlated with hardness (ρ=0.171, $p<0.05$). A stepwise linear regression showed across all treatments and regions that collagen cross-linking and crystallinity accounted for 8.7% of the variability in elasticity, while carbonate substitution, mineralization and collagen cross-linking described 12.8% of the variability in hardness. A correlation between whole bone mineralization and TMD did not show a correlation.

3.5 Discussion

FTIRI provides the sensitivity and spatial resolution that is required for chemical analysis of the different anatomical regions of bone, such as osteonal circumferential lamellae and trabecular bone. The combined use of reflection-based FTIRI and other surface sensitive imaging modalities such as nanoindentation, quantitative backscatter electron imaging (qBSE) and Raman spectroscopy enables direct comparisons between the chemical and mechanical properties of regions from single bone specimens, thus providing accurate spatial associations between outcome measures. Here, we employ the first of such comparisons using FTIRI and nanoindentation to probe and correlate the chemical and mechanical properties in several anatomical regions of the cortical shell specimens of rat femurs in the form of polished bone blocks. Our results indicate that OVX and treatment with low and high doses of Fluoride affected various chemical parameters in several regions of cortical bone, but to different degrees, while

the mechanical properties were not significantly affected. The periosteal bone in the lateral quadrant was found to be mostly affected, while endosteal bone remained unchanged in most cases. No changes were observed in the mechanical properties as probed by nanoindentation, and only a few correlations were found with chemical parameters. Further, variations in chemical properties accounted for less than 13% of the variability in the mechanical properties. In addition, TMD evaluation using desktop μCT was not sensitive enough to identify differences in mineralization between circumferential lamellar and intracortical bone.

The mineral composite of bone is in the form of hydroxyapatite, $Ca_5(PO_4)_3OH$. Substitution of the hydroxyl group (type-A) by a F^- or Cl^- ion and/or phosphate group (type-B) by an anionic complex such as carbonate commonly occurs in bone. Due to an increase in symmetry of apatite by type-A substitution with F^-, the crystal lattice is stabilized and solubility is reduced, eventually leading to increased crystallinity [70]. As a consequence of the slight change in lattice structure of apatite, the PO_4 ν_3 vibration occurs at different frequencies for pure HAP and FAP with vibrational shifts being as much as 5 cm^{-1} [140, 141]. Our results suggest that the IR spectroscopic assignments for the $\nu_1\nu_3$ phosphate bands are the same for bone from untreated and Fluoride treated rats. This is likely because the percent incorporation of F into HAP in low turnover bone is low: < 0.5% incorporation has been observed in a rat fetal osteoblast culture supplemented with 250 μM NaF for 40 days [138], while rat models suggest that an intake of water with 100 ppm fluoride for 10 weeks could increase fluoride concentrations by 2300 ppm in endosteal and periosteal circumferential lamellae of cortical bone [139]. Considering these factors, it is reasonable to conclude that spectral shifts in the $\nu_1\nu_3$ phosphate bands in rat femur specimens are <1 cm^{-1}, even for regions with unusually high amounts of FAP incorporation.

The anatomical differences in the structure of periosteal and intracortical bone as measured by visible light identify the outer anatomical region as circumferential lamellar bone and the inner region as less organized, intracortical bone. Further examination of the IR images also showed a distinct geographical boundary in mineralization levels in the same location as observed in visible light images, distinguishing highly mineralized outer circumferential lamellae on the periosteum from less mineralized intracortical and endosteal bone. This pattern was present in all treatment. Interestingly, NaF treated samples saw a similar boundary in crystallinity data, but this boundary lay further towards the periosteum, suggesting that the increased rate of periosteal apposition caused crystal maturity to lag behind mineralization of the tissue. Although this phenomenon has not been previously observed with FTIR, an increase in mineralization with age of both circumferential lamellae and osteons in swine has been previously reported in literature [129]. The spatial correlation between mineralization and visible structure supports the notion that these two types of bone exhibit different chemistries [129]. Consequently, these different chemistries may results in different mechanical properties as mineral content has been shown to affect nanomechanical properties [142] and cooperative deformation potential of the mineral and collagen phases of bone at the nanoscale level [15]. This is possibly due to different mechanisms of bone maturation in circumferential and fibrolamellar bone, but can also be explained by mineralization being on ongoing process throughout adulthood, which has been observed in cortical bone of Sprague Dawley rats [84] and in human compact bone [85]. Mineralization occurs at different rates and with different endpoints depending on the morphological region of the bone.

The observed uneven mineralization in the CNT group has previously been reported in cortical bone of 8-month old Sprague Dawley rats using Raman spectroscopy [84]. The high

degrees of mineralization in the lateral-posterior region of the periosteum and the medial-anterior region of the endosteum support the notion of cortical drift in the periosteal-lateral direction [143]. A suppression of mineralization in intracortical and endosteal bone and increases in the periosteum of the OVX group were possibly due to estrogen deficiency induced accelerated skeletal metabolism: periosteal apposition [144, 145] and endosteal bone resorption rather than apposition, which go paired with an increased occurrence of endocortical porosities and resorption cavities [146] and an overall reduction of cortical width [147]. Although the observed increase in periosteal mineralization was due to increased periosteal apposition, reduced mineralization and increased occurrence of resorption cavities in the endosteal regions was due to a combination of resorption and dissolution of apatite.

Although the CNT group did not indicate significant heterogeneity in crystallinity, collagen maturity and carbonate substitution, it should be noted that these chemical indicators reach their endpoint earlier in life, as has been observed in mice [100] and rats [130], resulting in less variability across the cortical shell under normal conditions. The increased periosteal mineralization and endosteal resorption due to ovariectomy did cause significant heterogeneity in carbonate substitution levels. These variations are more dramatic in some quadrants due to the combined effects of cortical enlargement and drift. An overall increase in metabolic activity would also reduce crystal sizes in areas of bone resorption due to partial dissolution of apatite, and account for the smaller crystal sizes in newly formed bone [13]. The crystallinity data show exactly this: a consistent reduction in crystal size and perfection in the OVX group across the entire cortical shell.

Due to the decreased solubility and a lower dissolution rate of the apatite crystals in NaF treated samples [148], the mineral phase in the remaining endosteal bone of the fluoride treated

group remained fairly intact compared to CNT, despite severe bone resorption as evident by the formation of large and numerous resorption cavities [*not shown*]. NaF increased crystal size in a dose-dependant manner over OVX, where these changes were biggest in periosteal bone, further supporting that NaF minimally affects crystal properties in existing bone, and dramatically that of bone formed during NaF treatment. A hypothesis offered by Mousney, et al [149] suggests that at high fluoride doses, the organic-inorganic interface is weakened, leading to increased flux of calcium and phosphate ions to the mineral interface, thereby leading to accelerated mineral growth, bigger crystals and higher degrees of mineralization. In addition, the increases in carbonate substitution levels in areas other than the resorbing endosteal surface of the NaF treated samples further suggests that NaF actually maintained the mineral phase in these areas. NaF treatments thus prevented crystal dissolution and maintained mineralization levels while carbonate substitution levels increased in areas of bone resorption.

The primary affect of fluoride treatment is on bone formed during treatment and is due to its incorporation into mineral phase, thereby stabilizing the crystal structure, reducing solubility and eventually increased the rate of periosteal apposition. The results suggest that the effects of fluoride treatment likely do not extend to the collagen network, mechanical properties or to any of the analyzed chemical parameters in intracortical bone. Fluoride treatment does not mitigate decreases in collagen cross-linking due to osteoporosis, but merely forms periosteal bone at a faster rate with a different chemical composition compared to new bone formed in normal conditions. Like fluoride, other pharmaceutical drugs that promote rapid formation of new bone could potentially be producing chemically inferior bone, ultimately negatively affecting its mechanical competence.

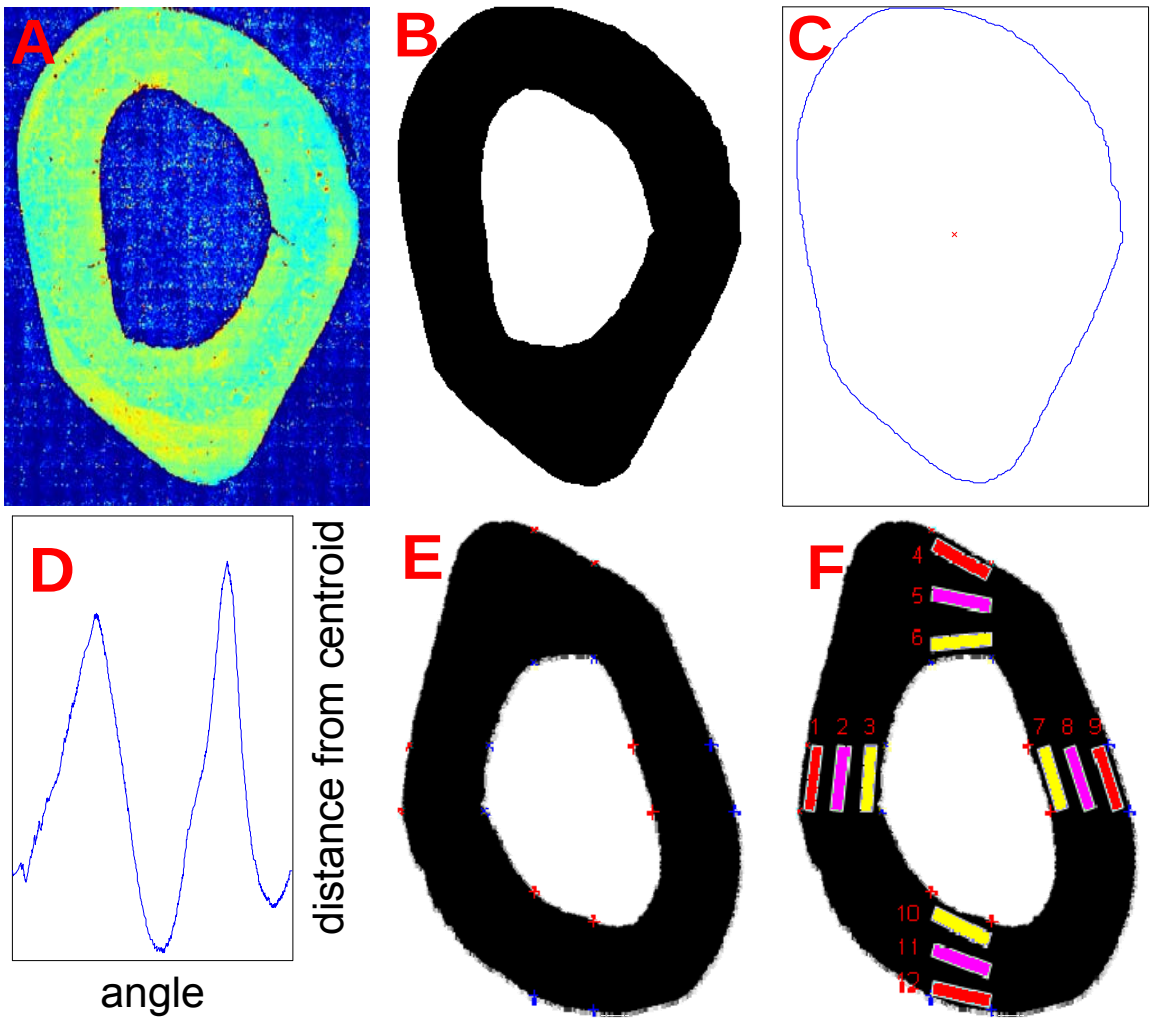

Figure 3-1: Approach to ROI based image analysis of FTIR integration maps. (A) Integration map of the mineralization parameter, showing a clear separation between bone (green-yellow) and embedding material (blue). (B) Bitmap image of (A) after the removal of embedding material. (C) Trace of the outer circumference and centroid of bone from (B). (D) Plot of the distance from centroid to outer circumference as a function of angle. The orientation of the bone can be determined based on the angle at which the maximum and minimum centroid-circumference distance occurs. (E) Rotation of the bone in (B) so that the lateral quadrant is on top. (F) ROI of a specific size (here, 100 x 500 µm) are applied to the endocortical, intracortical and periosteal regions of the lateral, medial, anterior and posterior quadrants. All pixels within a ROI are averaged and the standard deviation is calculated.

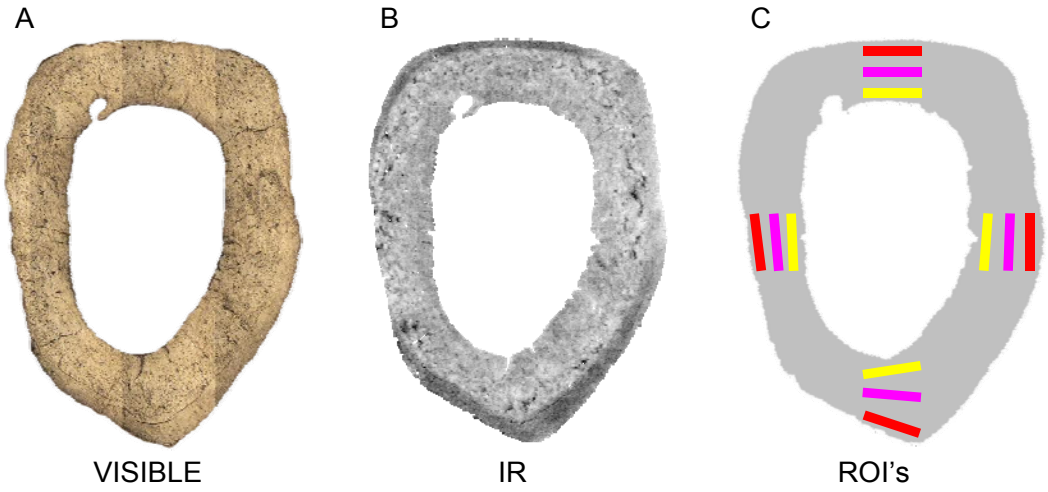

Figure 3-2: A) Visible light image of representative polished bone block (control specimen). B) Same specimen as in A, but showing the tissue mineralization. Darker shades indicate higher mineralization. C) The shape of the specimen is used to position 12 rectangles in 4 quadrants. Red, pink and yellow rectangles represent the periosteal, intracortical and endosteal bone regions, respectively.

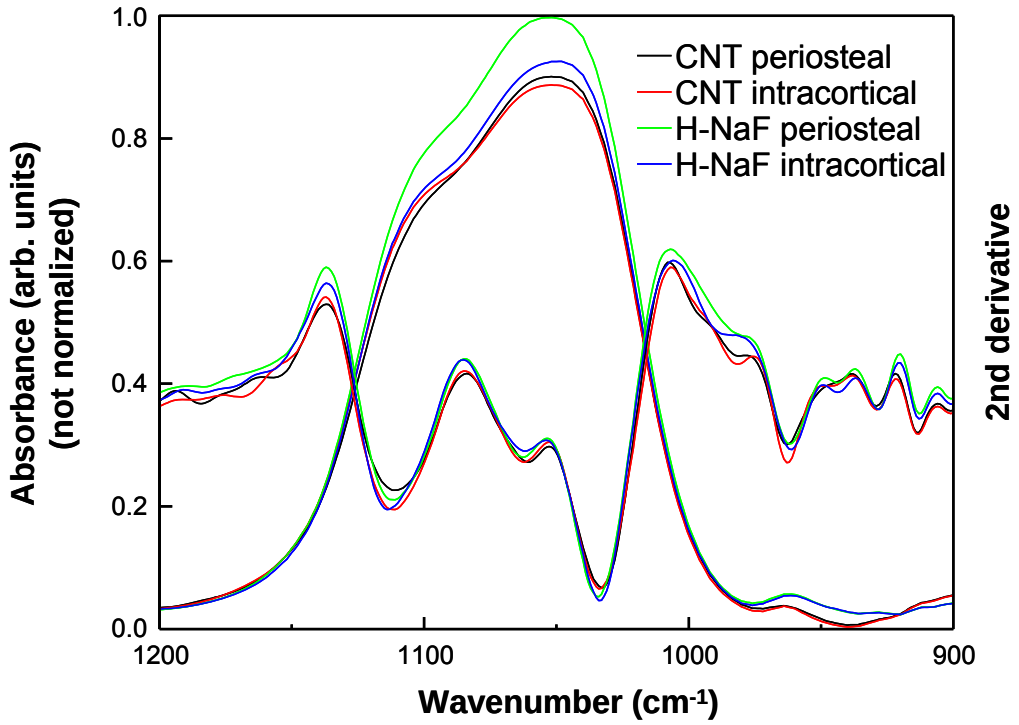

Figure 3-3: Absorbance and second-derivative spectra from the periosteal and intracortical regions of CNT (black and red) and H-NaF specimens (green and blue). Based on the second-derivative spectra, no spectral shifts of absorption peaks are observed between regions within groups or between groups.

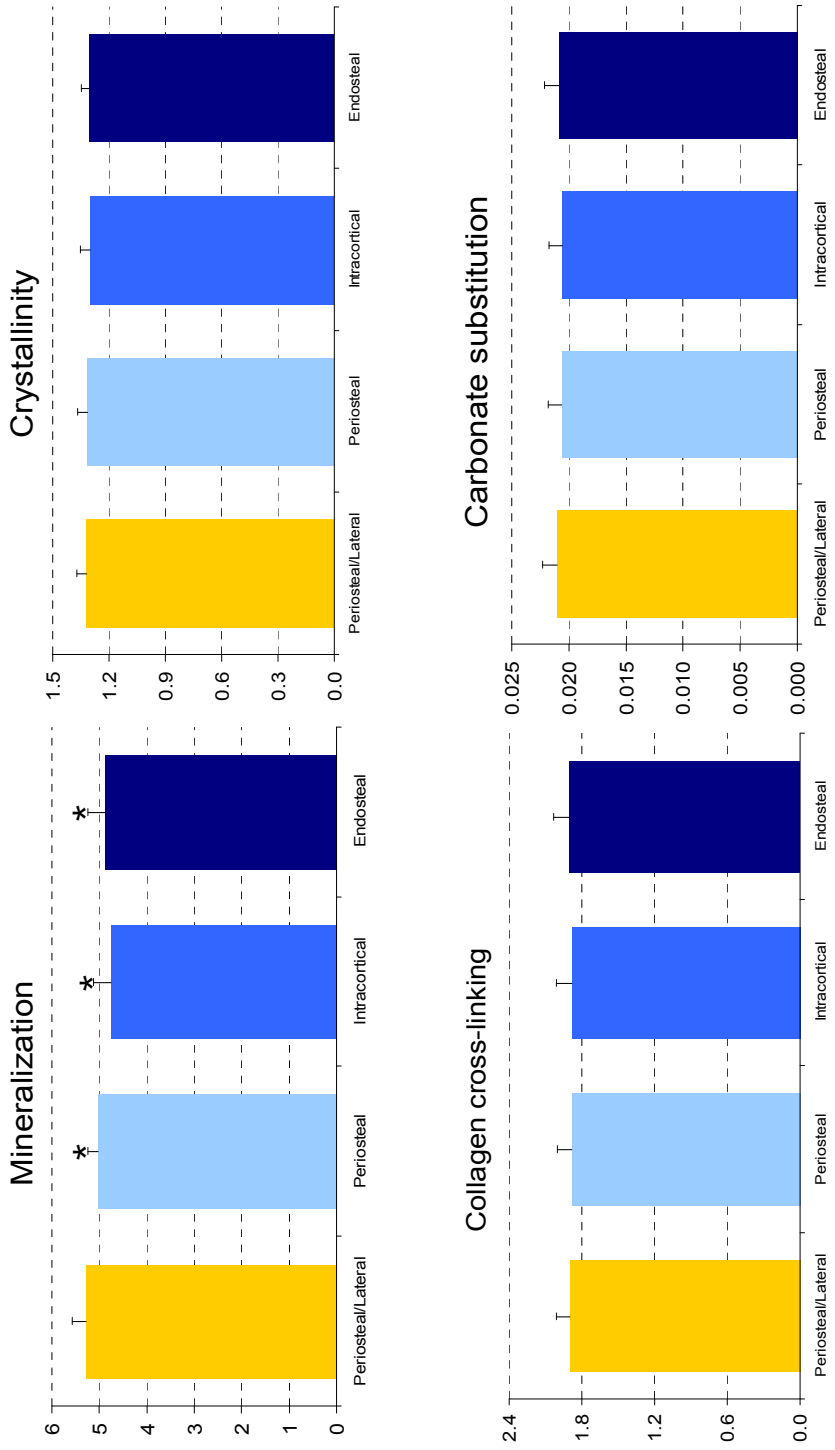

Figure 3-4: Tissue mineralization, mineral crystallinity, collagen cross-linking, and carbonate substitution levels in CNT specimens per region of interest. Significant differences from circumferential lamellar bone (periosteal/lateral ROI) are indicated by * ($p<0.05$).

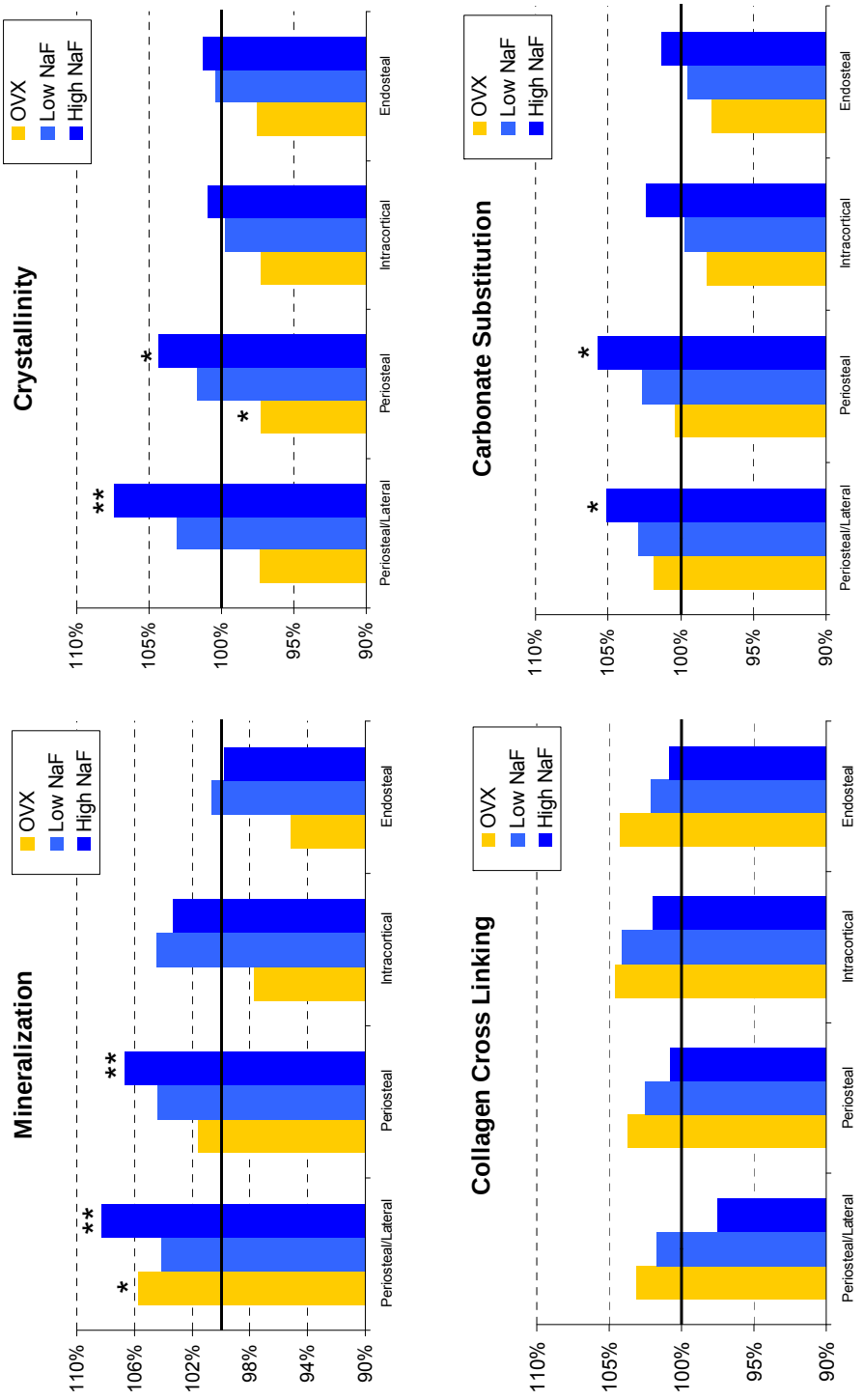

Figure 3-5: Tissue mineralization, mineral crystallinity, collagen cross-linking and carbonate substitution levels in OVX, L-NaF and H-NaF specimens per region of interest. Percent differences are compared to CNT specimens. Significant differences from circumferential lamellar bone (periosteal/lateral ROI) are indicated by * ($p<0.05$) or ** ($p<0.01$).

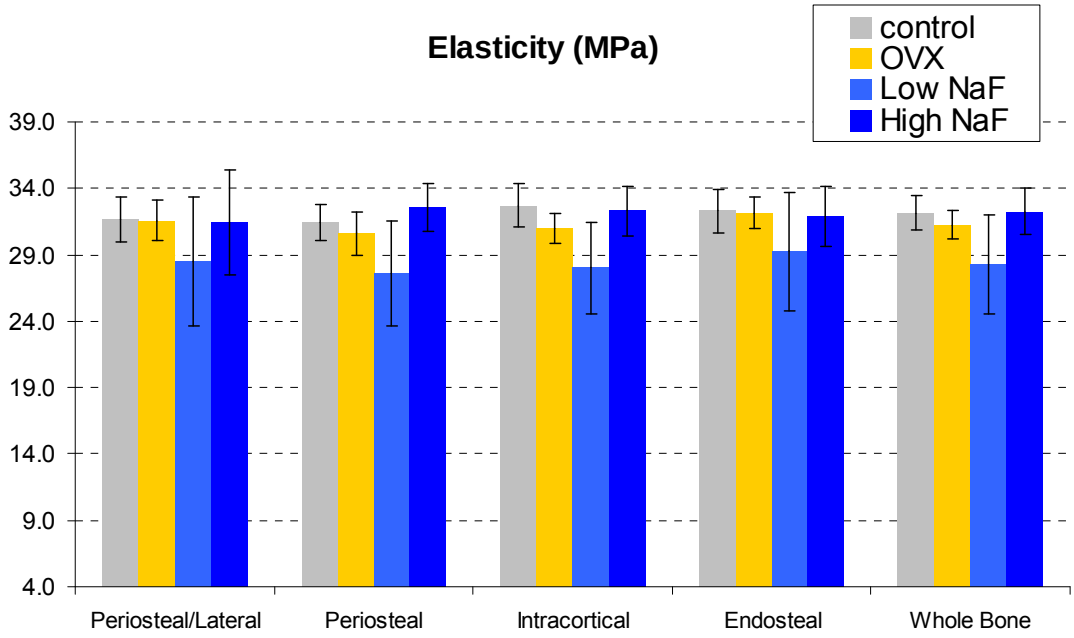

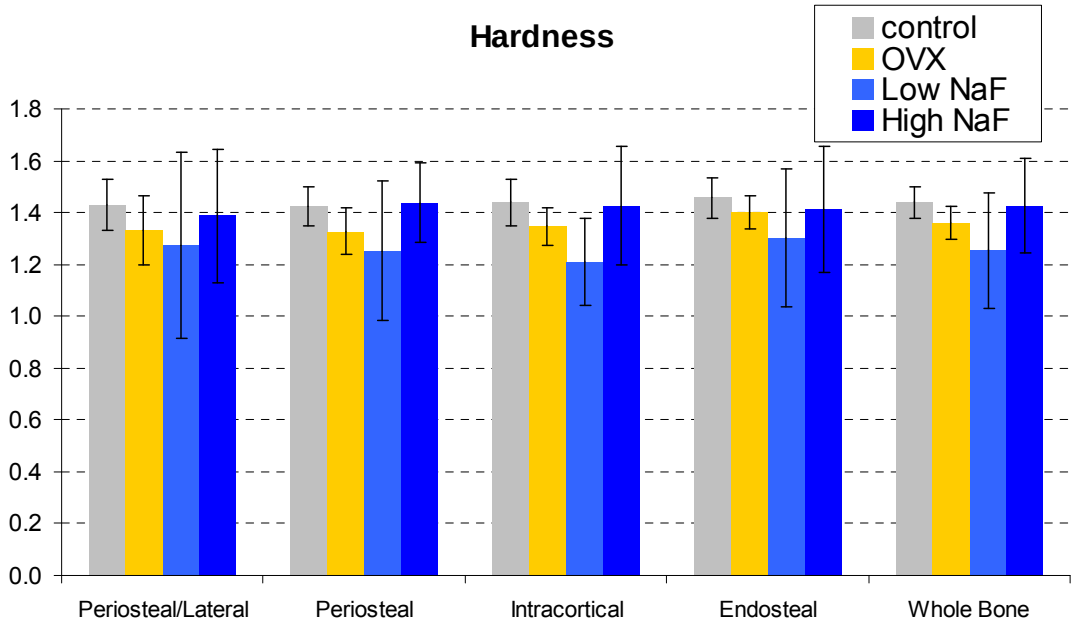

Figure 3-6: Elasticity and Hardness for control, OVX, L-NaF, and H-NaF specimens per ROI. No significant differences were observed between treatments or between regions of a single treatment.

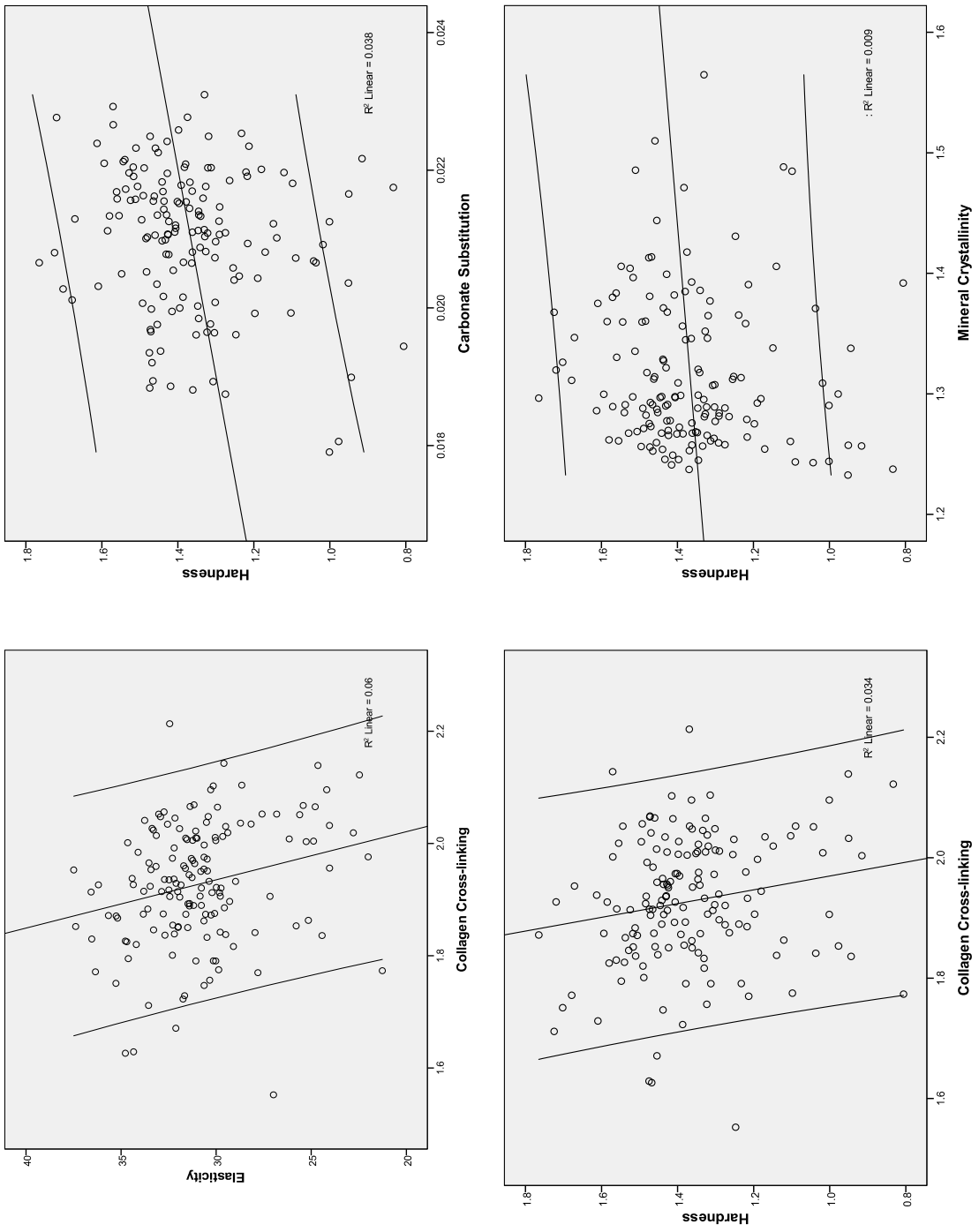

Figure 3-7: Correlation plots with associated R^2 values and 95% confidence limits (linear fit) between chemical and mechanical properties across all treatment groups. Collagen Cross-linking was negatively correlated with elasticity and hardness, while mineral crystallinity and carbonate substitution were positively correlated with hardness.

Table 3-1: Summary of the chemical composition of regions of interest per treatment as measured by FTIR.

		Periosteal Lateral	Periosteal	Intracortical	Endosteal	Whole Bone
Mineralization	CNT	5.2816 ± 0.2817	5.0305 ± 0.2140	4.7585 ± 0.3553	4.8794 ± 0.3704	4.9074 ± 0.2942
	OVX	5.6478 ± 0.2207	5.1495 ± 0.2593	4.6355 ± 0.1532	4.6619 ± 0.1480	4.8019 ± 0.0950
	L-NaF	5.4751 ± 0.4116	5.3678 ± 0.2607	5.0365 ± 0.1131	4.9509 ± 0.1072	5.0870 ± 0.1609
	H-NaF	5.7174 ± 0.2590	5.3640 ± 0.1559	4.9154 ± 0.2285	4.8686 ± 0.2411	5.0321 ± 0.1810
Crystallinity	CNT	1.3196 ± 0.0521	1.3140 ± 0.0507	1.2999 ± 0.0505	1.3026 ± 0.0469	1.3089 ± 0.0486
	OVX	1.2932 ± 0.0211	1.2801 ± 0.0189	1.2668 ± 0.0166	1.2708 ± 0.0205	1.2756 ± 0.0195
	L-NaF	1.3503 ± 0.0814	1.3265 ± 0.0681	1.2940 ± 0.0611	1.3054 ± 0.0581	1.3141 ± 0.0657
	H-NaF	1.4170 ± 0.0862	1.3712 ± 0.0665	1.3124 ± 0.0437	1.3190 ± 0.0431	1.3455 ± 0.0530
Collagen Cross-linking	CNT	1.8949 ± 0.1130	1.8811 ± 0.1192	1.8817 ± 0.1272	1.9015 ± 0.1298	1.8918 ± 0.1220
	OVX	1.9308 ± 0.0972	1.9683 ± 0.0638	1.9801 ± 0.0358	2.0013 ± 0.0466	1.9822 ± 0.0477
	L-NaF	1.9632 ± 0.1531	1.9999 ± 0.0848	2.0266 ± 0.0777	2.0070 ± 0.0759	2.0055 ± 0.0760
	H-NaF	1.8481 ± 0.0380	1.8961 ± 0.0621	1.9195 ± 0.0345	1.9180 ± 0.0473	1.9023 ± 0.0483
Carbonate Substitution	CNT	0.0210 ± 0.0013	0.0207 ± 0.0012	0.0205 ± 0.0012	0.0208 ± 0.0013	0.0207 ± 0.0012
	OVX	0.0214 ± 0.0008	0.0212 ± 0.0005	0.0205 ± 0.0007	0.0208 ± 0.0006	0.0209 ± 0.0007
	L-NaF	0.0220 ± 0.0008	0.0218 ± 0.0007	0.0210 ± 0.0008	0.0213 ± 0.0008	0.0215 ± 0.0007
	H-NaF	0.0221 ± 0.0005	0.0218 ± 0.0004	0.0210 ± 0.0002	0.0211 ± 0.0003	0.0215 ± 0.0003

CHAPTER 4

ALENDRONATE AND PARATHYROID HORMONE AFFECT THE CHEMICAL COMPOSITION OF OLD AND NEW BONE IN OVARIECTOMIZED RATS

4.1 Abstract

Several drug treatments exists that aim to strength bone, but often the mechanism of these drugs is unclear. Here, we examine the chemical changes in cortical bone induced by alendronate and parathyroid hormone in an ovariectomized rat model. Chemical characterization was performed using Fourier transform infrared imaging, and four chemical parameters were analyzed: Tissue mineralization, mineral crystallinity, carbonate substitution and collagen cross-linking. In all treatments a highly mineralized circumferential lamellar layer was found on the lateral quadrant of the periosteal surface and lower mineralized tissue in the intracortical area, indicating a normal cortical drift. Treatment with medium dose alendronate, but not in low and high doses, increased intracortical mineralization due to reduced bone turnover but continued secondary mineralization. Increased levels of carbonate substation into the mineral lattice in medium dose alendronate confirmed this increase in bone maturity. The anabolic agent PTH was found to increase tissue mineralization of circumferential lamellar bone at medium dose but not at high doses, likely because PTH both improved bone formation and tissue mineralization. These findings show that alendronate and parathyroid hormone treatments affect cortical bone chemistry in different ways. Further research into the relationship between these chemical changes and possible changes to the structural and mechanical properties of cortical bone will

help understand the effects of pharmaceutical drugs on the various properties of bone and further define bone quality.

4.2 Introduction

Osteoporosis arises from an imbalance between bone deposition by osteoblasts and bone resorption by osteoclasts. Amongst the risk factors involved in this imbalance are aging, estrogen deficiency in postmenopausal women [4] and malnutrition [5], but also genetic and modifiable factors such as Cushing's disease and glucocorticoid-induced osteoporosis, respectively [6]. Several treatment options exist that attempt to remedy to effects low bone mass and rapid bone loss induced by osteoporosis. These treatments can have antiresorptive effects, such as bisphosphonates and estrogens, which work by decreasing bone resorption and bone formation, leading to an overall increase in mineralization levels while maintaining the architectural integrity of the bone structure. Alendronate treatment has been shown to reduce the risk of osteoporotic fractures, which is attributed to the inhibition of bone resorption and increase in bone mass. The antiresorptive action of alendronate affects trabecular bone by increasing the uniformity and overall degree of mineralization, most likely because a greater fraction of trabecular matrix reaches higher levels of calcium content, but also cortical bone by decreasing remodeling activity within osteons, thereby leading to a decrease in cortical porosity [65]. This strengthening of the cortical shell is thought increase antifracture effectiveness [66].

Anabolic agents work by increasing primarily bone formation, thus increasing bone mass and strengthening bone architecture. However, the high rate of new bone formation results in a greater fraction of younger bone, thus decreasing the degree of mineralization. The anabolic action of parathyroid hormone (PTH) treatment produces the physiological response of an

increase in serum Ca^{2+} [58]. PTH has been found to affect both cortical bone and trabecular bone. An increased cortical thickness has been demonstrated, which in itself is predicted to significantly contribute to bone strength [49]. Further, increased connectedness in trabecular bone has been found, although the implications for bone strength remain unknown [60].

Using Fourier Transform Infrared Imaging (FTIRI), the chemical content of cross sections of the entire cortical shell can be analyzed at a high spatial resolution (<10 μm). Here, we employed FTIRI to investigate the effects alendronate and parathyroid hormone on the chemical composition of osteoporotic cortical rat femurs. The results of this study offer clues to how the structural hierarchy of bone and its chemistry are affected by pharmaceutical treatments. We correlated these data with nanoCT data that describe the geometry and occurrence of microporosities, and also with whole bone mechanical testing data to better understand the role of variations in chemistry in the prediction of fracture resistance. These results can help in the understanding between the interplay of the parameters that define bone quality, the ultimate tissue level mechanical properties, and fracture resistance of bone may lead to more potent pharmaceutical drugs to recuperate compromised bone quality.

4.3 Methods

Experimental design and sample preparation

Six-month old female Sprague Dawley rats were divided into 8 groups (n = 10). At 5 months of age, 7 groups were ovariectomized, while the age-matched control group (CNT) was not. 6 OVX groups were given subcutaneous injections of alendronate at doses of 1 μg/kg/2x wk (L-ALN), 100 μg/kg/2x wk (M-ALN), or 2 mg/kg/2x wk (H-ALN), or parathyroid hormone at doses of 0.3 μg/kg/d (L-PTH), 15 μg/kg/d (M-PTH), or 75 μg/kg/d (H-PTH). The remaining

OVX group was left untreated (OVX). At 12 months of age, all animals were euthanized and the right femurs were embedded with the cortical shell of the mid-diaphysis exposed. The top surface of the bone blocks were polished (Buehler, Lake Bluff, IL) with 1,200 grit carbide paper and a cloth impregnated with diamond suspensions (particle size 3, 1, 0.25, 0.05 μm) for 3 min at each step. All procedures were approved by the Stony Brook Institutional Animal Care and Use Committee.

FTIR Microspectroscopy

FTIRI was performed using a Hyperion 3000 FTIR microscope (Bruker Optics) equipped with a 64 x 64 element FPA detector. Polished bone blocks samples were mounted such that the surface was parallel to the focal plane produced by the optics. A 15X objective (0.4 numerical aperture) was used for data collection and 4 x 4 binning was applied to yield a 11 μm pixel resolution. Data were collected with a wavelength range from 850 to 3900 cm^{-1}, a spectral resolution of 8 cm^{-1} and 32 scans were co-added. A gold coated microscope slide was used as a reference material with 512 co-added scans. For all samples, the entire cortical shell of approximately 3 x 3 mm was imaged, which typically consisted of 450 FPA tiles, or 115,000 spectra. Reflection data were used to calculate absorbance equivalent spectra as described in [137]. Individual spectra were integrated to yield the degree of tissue mineralization (phosphate/protein ratio), carbonate substitution into the mineral lattice (carbonate/phosphate ratio), mineral crystallinity (ratio of stoichiometric / non-stoichiometric phosphate), and collagen cross-linking (Table 2-1).

Automated Region-of-Interest Selection

To ensure an unbiased analysis of regions within the IR integration maps of the cortical shell, a MATLAB procedure was developed that automatically recognizes the shape and orientation of the cortical shell, identifies the quadrants (posterior, lateral, anterior and medial) and overlays 3 rectangles in each quadrant (Figure 3-1). First, a low and high cutoff threshold is applied to the IR integration map for mineralization. The resulting bitmap is further filtered to yield an image of the bone, where back pixels correspond to the presence of bone. An outline of the bone's circumference and the weighted center are then used to plot the distance between the center and the circumference, as a function of angle. From this plot, the location (angle) or negative and positive peaks are correlated to the posterior, lateral, anterior and medial directions of the cortical shell. Based on this information, the IR integration map is rotated to have the lateral quadrant on the top. Afterwards, rectangles of a specific size (in this case 100 x 500 μm), are drawn in the quadrants directly on the horizontal and vertical axis. The orientation of these rectangles follows the angle of the nearest surface, e.g. the periosteal rectangles are angled to match the periosteal surface. More details are provided in Appendix C.

Data Analysis and Regions-of-Interest

A Matlab routine was developed to generate a mask representing the shape of each femur by identifying bone and non-bone pixels based on thresholding of mineralization IR maps. The masks were then rotated and flipped such that the lateral, anterior, medial and periosteal surfaces pointed up, right, down and left, respectively. The routine placed 100 x 500 μm rectangles in the each quadrant of each mask; a first set 50 μm from the periosteum, a second set 50 μm from the endosteum and a third set in between the periosteal and endosteal ROI. The periosteal and

endosteal ROI were orientated parallel to their respective surface, while the orientation of the intracortical ROI was an average of the periosteal and endosteal ROIs in each quadrant (Figure 3-2C). The mask and associated ROI of each specimen were then matrix multiplied with all of the specimen's integration maps, resulting in an average value and standard deviation per ROI per integration map for each specimen. Each ROI contained 500 spectra.

Statistical Analysis

ROI within treatment groups were compared using a one-way ANOVA followed with a Tukey Post-Hoc test. Comparisons between treatment and OVX per ROI were performed using an ANOVA followed with a Dunnett test (SPSS).

4.4 Results

Regional Differences within Specimens

In the alendronate treated specimens, a highly mineralized circumferential lamellar region on periosteal bone was clearly distinguishable from lower mineralized intracortical bone. For all three treatment doses, the periosteal circumferential lamellar ROI had a significantly higher ($p<0.05$) level of tissue mineralization compared to intracortical bone (Figure 4-1). Further, carbonate substitution levels in periosteal circumferential lamellar bone was higher than intracortical bone in the medium dose alendronate treatment (Figure 4-2), but no differences were observed in mineral crystallinity or collagen cross-linking.

Similar to the alendronate treated specimens, also the parathyroid group showed a highly mineralized circumferential lamellar layer on the periosteum. For low and high PTH treatments, a significant differences was observed between the periosteal circumferential lamellar and

intracortical ROI ($p<0.05$), but not for the medium dose (Figure 4-1). No further differences were found in carbonate substitution, mineral crystallinity or collagen cross-linking.

Chemical Differences Compared to OVX

A comparison of whole bone chemistry between the alendronate treated specimens and OVX did not find significant differences. On an ROI basis, comparisons to OVX revealed higher mineralization levels in intracortical bone of M-ALN ($p<0.05$). Further, carbonate substitution levels in endosteal regions of L-ALN ($p<0.05$) and M-ALN ($p<0.01$), and in the intracortical ($p<0.05$) and periosteal ($p<0.05$) regions of M-ALN treated groups were higher than OVX.

Whole bone comparisons of the chemical parameters of the PTH treatment groups compared to OVX identified lower collagen crosslinking ($p<0.05$) and higher crystallinity levels ($p<0.01$) in the L-PTH group. No other differences in whole bone comparisons were observed. Comparing the chemistry on an ROI basis showed lower levels of tissue mineralization in periosteal circumferential lamellar bone of M-PTH ($p<0.05$). Crystallinity values in the L-PTH group were higher in all regions (endosteal, intracortical, periosteal, and periosteal/lateral) compared to OVX ($p<0.05$). Collagen crosslinking values in intracortical ($p<0.05$) and periosteal ($p<0.05$) bone of the M-PTH were higher. Further, carbonate substitution levels in endosteal regions of H-PTH ($p<0.01$) were higher than OVX.

4.5 Discussion

In this study, we examined the chemical composition of cortical bone from diseased and drug treated rats using FTIRI. We observed an uneven mineralization in the control (OVX) and all treatment groups, with highly mineralized circumferential lamellae on the periosteum, and lesser

mineralized intracortical bone, similar to the observation in fluoride treated animals. This phenomenon has not been reported elsewhere in IR spectroscopy literature, although it has been suggested that tissue mineralization of circumferential lamellae and osteons increase at a different [129] than other regions in cortical bone, and similar findings have been observed in untreated bone in cortical bone of 8-month old Sprague Dawley rats using Raman spectroscopy [84]. Another explanation of the high degrees of mineralization in the lateral-posterior region of the periosteum in both OVX, alendronate and parathyroid hormone treatment groups is the notion of cortical drift in the periosteal-lateral direction [143]. This is the natural development and preferential growth of circumferential lamellar bone in the periosteal-lateral region of the cortex.

Medium dose alendronate treatment saw an increase in intracortical mineralization, which could be explained by reduced bone turnover and continued secondary mineralization by alendronate [150]. Interestingly, low and high dose treatments did not see this effect. This could suggest that not enough bone suppression occurred at the low dose and thereby allowing normal progression of tissue mineralization, while the high dose suppressed turnover and also prevented secondary mineralization. This type of modulation in bone turnover is also evident by the increased levels of carbonate substitution into the mineral lattice in endosteal, intracortical and periosteal bone of medium dose treatment and in endosteal bone of low dose treatment. As bone ages, carbonate substitution increases, but high rates of bone turnover typically prevent the accumulation of carbonate substitution [101]. In the low alendronate dose, increased carbonate substitution levels were only found in the endosteum and not throughout the cortical shell, which suggest a minimal effect and explains why mineralization levels were not affected. On the contrary, high doses of alendronate caused a dramatic reduction in bone turnover and secondary

mineralization, thereby preventing significant chemical changes to the bone, as is evident in tissue mineralization and carbonate substitution levels.

Despite the strong anabolic effect of PTH, tissue mineralization was lower in circumferential lamellar bone at a medium PTH dose, consistent with earlier reports that found an increase in uniformity of tissue mineralization due to PTH treatment [56]. This was not observed at low doses, likely because the effect of PTH on tissue mineralization was too small, although here the mineral crystallinity across the cortical shell was improved, suggesting modest. The lower tissue mineralization was also not observed at high doses of PTH; here it is likely that the effect of PTH was strong enough to improve both bone formation and tissue mineralization [151]. The lower collagen cross-linking ratio across the cortical shell of low dose PTH treatment indicates a shift towards divalent cross-links found primarily in young bone, suggesting that low dose PTH did have a modest effect on the cortical bone. However, at medium dose, the collagen cross-linking ratio was increased in intracortical and periosteal bone, indicating collagen maturity [152].

4.6 Conclusion

High resolution FTIRI is a unique tool that provides the sensitivity and spatial resolution (~10 μm) to investigate the chemical properties of small regions of interest within the cortical shell, such as the anatomically distinct circumferential lamellar bone or user defined quadrants within the cortical shell. Our results indicate that differences in tissue mineralization between intracortical and circumferential lamellae of cortical bone are present in osteoporotic and bone treated with alendronate and parathyroid hormone alike. Although the effects of alendronate treatment were primarily on tissue mineralization and carbonate substitution levels in endosteal and intracortical bone, parathyroid hormone induced changes to both mineral crystallinity and

collagen cross-links, pointing out the different mechanisms of action by these treatments. These results provide a better understanding of alendronate and parathyroid hormone affect the chemical composition across the cortical shell, and could help understand how these drugs are most effectively used. Further research into the contributions these drugs on the nanoscale structural properties on the mechanical properties, on both the microscale and tissue level, will help understand the relationship between the chemistry, structure and mechanical properties of bone tissue.

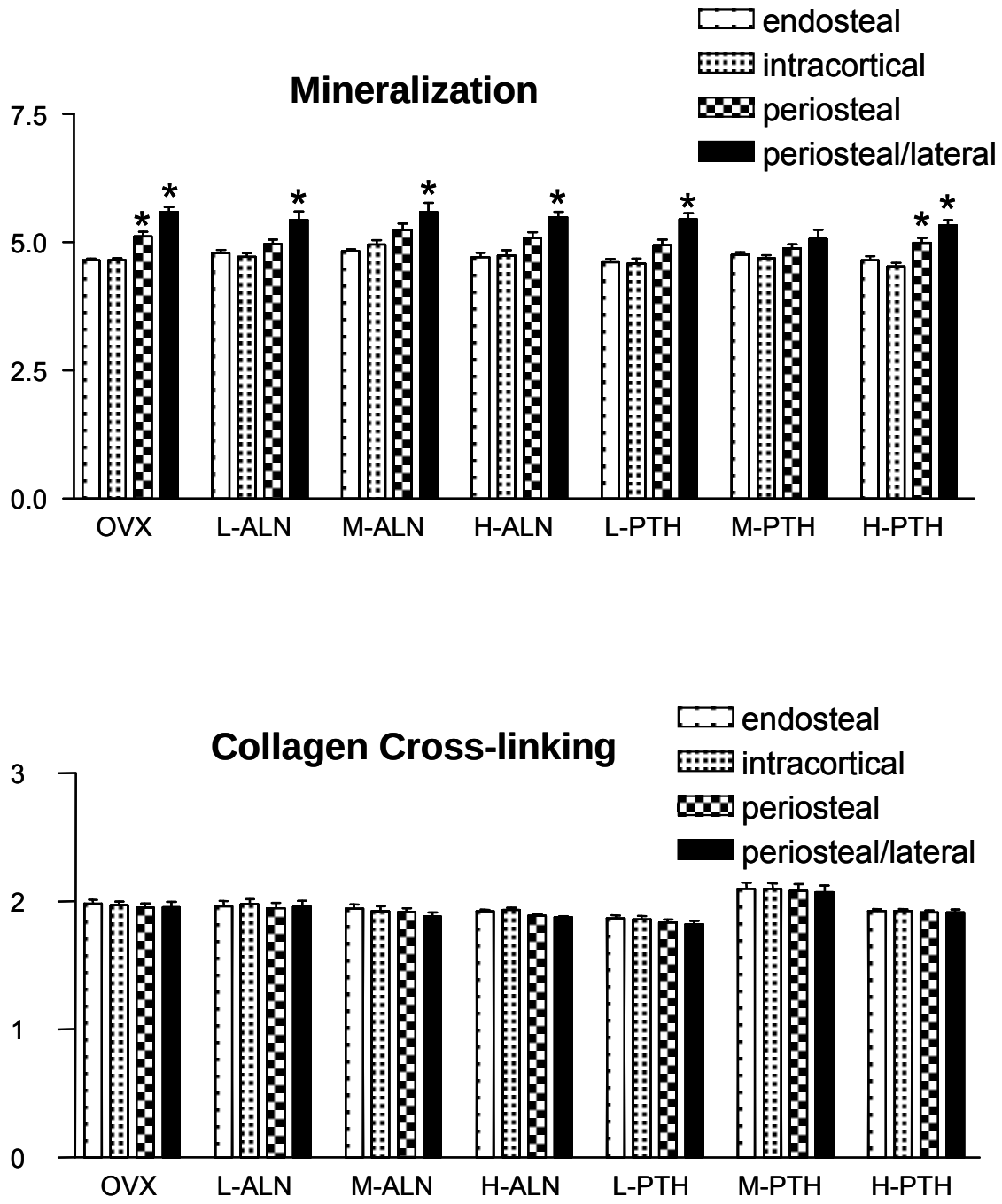

Figure 4-1: Tissue mineralization and collagen cross-linking in OVX, alendronate and parathyroid hormone treated groups per region of interest. * indicates significant difference from the intracortical ROI.

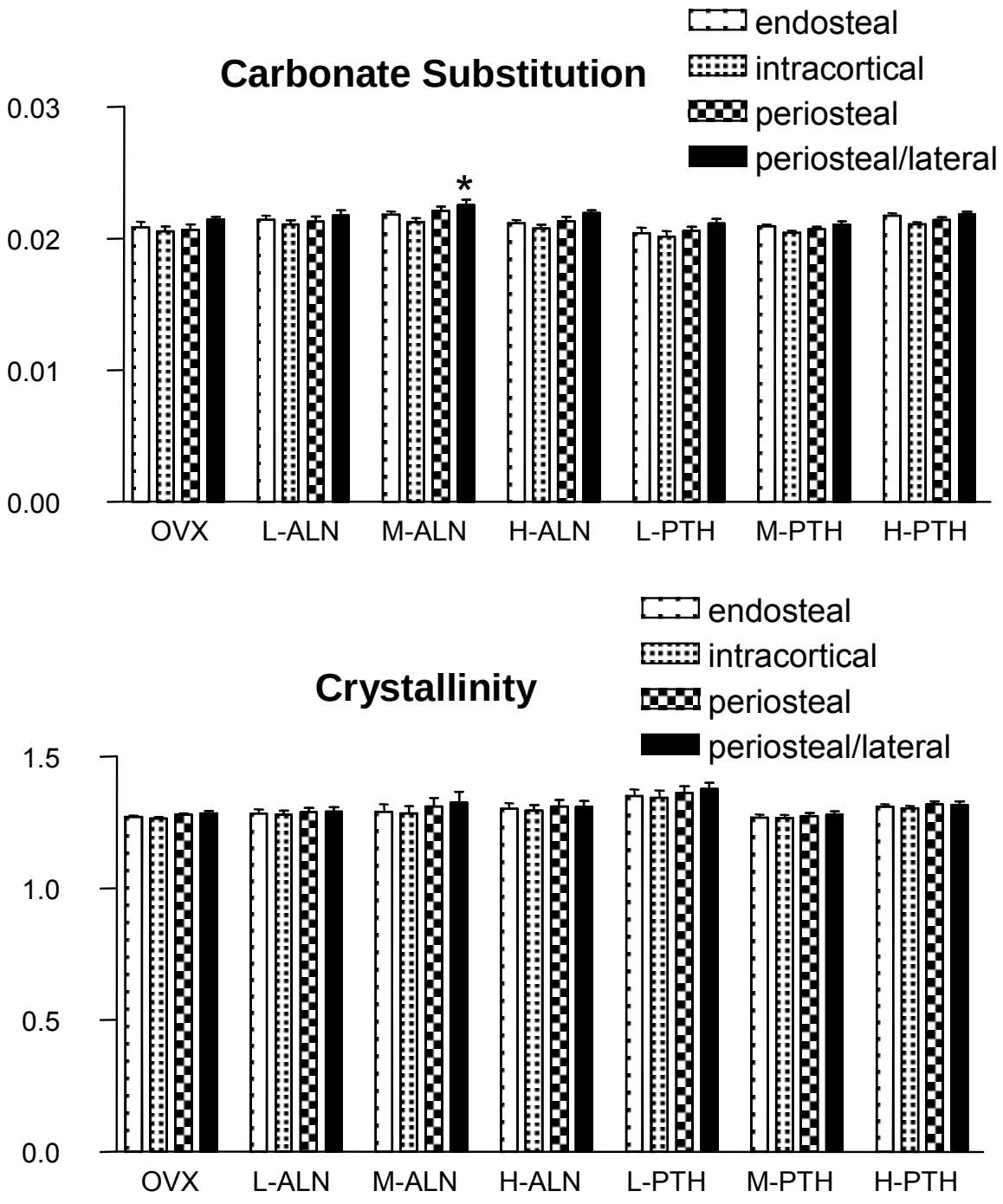

Figure 4-2: Carbonate substitution and mineral crystallinity in OVX, alendronate and parathyroid hormone treated groups per region of interest. * indicates significant difference from the intracortical ROI.

CHAPTER 5

ALTERATIONS TO CRYSTAL GEOMETRY AND ORIENTATION OF COLLAGEN FIBRILS IN EXISTING BONE DUE TO OSTEOPOROSIS ARE PREVENTED BY PHARMACEUTICAL DRUGS

5.1 Abstract

The influence of macroscale material properties of bone on its mechanical competence have been extensively investigated, but less is known about the contributions of the nanoscale material properties of bone. Recent research suggests that these nanoscale properties, the collagen network and the size and shape of hydroxyapatite mineral crystals, are modulated by aging of the tissue, mechanical strains and stresses and diseases such as osteoporosis, but little is known about the effects of pharmaceutical treatments and how this might affect the nano and macro mechanical properties of bone. Here, we used simultaneous Small and Wide Angle X-ray Scattering microbeam mapping to investigate changes in the collagen and mineral properties of cortical thin sections induced by osteoporosis and osteoporosis treatments at a high resolution. Our results show that osteoporosis reduced the mean deviation of the collagen orientation in existing intracortical bone, and that this was mitigated by treatment with Aln or NaF, but not by PTH. No changes were observed in the degree of collagen orientation at <20 micron resolution. Further, the mineral crystal width in newly formed periosteal bone was smaller in animals with osteoporosis, but existing cortical bone was not altered. These results indicate that the collagen and mineral properties in new and old bone are altered by the osteoporosis, and that these effects can be mitigated to some degree by osteoporosis treatments. In order to better define how these

parameters contribute to bone quality, further research is required to elucidate how subtle changes in the nanostructural properties affect bone's micro and macro mechanical properties.

5.2 Introduction

Bone undergoes a continual remodeling process mediated by the rate of bone formation and resorption. Aging, external mechanical strain [153], and pharmaceutical treatments have been shown to affect the various aspects of bone remodeling, but they also modulate the quantity and quality of new and old bone as measured by DXA, computed tomography (CT) and FTIRI. In turn, such changes alter mechanical properties and the ability to resist fracture. Although changes to the macro mechanical properties of bone are thought to be governed by changes to tissue quantity and quality, defining quality and by what mechanism the various parameters affect mechanical properties remains a challenge.

Small Angle X-ray Scattering (SAXS) has been used for decades to probe the structural arrangement of the collagen fibril networks and how these properties change as the tissue matures or is afflicted by diseases such as osteoporosis [56] or osteogenesis imperfecta [154]. Likewise, Wide Angle X-ray Scattering (WAXS) has been successfully used to interrogate the geometric properties of nm-sized mineral crystals embedded within this collagen network. Recent works have investigated if and how current osteoporotic treatments modulate these properties of bone [45, 56], and how they might affect the micro mechanical properties [155] and ultimately macro mechanical properties. The advent of third-generation synchrotron radiation sources has enabled these types of experiments to be performed using small spot sizes (<20 μm) at the sample location while maintaining a sufficiently high flux (>10^8 photons s^{-1}) in order to probe the organic and mineral properties of bone tissues at a high spatial resolution. These

developments have enabled more detailed investigations of the structure and orientation of mineral crystal in lamellar bone [156] and the bone/cartilage interface [157], but in different tissues [158]. The combination of simultaneous SAXS and WAXS data collection further allows for the pixel-to-pixel correlation of the collagen and mineral properties at a high spatial resolution.

The aim of this study is to gain insight into how the mineral and collagen properties of existing and new bone tissue might be modulated by osteoporosis and pharmaceutical treatments. We used synchrotron based simultaneous SAXS and WAXS to investigate the mineral crystal size and shape and the orientation and degree of orientation of the collagen network at a high spatial resolution in cortical bone.

5.3 Methods

Specimen Preparation

25 female Sprague Dawley rats were divided into groups (n = 5) labeled age-matched control, untreated ovariectomized (OVX), OVX treated with subcutaneous injections of parathyroid hormone 1-34 at a dose of 15 μg/kg/d (PTH), OVX treated with subcutaneous injections of Alendronate at a dose of 100 μg/kg/2x/wk (Aln) or OVX treated with 500 ppm sodium fluoride in drinking water (NaF). At 5 months of age, all groups except control were ovariectomized. Treatments started at 6 months of age, and continued for 6 months at which time all rats were sacrificed (12 months) and the right femurs were embedded in polymethyl methacrylate. 10 μm sections of the femur were cut at the metaphysis in the mid-sagittal plane. All procedures were approved by the Stony Brook Institutional Animal Care and Use Committee.

Simultaneous Synchrotron SAXS and WAXS

Simultaneous data collection of SAXS and WAXS patterns was performed at beamline X9 of the National Synchrotron Light Source at Brookhaven National Laboratory [159]. The x-ray ring operates at 2.8 GeV and provides a current between 200 and 300 mA. A Si(111) DCM monochromator (FMB-Oxford) was used to tune the x-ray energy to 0.918 Å. A primary focusing mirror system composed of SESO bimorph mirrors and a secondary K-B focusing mirror were used to focus the beam to a small spot, which was further apertured down to a 20 x 20 μm spot size at the sample location. A 1024 x 1024 pixel Mar 165 CCD detector was placed at a sample-to-detector distance of 3.135 meter to provide for SAXS data collection in the q-range of 0.005 to 1.5 $Å^{-1}$. A custom designed Photonic Science detector was placed at an off-angle to provide for WAXS data collection in the q-range from 1.5 to 4 $Å^{-1}$ (Figure 5-1). SAXS and WAXS patterns were q-calibrated using AgBH and LaB_4 standards, respectively. Specimens were oriented with the proximal-distal direction vertical, ensuring that the (002) reflection of the mineral crystals fell on the WAXS detector. Specimens were raster scanned across the cortical shell and approximately 150 μm in the proximal-distal direction with a step size of 20 μm. SAXS and WAXS patterns were simultaneously collected for 30 seconds at each point.

SAXS and WAXS Data Reduction

The beam center on SAXS patterns was determined by fitting a circle to the AgBH scattering patterns before and after each specimen. The 2-dimensional SAXS intensity patterns $I(q,\psi)$ were transformed with respect to the beam center into a 2-dimensional matrix of $I(\psi)$ plotted as a function of q. Integrating over a q-range from 0.3 to 0.5 $Å^{-1}$ produced SAXS orientation plots of I(q) as a function of ψ, and integrating over ψ produced SAXS intensity plots of I(q) vs q.

WAXS patterns were corrected for detector tilt, rotation, and roll, and subsequent beam center refinement was performed using a circle fit (Taubin method) on LaB_4 scattering patterns. The WAXS patterns were then radially integrated about the center to yield plots of I(q) vs q. An overview of the data reduction is shown in Figure 5-2.

Collagen D-spacing, Orientation, and Isotropy

For determining the collagen *D*-spacing, $q^2I(q)$ as a function of q was used to locate the third harmonic of collagen. The third harmonic peak was curve fit and the peak maximum determined as a function of q. The SAXS intensity I(q) as a function of ψ holds information about the orientation of the scattering pattern [160] (Figure 5-2). The angular location of two peak maxima, which are separated by 180°, directly indicate the projected orientation (PO) of the collagen and mineral crystals, rotated by 90°. The difference between the mean PO for the imaged area and the PO at each pixel was used as a measure of deviation of the PO. The degree of orientation (PDO) was calculated by the integrated area of the two peaks on a flat baseline, ratioed to the total integrated area. The resulting value of ρ thus indicates perfect alignment ($\rho \rightarrow 1$) or no alignment ($\rho \rightarrow 0$) [161]. A measure of tissue level collagen isotropy was calculated by the mean angular deviation of collagen at individual pixels from the mean collagen orientation.

Mineral Crystal Geometry

Crystal lengths in the c-axis and widths in the *ab*-plane were derived from the widths of the (002) and (310) reflections, respectively. For both reflections, first a linear baseline was fit as described in [162]. The peaks were then curve fit using an asymmetric pseudo-Voigt function with varying weights of Gaussian and Lorentzian components as well as varying asymmetry by

method of least squares algorithm. Total integrated area, FWHM and the location of peak maximum were calculated. Instrumental line broadening was removed by subtracting the instrument's squared FWHM from the squared FWHM of the specimens, and taking the square root of the result [155]. The corrected FWHM values for the (002) and (310) reflections were then used to calculate the crystal dimensions along the *c*-axis and the *ab*-plane, respectively, using Scherrer's equation [155]:

$$D = K \lambda / \beta_{1/2} \cos(\theta)$$

where D is the average crystallite size corresponding to the chosen reflection, K is a constant describing the crystal shape, λ is the X-ray wavelength, $\beta_{1/2}$ is the FWHM after correcting for line broadening and θ is the scattering angle. K was chosen to be 0.9.

Regions of Interest and Statistical Analysis

Bone and background pixels were identified based on total scattering intensity: areas in the specimen without bone material had little scattering, while areas with bone material produced a lot of scattering. Based on the growth rate of cortical bone in the metaphysis of the femur in Sprague Dawley rats, it was estimated that ~60 μm of new bone had been added on the periosteal surface. Regions of interest were drawn to include the outermost ~60 μm (3 pixels) of bone on the endosteum (newly formed bone since start of treatment) and periosteum (periosteal ROI), and a third region of interest on the remaining bone (intracortical ROI). Within each ROI, means and standard deviations for the predominant collagen orientation, the degree of collagen orientation, collagen *D*-spacing, crystal length, crystal width and crystal deformation were calculated.

Nonparametric statistics were used due to the small sample size. To reduce the number of comparisons, no comparisons between treatments groups were performed. The mean deviations

of the PO from the mean PO for each treatment were compared to control and OVX per ROI, using a nonparametric one-way ANOVA with the Dunnett post-hoc test (GraphPad Prism 3.0) with a significance level of 0.05. Unpaired t-tests were performed between intracortical and periosteal, and intracortical and endosteal parameters.

5.4 Results

An overview image of a representative age-matched control specimen labeled with the periosteum (denoted *Per*), intracortical bone and endosteum (denoted *End*) of the cortical shell as well as the trabecular bone is shown in Figure 5-3A. The imaged area (200 x 460 μm) shows a smooth periosteum and an irregular endosteum. The collagen *D*-spacing showed less heterogeneity across the cortical shell (Figure 5-3B), with several areas showing an unresolved collagen *D*-spacing. The projected degree of orientation (PDO) and predominant orientation (PO) of the collagen are depicted by oriented lines indicating the orientation (0-180°), and the line lengths reflect the degree of orientation (0→1). The collagen orientation in the periosteal bone appeared parallel to the periosteal surface with a homogeneous PDO (Figure 5-3C). Intracortical bone shows clusters of low and high PDO, while the PO was less aligned with the periosteal or endosteal surfaces, similar to as reported by [45]. The mineral platelet length (*c*-axis) and width (*ab*-plane) are shown in Figure 5-3D-E, and indicate a slightly shorter, but similarly wide crystal in the newly formed bone on the periosteum. The aspect ratio of the crystals, a measure of crystal deformation and defined as the ratio of length to width, are shown in Figure 5-3F.

SAXS - Collagen D-spacing, Orientation, and Isotropy

For all samples, the mean collagen fibril PO in newly formed periosteal and existing intracortical bone was parallel with the mean orientation of the endosteal and periosteal surfaces. When comparing the mean collagen fibril PO in intracortical bone Figure 5-4A, OVX specimens were found to have a lower mean deviation from the mean orientation compared to control specimens ($p<0.05$). Compared to OVX, Aln ($p<0.05$) and NaF ($p<0.05$) were found to have a higher mean deviation from the mean orientation, while PTH did not differ from OVX. The PDO and collagen *D*-spacing did not vary when comparing the intracortical and periosteal regions within groups Figure 5-4B. Further, in regional comparison between control and OVX, and between OVX and treatment groups, no significant differences were found Figure 5-4C.

WAXS - Mineral Crystal Length, Width and Deformation

Several crystallographic reflections were identified based on a hydroxyapatite standard in the azimuthally averaged WAXS patterns, and these were found to be present in all specimens. Although many of the reflections are well resolved, the (002) and (310) reflection were chosen for analysis as they do not overlap with other reflections. Furthermore, they provide complementary information about the crystal dimensions, namely length along the *c*-axis and crystal width in the *ab*-plane, respectively. These reflections typically have a clean baseline on both sides which facilitates curve fitting [162]. The reflections have previously been found to be best described using an asymmetric pseudo-Voigt function with a linear baseline. Slight line broadening of the reflections due to instrumental broadening was observed, and subsequently the FWHM were deconvolved to remove this instrumental line broadening [155]. An intense but complex peak is present at 2.80 Å, but the complexity of deconvolving and curve fitting the

overlapping (211), (112), (300) and (202) peaks requires excellent signal quality, which is typically reserved for powder diffraction experiments.

Average crystal lengths along the *c*-axis, widths in the *ab*-plane and crystal deformation are reported in Figure 5-5. In control specimens, mean crystal lengths were 31.5 ± 2.6 nm and 29.6 ± 1.8 nm for intracortical and periosteal bone respectively, while crystal widths were 11.6 ± 1.2 nm and 11.7 ± 0.8 nm, respectively. No changes were seen in crystal deformation. In the OVX group, crystals in intracortical bone had a mean length of 30.4 ± 3.0 nm, while the periosteal crystals were significantly shorter at 26.5 ± 2.0 nm in length ($p<0.05$). No further significant differences were observed in crystal widths and deformation between intracortical and periosteal bone. In the treatment groups, no significant differences were found between intracortical and periosteal bone.

Compared to crystals in the periosteal region of control specimens, the crystal length in periosteal bone of OVX specimens were significantly shorter ($p<0.05$) and the periosteal crystal deformation ratio less ($p<0.05$). The mean crystal width (*ab*-plane) of crystals in intracortical bone of OVX specimens was 11.6 ± 1.2 nm, an increase of 12% from control specimens (13.0 ± 0.8 nm), although this was not significant, and no differences were found in crystal geometry in intracortical bone.

The alendronate treatment group was found to contain longer crystals (32.6 ± 3.1 nm) in periosteal bone compared to periosteal bone of OVX specimens ($p<0.05$), and consequently the crystal deformation ratio was higher ($p<0.05$). Additionally, intracortical bone of alendronate specimens was found to have narrower crystal compared to the same region in OVX ($p<0.05$). Treatment with PTH reduced intracortical crystal width relative to the same region in OVX

($p<0.05$), but no further differences were found due to PTH in any region. NaF did not significantly alter crystal length, width or deformation compared to OVX for any region.

5.5 Discussion

In the present study, simultaneous mapping of the structural organic and mineral components in cortical bone specimens using a combined SAXS and WAXS data collection setup is reported. We employed dedicated SAXS and WAXS detectors which provided a continuous q-range from 0.005 to 4.0 $Å^{-1}$ with high q resolution, sufficient to resolve small variations in both the collagen and mineral components of bone tissue. SAXS has previously been used to characterize mineral and collagen orientation [45, 163] and the degree of orientation [164], as well as the collagen *D*-spacing, which is typically 64 - 67 nm in bone tissue [165] and mineral crystal thickness [160]. WAXS provides more detailed information about the geometry of the mineral crystals, and is typically used to determine crystal lengths along the *c*-axis as well as the crystal width in the *ab*-plane [166]. We used simultaneous data collection of SAXS and WAXS patterns to ensure that information about the collagen and mineral phases could be directly correlated in a pixel-to-pixel fashion at the tissue level. The use of a synchrotron source further facilitated the experiment by providing high brightness at a small, focused spot size, which was needed to maintain a high signal-to-noise ratio to properly resolve weak features in the SAXS and WAXS patterns. Results showed that ovariectomy increased crystal widths in existing bone and increased the degree of collagen fibril alignment. While the bisphosphonate alendronate was found to mitigate alterations to the collagen alignment and mineral crystal due to OVX, PTH was only able to maintain crystal geometry. Fluoride treatment notably reduced collagen fibril isotropy, but had little impact on mineral geometry.

In rats, the normal maturation of mineral crystals found in the gap-zones of collagen fibrils is thought to occur in all directions, e.g. in the length, width [167, 168], and in thickness [66] following a logarithmic growth rate, producing mineral platelets with ultimate dimensions of 3 x 12 x 33 nm [169]. Different constraints limit the size in each dimension, and stress and strain may play a role as well. For example, the thickness of crystals is limited by the ~3.5 nm space between hole zones of collagen fibrils [170]. However, the type of bone [157], level of mineralization [163], or proximity to the growth plate [164] may vary the crystal thickness from 1.5 to 9 nm. Similar trends may be true for the crystal length and width [155]. While the length of crystal reaches maturity 8 and 14 weeks after nucleation in rat models, the growth in the width may continue to 22 weeks or beyond. Previous studies suggest that OVX increases mineral thickness beyond normal values in both existing and new bone [45, 56], possibly due to the continued maturation of bone and thus an overall increase in bone maturation compared to normal conditions. Our findings further indicate that OVX also increases the crystal width in existing bone, suggesting that OVX affects bone maturation of existing bone and old bone alike.

The efficacy of the bisphosphonate, alendronate, to reduce bone loss is achieved by inhibiting cell activity and thus bone turnover [171]. On the other hand, the anabolic effect of PTH increases bone mass and strength by the activation of bone lining cells and reduction of apoptosis of osteoblasts [172]. Both treatments have noted affects not only on new bone formation, but also on existing bone, with possible implications on the mechanical properties of these types of bone. For example, PTH has been found to increase intracortical bone turnover and porosity without affecting bone strength [173], while the reduced turnover induced by alendronate has been found to stem the increases in occurrence of osteocyte lacuna-size pores in existing intracortical bone in rats compared to OVX [22]. In previous SAXS studies using human

transiliac biopsies [66] and minipigs [160], ALN treatment did not offer protection to alterations of the crystal shape and thickness by OVX. Similarly, PTH treatment of mature rats did not significantly affect mineral thickness compared to OVX [56, 61], although both studies report a non-significant reduction in crystal thickness compared to OVX. Our results show that treatment with either ALN or PTH mitigated the effects on increased crystal width seen in OVX, suggesting that ALN and PTH treatments predominantly affect the crystal width. But the mechanisms by which these drug treatments achieve this are very different. In the case of ALN, presumably the reduced bone turnover slowed the process of mineral maturation to normal levels, while the observations in PTH treated rats may indicate a slight increase in catabolic activity in intracortical bone. Although the apparent ability of ALN and PTH to maintain normal crystal widths despite OVX is interesting, the accelerated rate of intracortical remodeling by PTH and reduced rate by ALN has serious implications for stress fracture repair [150, 174].

Although F delays mineral deposition, the increase to bone formation and mineral density occurs mostly in new bone during fluoride exposure, while minimally affecting previously mineralized, mature bone [70]. Newly formed bone during the treatment is typically of higher mineralization and crystallinity [166, 175], but less is known about how F affects the crystal size and shape. While our results support previous studies that the crystal length is not affected by F [175], crystal thickness is thought to increase due to F treatment [67, 160]. However, these changes are small enough that they alone are unlikely to cause significant disruption to the mechanical integrity of new bone. In addition to these small changes to crystals within fibrils, the formation of large crystals outside the collagen fibrils is thought to occur [176], which may explain why new bone is typically of higher mineralization and crystallinity, and less resistant to

fracture. Further, prolonged treatment with high doses of F can lead to hypermineralization of old bone, extending the deleterious effects deeper into existing bone.

Our results show that the orientation of collagen in periosteal bone is aligned parallel to the periosteum, consistent with earlier reports that collagen in endosteal bone and deposited by appositional growth in the periosteum is aligned with their respective surfaces [45]. We also found collagen in intracortical bone to be parallel with the endosteal and periosteal surfaces, with no significant variations due to treatment. The work by Bunger, et al showed that intracortical bone contains small clusters of collagen with similar alignment. Although we did not observe a difference in the degree of alignment across the cortical shell, it should be noted that Bunger, et al used cross sections compared to sagittal cut sections in our study. Thus, it remains possible that clusters of well aligned collagen fibrils extend in the proximal-distal direction, parallel to the direction of growth, but are less likely to be observed in the thin sections in proximal-distal direction. Our results further indicate that the deviation from the mean collagen orientation is severely reduced by estrogen withdrawal. The effects of estrogen withdrawal thus penetrate into intracortical bone, and either actively rearranges or prevents normal rearrangement of the collagen network to be more isotropic in the proximal-distal direction. Although total collagen content is thought to be un-affected by osteoporosis, mounting evidence indicates a significant reduction of enzymatic cross-links and an increase in AGE's cross-links, thereby directly affecting the material and mechanical properties of the tissue [39]. The collagen network was not affected in Aln or NaF treated bone, which were similar to control specimens, which may be due to the reduced cellular activity in the case of Aln, and the over-mineralization of the collagen network by NaF treatment. Interestingly, treatment with PTH had no effect indicating that its

anabolic activity offers little protection to the effects of estrogen withdrawal on the collagen network.

The simultaneous collection of SAXS and WAXS patterns by separate detectors allows for the direct correlation of the organic and mineral properties of bone at a high spatial resolution. However, a limitation of this setup is that only a partial WAXS pattern can be collected, since the WAXS detector has to be positioned off-axis with respect beam direction. Analysis of crystallographic reflections which are not continuous with respect to θ, such as the (002) reflection, may not produce reliable results if the reflection is not sufficiently captured by the off-axis WAXS detector. This makes analysis of the mineral phase in trabecular samples difficult, as the random alignment of mineral crystals in trabecular bone produces (002) reflections at unpredictable θ values. Further, the sample thickness should be chosen to match the collagen heterogeneity in the direction of the cut. This is especially important if the analysis of collagen orientation and degree of orientation is of interest.

5.6 Conclusion

In summary, successfully developed and employed simultaneous Small and Wide X-ray Scattering microbeam mapping to investigate the collagen fibril organization and mineral crystal geometry in health, diseased and drug treated bone tissue sections. Our results indicate that several of these properties are affected by disease and drug treatment, notably that collagen fibril isotropy was increased in diseased specimens, while this effect was mitigated in alendronate and parathyroid hormone treated specimens. Further, several changes to the mineral crystal geometry were noted, such as the reduced width of crystals in periosteal bone of diseased specimens, and the mitigation of this effect by the drug treatments. These results provide a better understanding

of how pharmaceutical drugs alter the structural properties of bone at the nanoscale, and can potentially contribute to bone quality. We anticipate that simultaneous Small and Wide X-ray Scattering microbeam mapping will become an important tool to investigate the collagen and mineral components of bone. Further research examining the contributions of the nanoscale structural properties on the mechanical properties, on both the microscale and tissue level, will shed light onto how disease and pharmaceutical treatments change the fragility of bone.

5.7 Supplemental Information

Detector Tilt Correction

Correcting the WAXS pattern based on the tilt of the WAXS detector is critical to achieving an accurate q-spacing. This correction can be performed by a series of matrix multiplications, which mimic the known tilt, but also the rotation of the WAXS detector. However, the order of the matrix multiplications should be carefully considered. Furthermore, since matrix multiplications are performed with respect to a center of rotation, this center should be defined as the out-of-sight beam center. In a series of steps, the WAXS pattern is first translated with respect to the beam center. A translation matrix can be constructed with offsets for the beam center over the x-and y-axes as follows:

$$\text{translate} = \begin{pmatrix} 1 & 0 & cx \\ 0 & 1 & cy \\ 0 & 0 & 1 \end{pmatrix}$$

Further, rotation matrices around the z-axis to correct for detector orientation θ and around the y-axis to correct for detector tilt τ are constructed as follows:

$$\text{rotateZ} = \begin{pmatrix} \cos(\theta) & -\sin(\theta) & 0 \\ \sin(\theta) & \cos(\theta) & 0 \\ 0 & 0 & 1 \end{pmatrix}$$

$$\text{rotateY} = \begin{pmatrix} \cos(\tau) & 0 & \sin(\tau) \\ 0 & 1 & 0 \\ -\sin(\tau) & 0 & \cos(\tau) \end{pmatrix}$$

An overall multiplication matrix based on the translation and rotation matrices is constructed to as follows, and takes into account the correct order of multiplication while conserving the rotation of the WAXS pattern:

$$\text{multMatrix} = \text{rotateZ}^{-1} * \text{ rotateY} * \text{rotateZ} * \text{translate}$$

Individual WAXS patterns are multiplied by multMatrix, after which the pattern is free from distortion due to the tilt of the WAXS detector.

WAXS Peak Fitting

In order to accurately determine the domain size of corresponding WAXS reflection, an accurate measurement of the FWHM and q-position of the reflection is needed. As such, an automated peak fitting procedure of the (002) and (310) WAXS reflections was developed in MATLAB. The procedure first takes into account the baseline of the peak surroundings by fitting a 2^{nd} degree polynomial to data point on both sides of the peak, but not the peak itself. This baseline is subtracted from the peak itself, leaving a baseline corrected peak.

A pseudo-Voigt distribution is a convolution of the Gaussian and Lorentzian distributions and is largely considered a best fit distribution for WAXS reflections of mineral crystals in bone. The peak fitting algorithm fits an asymmetric pseudo-Voigt function, which accounts for slight

asymmetry in the peak. An initial estimate of the peak volume is made by a simple integration, and the peak location is estimated by a peak search. An iterative peak fitting algorithm then fits the asymmetric pseudo-Voigt function while varying the location, total volume, asymmetry and contributions from Gaussian and Lorentzian shapes (Figure 5-6). Once fit, the FWHM and location are used in calculations of the domain size. To account for line broadening, the FWHM of (002) and (310) reflections are deconvolved using an estimate of line broadening based on a highly crystalline sample.

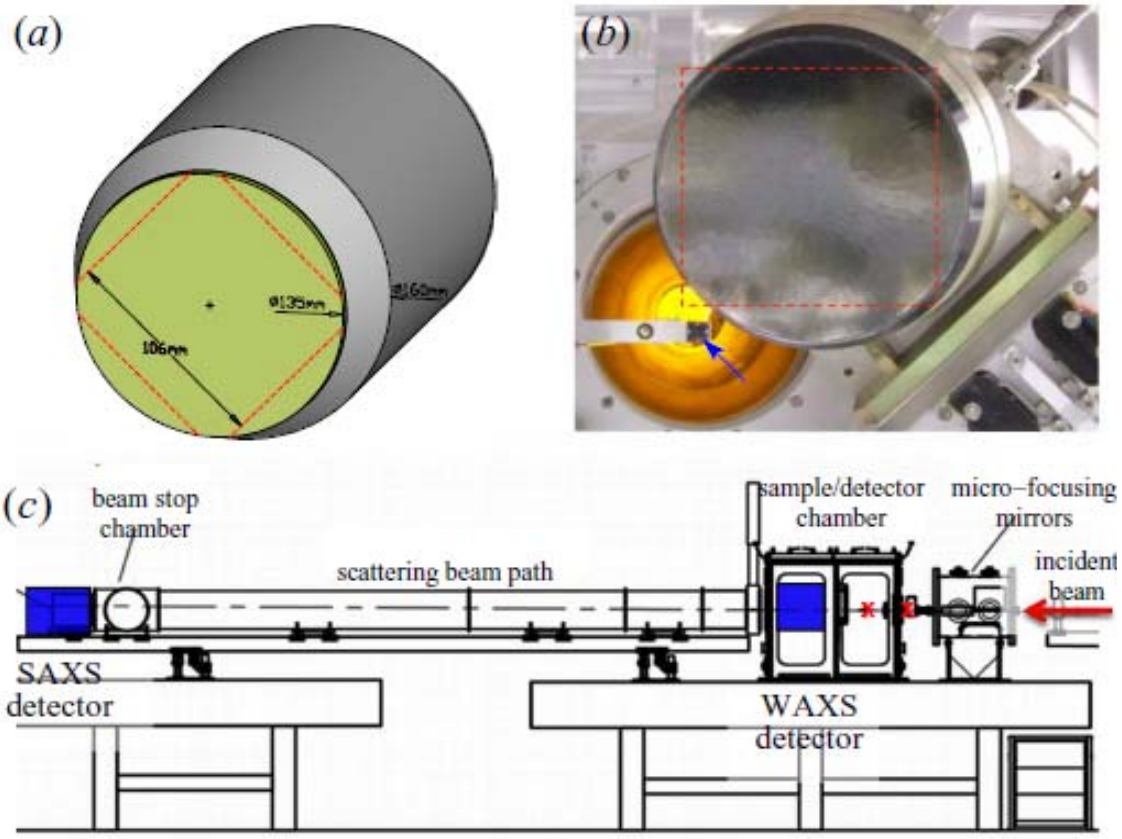

Figure 5-1: Configuration at beamline X9 of the National Synchrotron Light Source, Brookhaven National Laboratory. A) The WAXS detector is placed at an angle with respect to the incident beam. B) The SAXS detector is centered on the incident beam, and is partially obscured by the WAXS detector. This configuration provides a continuous q-range from 0.005 to 4. C) Side view end station at X9 showing the micro-focusing mirrors upstream of the sample chamber, and the WAXS and SAXS detectors downstream of the sample chamber [159].

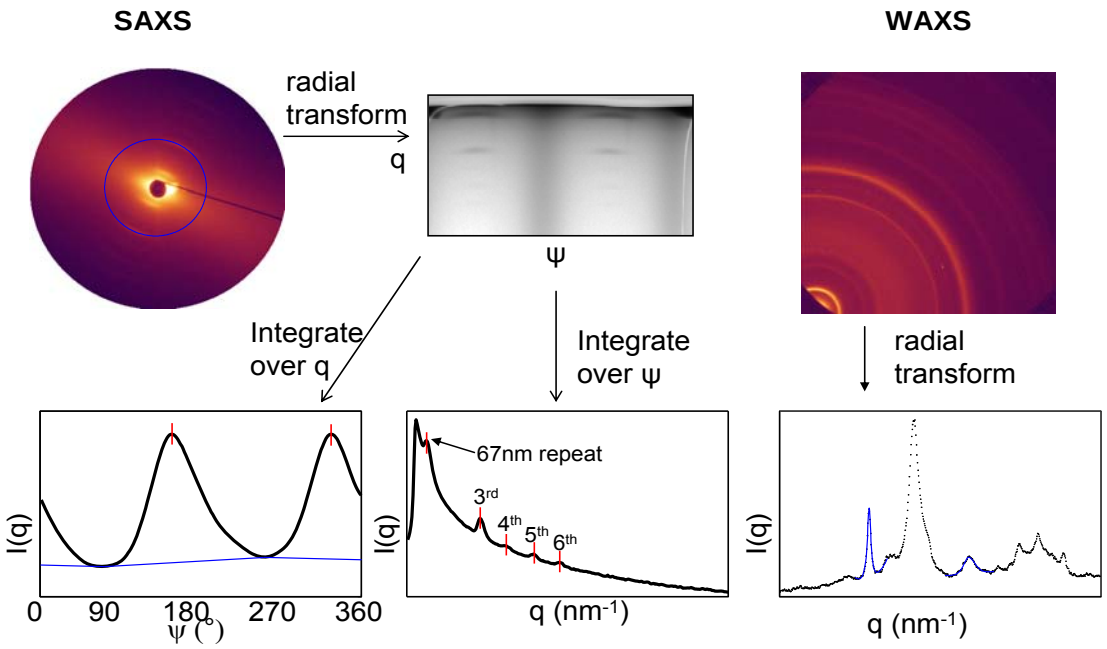

Figure 5-2: Overview of SAXS and WAXS data processing. On the left, a SAXS pattern is radially integrated around the beam center resulting in a plot of I(ψ,q). Integration over q yields an angular dependant intensity plot from which orientation is determined. Integration over ψ yields a plot of intensity versus q from which the collagen D-spacing is calculated. On the right, a WAXS pattern is radially integrated with respect to the out-of-sight beam center, resulting in a plot of I versus q in the WAXS range. Mineral crystal reflections (002) and (310) are outlined in blue.

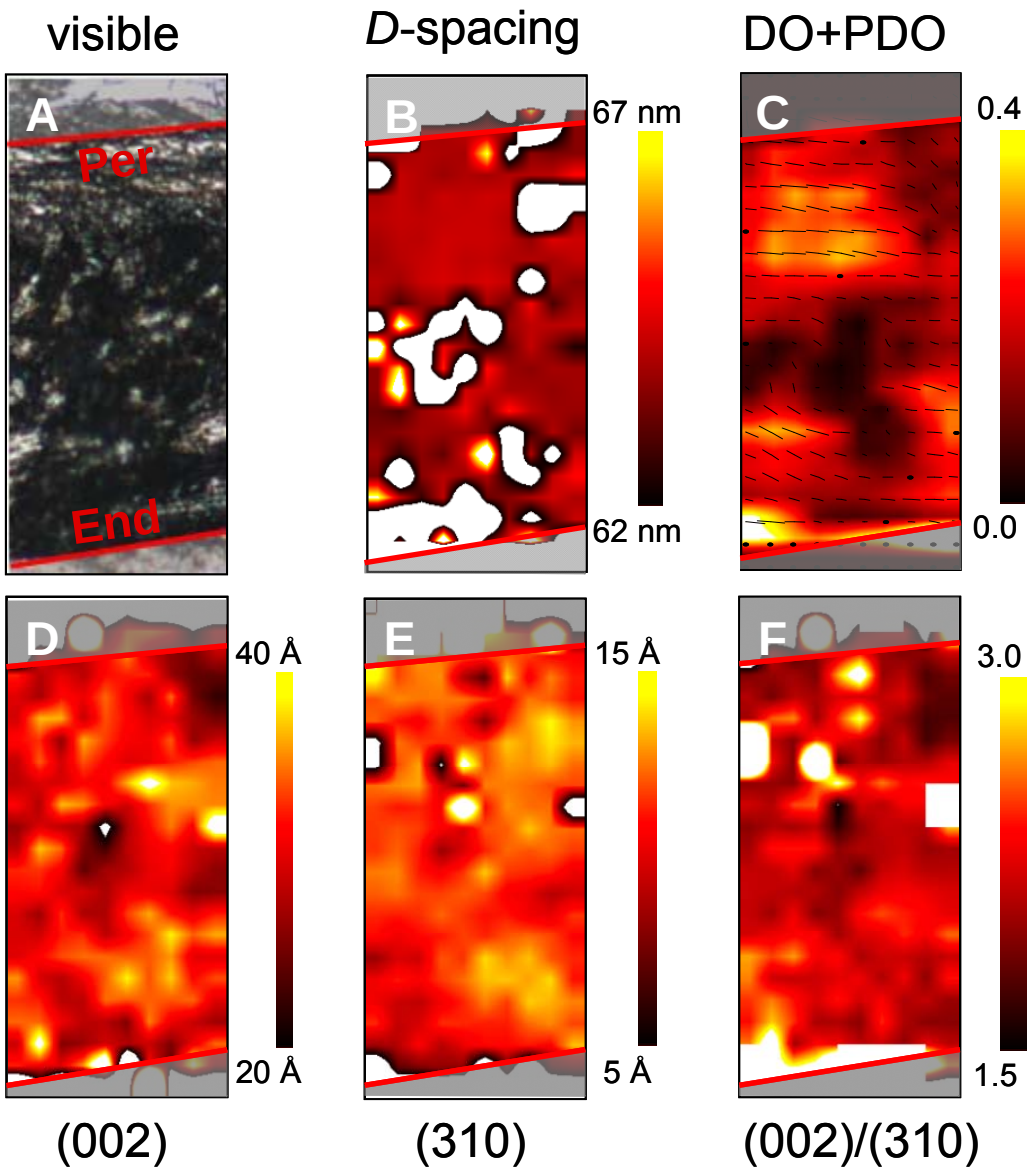

Figure 5-3: A) Visible light image of a portion of the cortical shell of a CTRL specimen. Endosteal (End) and periosteal (Per) surfaces are labeled. B) The collagen *D*-spacing as calculated from the 3rd harmonic in SAXS I(q) plots. C) The degree of orientation (line length and color) and predominant orientation of the collagen (line orientation). Black dots indicate no or unresolved alignment. D) The crystal lengths as calculated from the width of the (002) WAXS reflection. E) The crystal width as calculated from the width of the (310) WAXS reflection. F) A crystal deformation parameter, given by the ratio of the crystal length to width, (002)/(310).

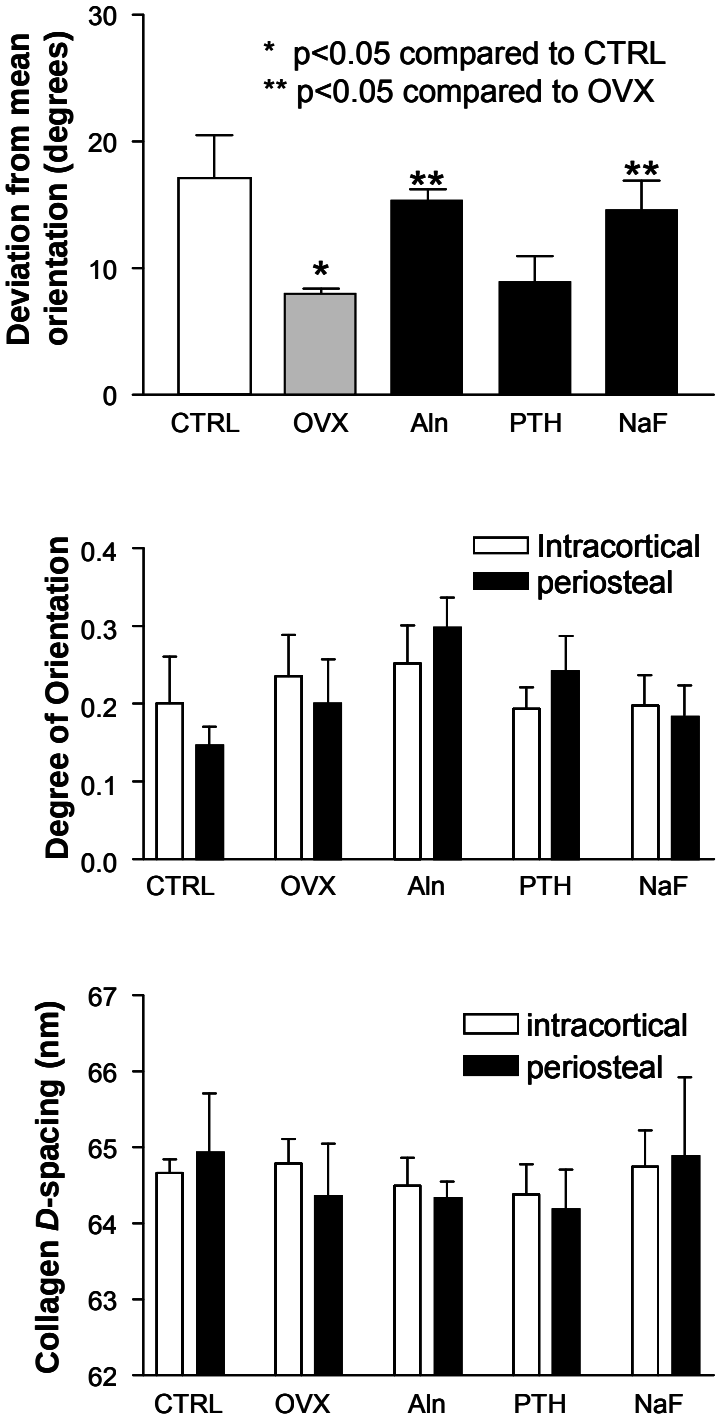

Figure 5-4: Top) The deviation from mean orientation is a measure of tissue level degree of collagen orientation (isotropy). A mean collagen orientation for all reported collagen orientations with a specimen is computed, and the deviation from this mean is reported as average and standard deviation. Middle) The degree of collagen orientation measured on a pixel resolution. Bottom) Collagen *D*-spacing calculated based on the distance (in q) of the 3rd harmonic in SAXS patterns.

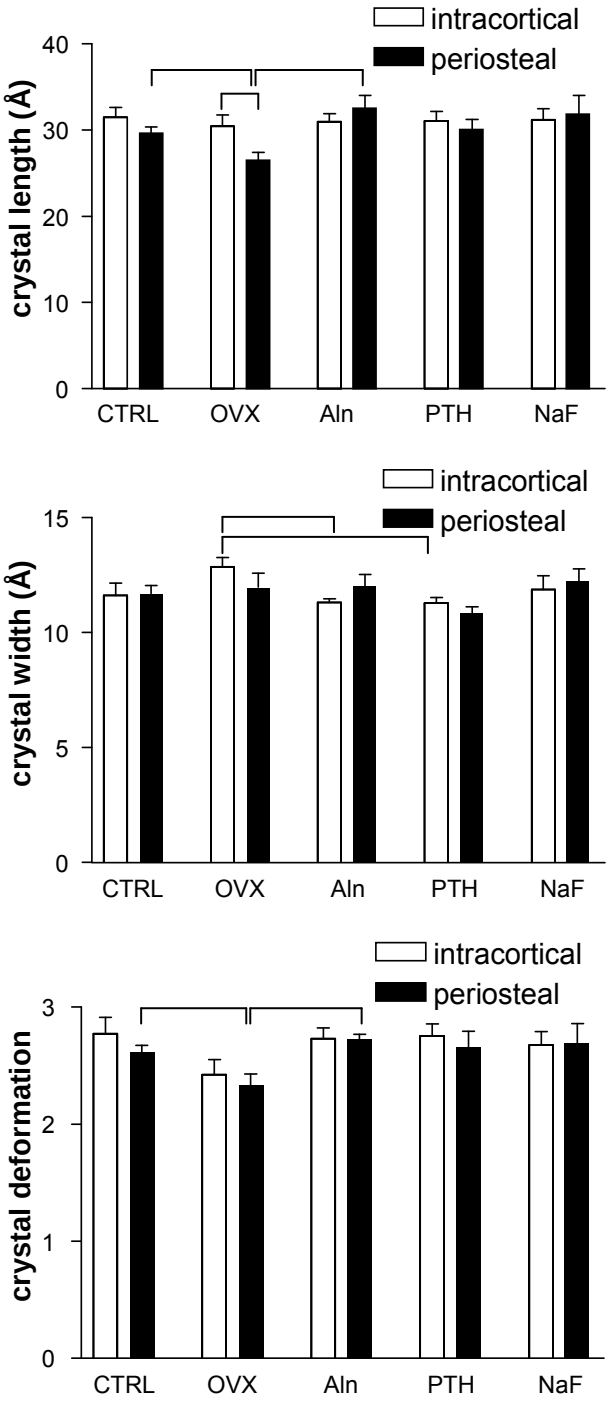

Figure 5-5: Top) Mineral crystal length as determined from the (002) reflection width. The mean crystal length in intracortical bone was ~31 Å in OVX specimens, and did not significantly change with treatments. Middle) Mean crystal widths as determined from the (310) reflection width. In OVX specimens, the mean crystal width was ~12 Å for intracortical bone. Bottom) A measure of crystal deformation, the crystal deformation parameter is defined as the aspect ratio of crystal length to crystal width. Significance between groups/regions is indicated by bar ($p<0.05$).

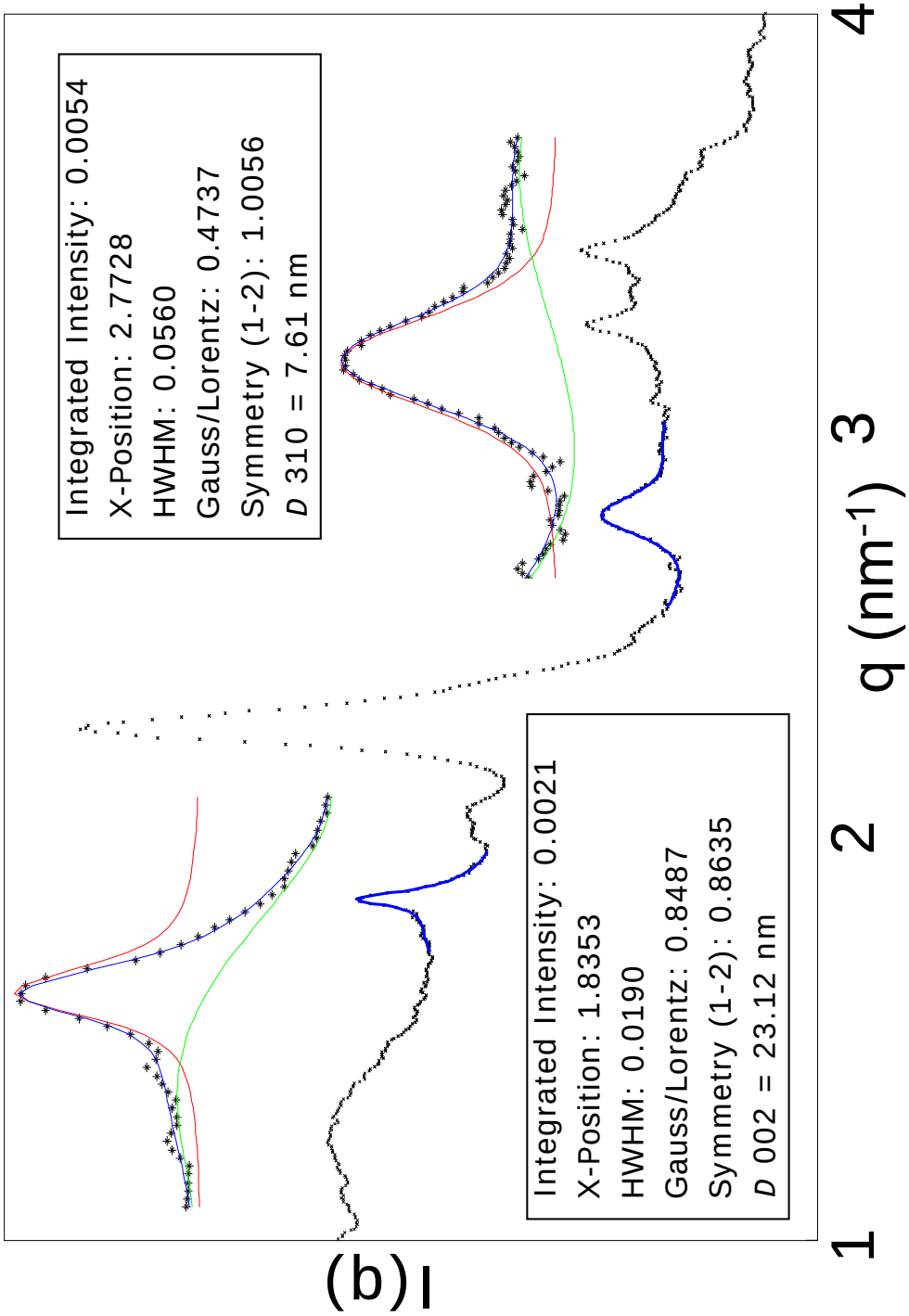

Figure 5-6: Representative WAXS pattern of cortical bone showing the peak fitted (002) and (310) reflections. Peaks were baseline fit with a polynomial and curve fit with an asymmetric pseudo-Voigt function. FWHM were used to calculate domain size using Scherer's equation.

CHAPTER 6

DISCUSSION AND CONCLUDING REMARKS

Bone diseases such as osteoporosis and osteogenesis imperfecta affect millions of Americans and are responsible for more than 2 million fragility related fractures annually [2, 3]. These diseases disrupt the roles of bone in a variety of ways, namely by impairing the chemical, structural and mechanical properties of bone. Although pharmaceutical drugs can mitigate some of these disruptions, they are not perfect, partially because it is largely unknown how these drugs affect the complex hierarchical structure of bone. This study clarifies some of the unknowns about bone chemistry and structure at the micro level, and how these properties might be affected by bone disease and pharmaceutical drugs that are designed to modulate these properties.

The current "gold standard" for the clinical assessments of bone fracture risk is based on measurements of bone quantity by DXA [8]. However, bone quantity alone is not a sole predictor of fracture risk. For example, both young, developing bone and older, osteoporotic bone may have similar bone quantity, but not the same fragility. Thus, there is a need to better define bone fracture risk as a function of both bone quantity and quality [9, 10]. Indeed, increasing evidence suggests that the contributions of various bone quality related parameters are as critical in estimating bone fracture risk. Although defining these parameters has been a topic for discussion for the past three decades, generally they fall into three categories: mechanical, structural and mechanical. Methodologies have been developed to assess the various properties of bone in these categories [9, 71, 74, 76] in order to understand how these properties contribute to bone quality and predict fracture risk. However, while most of these methodologies focus on the macro level properties of bone, the micro level properties may hold different clues about the

nature of bone and how bone responds to external stimuli, aging, disease and pharmaceutical treatments. In fact, at the micro level bone, has a hierarchical structure and is in part made up by the mineralized collagen matrix, the organization of collagen fibrils, and the structure lamellar layers. The focus of this project was to more readily enable the chemical and structural analysis of the hierarchical structure of bone at the micro level, in order to gain understanding of the interrelationship these properties of bone. We developed the techniques to exactly this, and used them to observe changes in the chemical and structural properties due to disease and pharmaceutical treatments.

6.1 Summary of Findings

Development of Reflection-based FTIRM

A thorough analysis of bone tissue requires a multimodal approach. To date, correlative studies such as these are typically performed across different specimens without performing the correlations on the same volume of tissue. While useful, this approach is limited by inter- and intra-specimen heterogeneity and reduces statistical power. In this study, we developed and demonstrated reflection-based FTIRM as an alternative approach to transmission-based FTIRM, enabling direct pixel-to-pixel correlations with other high resolution imaging modalities such as nanoindentation and qBSE on a single specimen, thereby providing accurate spatial associations between outcome measures. We demonstrated how absorbance spectra can be determined by FTIRM reflection measurements using the Kramers-Kronig transform [111], and that these spectra can be analyzed using standard methodology. This development is thus a step forward in enabling a multimodal approach to analyzing bone tissue, which can now include FTIRM. As added advantages, reflection-based FTIRM does not require additional hardware nor thin bone

specimens, and thus sample embedding is not strictly required, although it may facilitate the handling of thick bone specimens and small bone blocks. We anticipate that reflection-based FTIRM will more readily allow the pixel-to-pixel correlations between bone's material, mechanical, and morphological properties within a single specimen on the micron (and perhaps nano) scale. This can be used to study how region-specific differences in bone chemistry – caused by metabolic, genetic, environmental, or structural influences – affect the microscopic material properties of bone tissue and alter the local mechanical behavior. As such, this spatially-resolved, correlative approach will significantly contribute to a better understanding of the contributors to bone quality and fracture risk. For example, the effects of DMP1 on the biomineralization and structural properties of cortical bone using combined μCT and FTIRI on single specimens found that overexpression of DMP1 led to increased mineralization and increased structural cortical properties. These results were further correlated with altered biomechanical properties, such as decreased ductility [177].

Development of Simultaneous SAXS and WAXS Mapping of Bone

Direct visualization of the nanostructure of bone can be accomplished by electron microscopy (EM) or high resolution transmission x-ray microscopy (TXM). Although this remains the gold standard for imaging of collagen fibril arrays and the mineral crystals that coat and interleave these arrays, the typical requirement of ultrathin sections of bone makes sample preparation difficult. As an alternative, x-ray scattering techniques have been used extensively to study bone's nanostructure to study small changes in mineral crystal geometry during bone growth or under the influence of external stress of pharmaceutical treatments (SAXS) [56, 154, 160, 178], but also to investigate the collagen fibril organization in trabecular and cortical bone (WAXS) [45, 56, 155]. Compared to EM or TXM, the combined use of SAXS and WAXS

provides a much richer dataset from which both the collagen fibril and mineral crystal geometry and organization can be studied, and the sample thickness requirements are not as strict. Since the data are collected in reciprocal space, data analysis is more meticulous and we developed specific methods for the analysis of bone tissue. Although SAXS and WAXS patterns are analyzed separately, resulting information can be directly compared as the data were taken simultaneously and from the same location on the sample and data. Thus, the major advantage of this setup is that both the collagen fibrils and mineral crystals can be analyzed simultaneously, which ensures that their measured properties can be directly correlated on a pixel-to-pixel basis. We also developed simultaneous mapping of areas of tissue to investigate the collagen and mineral components of bone by using a combined SAXS and WAXS data collection setup. The use of a synchrotron source ensured sufficient photon flux and high spatial resolution, sufficient to resolve small features and spatial heterogeneity of the tissue.

Circumferential and Intracortical Lamellar Bone Differ in Chemistry

Investigations into the rat cortical bone chemistry of healthy bone tissue found a distinct geographical boundary in mineralization levels between the outer circumferential lamellar and the inner intracortical regions of bone. Interestingly, visible light microscopy found an identical division of the cortical bone, and identified the outer anatomical region as circumferential lamellar bone and the inner region as less organized, intracortical bone. The spatial correlation between mineralization and visible structure supports the notion that these two types of bone exhibit different chemistries [129]. Such differences were not observed in the mineral crystallinity, degree of collagen crosslinking or carbonate substitution levels in the apatite lattice. Nonetheless, these observations were the same for bone affected by osteoporosis and could ultimately result in different mechanical properties [15, 142], and ongoing research using

extensive has already pointed that removal of circumferential lamellar periosteal bone significantly reduces bone strength for prolonged period [179].

Fluoride Treatment Greatly Affects Mineral Chemistry in New and Old Bone

Upon prolonged treatment with sodium fluoride, in which the fluoride ion is known to be incorporated into the lattice of newly formed apatite, we found that newly formed bone was dramatically different compared to that of diseased specimens: Mineral crystal sizes were bigger and tissue mineralization higher. In addition, we found more subtle changes to existing, intracortical bone in the form of increased levels of carbonate substitution. The effects of sodium fluoride treatment are thus found in newly formed and existing bone alike, which is supported by previous findings that fluoride is incorporated into circumferential lamellar bone on the periosteum and endosteum as well as intracortical bone [139], but tends to accumulate in areas of high mineralization [70]. Nonetheless, the deleterious effects of osteoporosis are not completely mitigated by sodium fluoride treatment. For example, the reduced collagen crosslinking still persists in treated bone tissue [13]. The changes in bone chemistry that sodium fluoride is responsible for actually do not reduce fracture risk of the bone; In fact sodium fluoride has been shown to increase fracture risk as bone become more brittle [68]. Fluoride did not mitigate the deleterious effects of osteoporosis, but rather formed periosteal bone at a faster rate than normal and with a slightly different chemical signature. This suggests that other pharmaceutical drugs designed to promote bone growth might produce inferior bone, thereby potentially negating their anti fracture effectiveness.

Pharmaceutical Drugs Modulate Chemistry of New and Old Bone

In all specimens treated with alendronate and parathyroid hormone, a highly mineralized circumferential lamellar layer was present on the periosteal surface while the intracortical bone area was less mineralized. The tissue mineralization levels in the circumferential periosteal bone were no different compared OVX specimens. Nonetheless, the overall distribution of tissue mineralization was more even across the cortical shell compared to OVX. The efficacy of these two pharmaceutical drugs has been extensively described in literature. Alendronate treatment has been shown to reduce the risk of osteoporotic fractures, which is attributed to the inhibition of bone resorption and increase in bone mass [65, 66]. The anabolic action of parathyroid hormone treatment produces a physiological response in the form of an increase in serum Ca^{2+} [49, 58], and has been found to affect both cortical bone and trabecular bone. An increased cortical thickness has been demonstrated, which in itself is predicted to significantly contribute to bone strength. Previous studies have also reported increases to the uniformity of tissue level mineralization by alendronate [66, 67] and parathyroid hormone [56], which is in agreement with our results. Although the influence of these two treatments on cortical bone chemistry was more subtle than the sodium fluoride, these findings demonstrate that pharmaceutical drugs can modulate chemical properties in distinct ways, by affecting new and old bone differently and thereby affecting chemical uniformity across the cortical shell.

Collagen Isotropy and Alignment are Affected by Osteoporosis and Treatments

In addition to changes in chemistry, osteoporosis and pharmaceutical treatments have also been shown to affect the collagen and mineral structure of collagen fibrils. Specifically, the gap zones between successive collagen molecules that are filled with plate-like apatite mineral

crystals have been a recent target of investigating the nanostructure of bone tissue. We used synchrotron based simultaneous SAXS and WAXS mapping to investigate the mineral crystal size and shape and the orientation and degree of orientation of the collagen network at a high spatial resolution in cortical bone. Our findings confirm the alignment of collagen fibrils parallel to the endosteal and periosteal surface, as previously reported [45]. Our findings further suggest that osteoporosis altered the mineral crystal widths and the degree of collagen alignment in existing, intracortical bone. This indicates that existing bone can be affected by bone diseases, perhaps by the continued aging of the tissue. Interestingly, no differences in crystal geometry of newly formed periosteal bone were found in any of the groups, so the normal development of the crystals was not affected by disease or treatments. Further, the changes in collagen alignment induced by osteoporosis were mitigated by alendronate and sodium fluoride, but not by parathyroid hormone. This can also be seen as a product of continued aging; alendronate slows bone turnover [171] and sodium fluoride stabilizes the mineral lattice [70], while parathyroid hormone increases bone turnover [58]. As a result, parathyroid hormone offers no protection against the aging of bone, and in fact might help cause it.

6.2 Limitations of Study

Ovariectomized Rat as a Model for Post-Menopausal Osteoporosis

The ovariectomized rat model and post-menopausal osteoporosis share several characteristics that make the animal model suitable as a predictor for events in humans, such as increased bone turnover, onset of bone loss due to increased rates of resorption, and a similar response to pharmaceutical treatments such as estrogens, bisphosphonates and parathyroid hormone [180]. Unlike in humans, however, cortical bone in the Sprague Dawley rat does not normally undergo

Haversian remodeling and instead has a predominantly lamellar cortical structure [180]. Rat cortical bone can however undergo Haversian remodeling due to age or trauma. Because of this limitation, it is unknown whether results from the lamellar cortical structure of rat femurs in this study can be extrapolated to cortical bone in human femurs, which contains Haversian systems and undergoes additional types of remodeling. Furthermore, the doses of drugs used in this study were based on extrapolations from clinical doses in humans, and have been shown to affect bone quality and quantity [171]. Future research focusing on the partial contributions of lamellar cortical structure and Haversian systems on the biomechanical properties of human bone can put results from rodent studies into better perspective. Additionally, studies using human biopsies can directly investigate alternations to cortical bone properties.

Trabecular Bone was not Analyzed

Both cortical and trabecular bone contribute to the macro-mechanical properties of whole bone, and each may be affected differently by OVX and treatments. Trabecular bone has a higher turnover rate than cortical bone, and can thus be expected to have a bigger effect to osteoporosis and treatments. Since the size of trabeculae expands in the width, the bulk of the regional variability in trabecular bone is across trabeculae. Nonetheless, the contributions of trabecular microstructure are smaller than the contributions of the cortical component [181]. In this study, data was only taken from cortical bone. No trabecular bone was imaged due to the limited spatial resolution of the FTIRM and SAXS/WAXS imaging systems that were used. In addition, due to limited angular range of the WAXS detector and the wide range of mineral crystal orientations in trabecular bone, the mineral crystal reflections (notably the (002)) could not be measured with consistency. The best spatial resolution for these systems was 10 x 10 and 20 x 20 μm, respectively, while single trabeculae can have regions of interest that are smaller than 5 μm in a

single dimension. For example, a layer of newly added trabecular bone can be less than 3 μm wide, making accurate assessment difficult. However, it should be noted that the cortical shell has rich regional variability, both in the circumference (lateral, anterior, medial and posterior directions) and distance from the bone marrow, which were both captured in this study.

Further improvement of these techniques through the use of a 3rd generation synchrotron source and advanced resolution enhancement techniques would achieve the higher photon flux and spatial resolution needed to properly resolve the smaller features in trabecular bone. Further, since the (002) reflection is not continuous and its angular projection will likely vary in trabecular bone, it's projection on an off-angle WAXS camera cannot be guaranteed. As an alternative, a different reflection that is continuous and describes crystal width or thickness can be used.

Small Sample Size in the SAXS and WAXS Study

The small sample size and small imaged area per sample in the SAXS/WAXS study (n = 5 per group, 5 groups) was due to time constraints of limited synchrotron beam time. Although three days of synchrotron beam time were awarded on four consecutive cycles each, only 7 - 10 specimens were scanned per beam time (approximately 8 hours per sample). This slow scan speed was in part due to the small spot size of 20 x 20 μm and the 50 seconds scan time per spot, leading to a scan time speed of 160 x 160 μm per hour. In comparison, the cortical shell has a width of 400 to 600 μm, which is about 4 to 6 hours of scan time. As such, the area to be imaged was chosen to cross the entire cortical shell and have a width of 200 μm. Because of the small imaged area, the data mostly described the variability across the cortical shell, not the variability across different regions of cortical bone. Although the former is important as it describes

collagen and mineral properties in different types of bone (periosteal, endosteal, and intracortical), as well as new and old bone in the case of time studies, the latter describes tissue level mineral crystal uniformity and collagen isotropy which may be affected over larger period of time. However, since several hundred SAXS and WAXS patterns were collected per sample, statistically significant data could be obtained from each sample, from regions within sample, and from comparisons between groups. The use of a 3rd generation synchrotron source provides the necessary photon flux to reduce scan time per pixel and thus make imaging of larger areas more manageable. Additionally, advances in camera technology can further reduce dead time during detector readout, which in our studies accounted for approximately 35% of the scan time per pixel.

6.3 Future Directions

Multimodal imaging of a single specimen

Multimodal imaging provides a good assessment of the various properties of a single specimen, and allows for pixel-to-pixel and region-by-region comparisons of properties. With the development of reflection-based FTIRM, this technique can now be combined with qBSE, nanoCT and NI. Further development of Grazing Incidence SAXS (GISAXS) of polished bone blocks would allow this technique to be used alongside the previously mentioned techniques. Combined, a single specimen could be analyzed for material chemistry, tissue mineralization, morphological structure, mechanical properties, collagen alignment and mineral crystal geometry at micron spatial resolution. Aside from initial specimen preparation which involves flattening and polishing of a single surface of the bone block, no further adjustments are required. This

greatly reduces specimen preparation time and allows for a single feature in the specimen to be analyzed in the same state using all of these techniques.

This type of multimodal imaging opens the door to analyzing and correlating the aforementioned properties at a high spatial resolution for the investigation of the lamellar cortical structure, Haversian systems, and trabecular bone, but also for analyzing larger areas such as entire cortical cross-sections to investigate the efficacy of new and promising pharmaceutical drugs.

High Resolution FTIRM of Trabecular Bone

The spatial resolution of FPA-based FTIRM is typically limited to the wavelength of the incident IR light. In the case of imaging bone tissues, the spatial resolution is limited to 5 - 10 μm. Confocal FTIRM in conjunction with a synchrotron source can improve this by a factor of two to λ/2 [182, 183], thereby enabling the imaging of individual trabeculae. Because trabeculae are typically higher turnover than cortical bone, it is especially of interest to be able to distinguish between newly formed and existing bone in individual trabeculae. Higher resolution imagery of individual trabeculae may reveal distinct changes in newly formed bone and older bone in trabeculae. Further resolution enhancement to λ/4, thus approaching 1 μm, would help immensely in the study of individual trabeculae. To achieve this, efforts are underway to develop spatial deconvolution of oversampled IR imagery [184]. This type of deconvolution makes use of the Point Spread Function (PSF); a mathematical description of the response of the microscope to a point source [185]. In the case of oversampling FTIRM, the specimen can be considered as a collection of point sources that are spatially resolved using a deconvolution routine. A general equation is as follows:

$$g(r) = f(r) * h(r) + n(r)$$

where g(r) is the measured imagery, f(r) is the actual imagery, h(r) described the PSF and n(r) is added noise. Aside from added noise, an accurate description of the PSF can yield an accurate estimate of the actual imagery using a simple inverse function. However, added levels of noise n(r) complicate the deconvolution process. If the level of noise can be accurately described, an inverse filter (Wiener filter) can be used to estimate the actual imagery h(r). But the most common way to account for an approximation of the PSF while tolerating moderate levels of noise is the Lucy-Richardson deconvolution method, which iteratively resolves an estimate of the actual imagery while varying the noise n(r). Optionally, the algorithm can be used to also resolve the PSF (blind deconvolution) [186]. An example is shown in Figure 6-1 where 6 μm polystyrene beads were imaged using a FPA-based oversampling with a pixel resolution of 0.54 μm. In the raw image, a single bead is distinguishable from a crystal of beads. After deconvolution, the cluster of beads clearly shows three beads in a triangular formation, matching the configuration shown in the visible light image. The profile image shows that the peaks are sharper and more clearly distinguish the three cluster beads.

Visualization of collagen fibril organization at nanometer resolution

Several osteoporosis drugs, such as the anabolic parathyroid hormone treatment or the antiresorptive alendronate and residronate agents, are designed to act on the osteoblasts and osteoclasts in order to build new bone or slow bone remodeling, respectively. The aminobisphosphonates zoledronate, pamidronate, and alendronate have been shown to affect the osteoblast lineage and mineral nodule formation [187, 188], while the dual-acting bone agent Strontium Ranelate (SrR) has been shown to increase collagenous matrix formation in osteoblast

cells, leading to a reduced risk of vertebral fracture [189]. The effects of these drugs on osteoblasts and osteoclasts have been extensively studied in culture but primarily on the macroscopic (bulk) level. Alterations to the actin filaments and eventual apoptosis of osteoclasts has been shown to be the major events which lead to reduced bone resorption in patients treated with various bisphosphonates [190]. While some of these drugs are thought to increase collagen matrix formation, their effects on early-stage formation of mineral remain unclear. Investigation into how the overall structure and composition of new the mineralized collagen matrix differs from normal conditions is important to understanding the quality of this new tissue.

Although SAXS with a third generation synchrotron source can approach 1 μm spatial resolution, data collection times prohibit imaging over a large field as individual points on a sample are scanned in reciprocal space one at a time. Direct imaging of small gold nanosphere attached to specific antibody label [191] using a full-field detector is a faster alternative to imaging the collagen network. In the antibody labeling procedure, a collagen specific primary antibody is attached to exposed collagen fibrils, and a second antibody with a probe is attached to the primary antibody. This probe comes in the form of a fluorescent fluorophore (Nanoprobes, Yaphank NY) that can be imaged at a low resolution (~1 μm) to obtain a quick overview of the labeled specimen. A second probe in the form of a 50-nm gold nanosphere can be imaged at a much higher resolution (>40 nm) using TXM in phase contrast mode and accurately visualizes the distribution, density and alignment of collagen fibrils over a large area using an area detector. Optionally the gold nanosphere, and other metal ions such as calcium and iron, can be imaged using XFM of the Au L_α edge.

FTIRM as a tool to investigate the efficacy of new and promising pharmaceutical drugs

Several new potential drug treatments, such as sclerostin antibody and dentin matrix protein-1 (DMP1), are currently under development or are undergoing preclinical and clinical testing. Since the whole bone antifracture potential of is one of the most important attributes of drug development, high resolution FTIR imaging of cortical and trabecular components is typically not used during the development and testing phase. But high resolution can give insight into the efficacy of these drugs, and this can be used to improve potency and reduce side effects. For example, the involvement of DMP1 in the biomineralization process has recently attracted attention, and research is ongoing on the effects of overexpressing DMP1 on the level of tissue mineralization and tissue mechanical properties [192, 193]. FTIRM has been used to show that DMP1 overexpression accelerates mineralization of the cortical bone [177]. Another example is the (effectively anabolic) sclerostin antibody which has been shown to increase bone formation and increase tissue mineralization by blocking the canonical Wnt signaling pathway in osteoblasts, but how exactly the material chemistry of the tissue might be affected is unknown. Research is underway to investigate these changes using FTIRM. The osteoporotic drug Strontium Ranelate (SrR) is designed to act on both osteoblasts and osteoclasts in order to rebalance bone turnover and formation. Mechanistically, SrR is thought to inhibit bone resorption and promote bone formation by stimulating pre-osteoblast differentiation into osteoblasts. The binding of SrR to the calcium sensing receptor on the osteoblast cell surface is thought to mediate the beneficial effects of SrR [194]. Furthermore, the strontium cation is thought to be incorporated into newly formed mineral matrix, without having deleterious effects on matrix mineralization [189], although its effects on early-stage formation of mineral remain unclear. Investigation into how SrR affect the overall structure and composition of new mineral

matrix is important to understanding the quality of this new tissue. FTIRM is an exceptionally useful imaging tool in this case, as both the material chemistry and the SrR drug, by the IR active ranelate group, can be imaged simultaneously.

6.4 Conclusions

Osteoporosis is a silent disease that affects tens of millions of men and women in the Western world alone. The disease is characterized by low bone mass which increases the risk of bone fractures. Fortunately, bone health is easily monitored with routine checkups and if needed further deterioration of bone can be slowed with appropriate lifestyle changes and medication. Decades of research into the basic composition and structure of bone have laid the foundation for the development of pharmaceutical drug treatment to combat the disease. Although this has been largely a discovery process and often the more potent drugs have significant side effects, these medications are regularly used in combination with lifestyle changes to slow the progression of the disease. But recent research into the finer structure and regulatory pathways of bone formation and modeling may soon lead to a revolution of intelligent drug development to target specific pathways and deficiencies in the mineralized tissue. For example, many ongoing projects are focusing on promoting the formation of new and strong bone in order to strengthen the bone as a whole, while others are finding new ways to strengthen existing bone.

This study points out that pharmaceutical drugs can not only promote the formation of new and strong bone or prevent bone resorption, but that they can also modulate specific properties of existing bone that may have been compromised by disease. As these modulations cover a range of properties and affect the hierarchical structure of bone, there is a need for multi modal imaging of bone tissue to accurately evaluate new drug treatments. We developed new

methodologies that can accurately measure changes to a range of properties and at different hierarchical levels, such as the chemistry of cortical lamellar bone, the isotropy of collagen fibrils on the micron scale and the geometry of nanosized mineral crystal that interleave and coat collagen fibrils. We have applied these new techniques to monitor changes to bone as a function of disease and drug treatments. A key finding lies in the chemical properties of circumferential lamellar and intracortical bone: while the tissue mineralization of circumferential lamellar bone was found to be affected by OVX and treatments, the older intracortical bone was not. We also showed that OVX alters mineral crystal geometry in existing bone, while some treatments were found to mitigate these effects. Investigations into the collagen and mineral organization found that collagen isotropy is greatly increased in OVX, and that alendronate and fluoride acted to mitigate these changes, while mineral crystal geometry in periosteal bone was affected by OVX. Further work that focuses on the development of new methodologies to study cortical and trabecular bone structure, and investigations into a wider range of drugs including new drugs will aid in the development of more potent drugs designed to strengthen and improve the health of existing bone, thereby reducing fracture risk. This approach can also greatly improve the body's ability to repair bone fractures, which may occur in older and new bone.

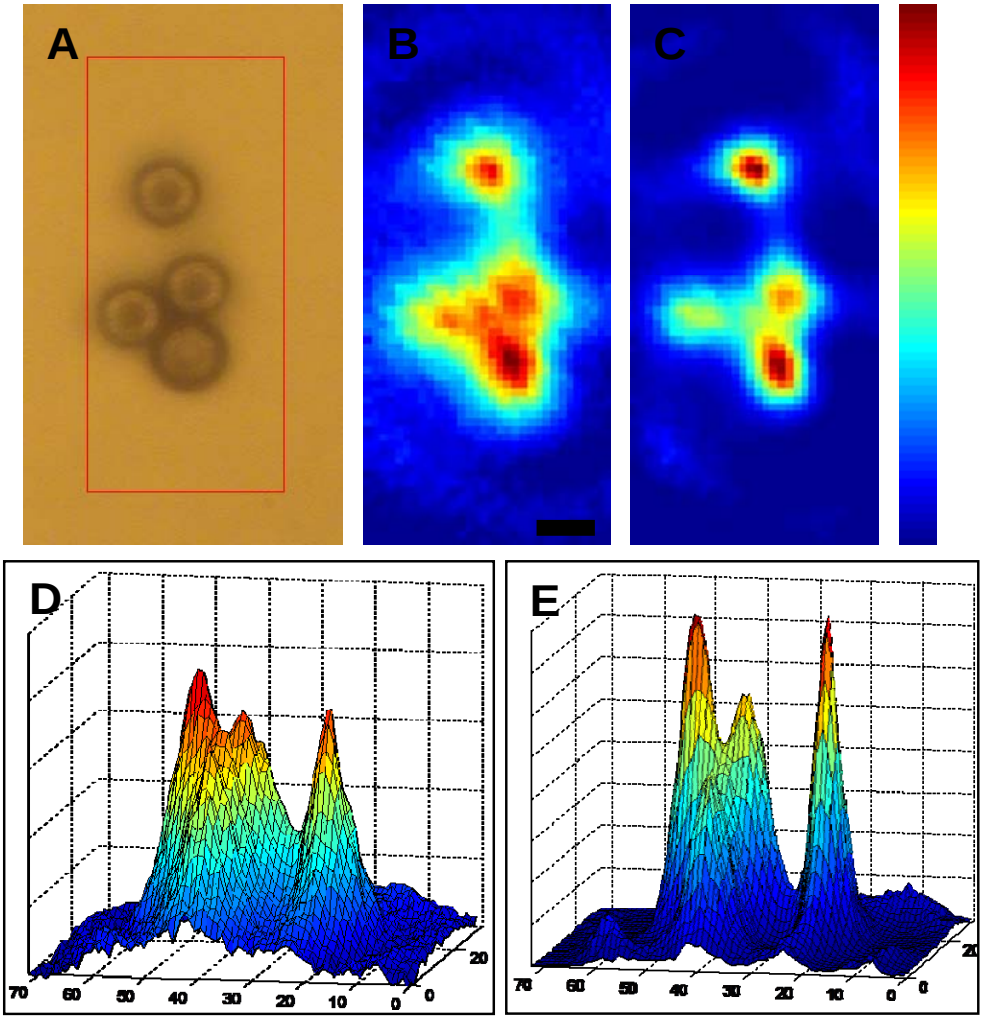

Figure 6-1: Example of PSF based spatial deconvolution of 6 µm polystyrene beads using a 74x objective and synchrotron IR light (585 mA). A) Visible image of 4 beads in a 17 x 39 µm area outlined by the red box. B) Integration of an absorption peak at 1450 cm^{-1} shows a cluster of beads and a single bead. C) After blind deconvolution, the cluster of beads is more defined and three distinct beads are apparent. In D and E, a side profile of the integration maps B and C are shown, respectively. The sharper and more defined peaks in E are the result of several iterations of deconvolution.

Bibliography

1. Baron, R., General Principles of Bone Biology. In *Primer of the Matabolic Diseases and Disorders of Mineral Metabolism*, Favus, M. J., Ed. American Society for Bone and Mineral Research: Washington, DC, 2003.

2. Burge, R.; Dawson-Hughes, B.; Solomon, D. H.; Wong, J. B.; King, A.; Tosteson, A., Incidence and economic burden of osteoporosis-related fractures in the United States, 2005-2025. *Journal of Bone and Mineral Research* **2007,** 22, (3), 465-75.

3. Harvey, N.; Dennison, E.; Cooper, C., Osteoporosis: impact on health and economics. *Nature Reviews Rheumatology* **2010,** 6, (2), 99-105.

4. Eastell, R., Pathogenesis of Postmenopausal Osteoporosis. In *Primer on the Metabolic Bone Diseases and Disorders of Mineral Metabolism*, 5 ed.; Favus, M. J., Ed. American Society for Bone and Mineral Researc; 5 edition (June 2006): Washington, DC, 2003; pp 314-323.

5. Heaney, R. P., Nutrition and Osteoporosis. In *Primer on the Metabolic Bone Diseases and Disorders of Mineral Metabolism*, 5 ed.; Favus, M. J., Ed. American Society for Bone and Mineral Researc; 5 edition (June 2006): Washington, DC, 2003; pp 352-355.

6. Lukert, B. P., Glucocortocoid-Induced Osteoporosis. In *Primer on the Metabolic Bone Diseases and Disorders of Mineral Metabolism*, 5 ed.; Favus, M. J., Ed. American Society for Bone and Mineral Researc; 5 edition (June 2006): Washington, DC, 2003; pp 364-370.

7. Link, T. M.; Majumdar, S., Current diagnostic techniques in the evaluation of bone architecture. *Current Osteoporosis Reports* **2004,** 2, (2), 47-52.

8. Kanis, J. A.; Johansson, H.; Oden, A.; McCloskey, E. V., Assessment of fracture risk. *European Journal of Radiology* **2009,** 71, (3), 392-7.

9. Lewis, G.; Nyman, J. S., The use of nanoindentation for characterizing the properties of mineralized hard tissues: State-of-the art review. *Journal of Biomedical Materials Research Part B: Applied Biomaterials* **2008,** 87B, (1), 286-301.

10. Zysset, P. K.; Guo, X. E.; Hoffler, C. E.; Moore, K. E.; Goldstein, S. A., Elastic modulus and hardness of cortical and trabecular bone lamellae measured by nanoindentation in the human femur. *Journal of Biomechanics* **1999,** 32, (10), 1005-12.

11. Marshall, D.; Johnell, O.; Wedel, H., Meta-analysis of how well measures of bone mineral density predict occurrence of osteoporotic fractures. *British Medical Journal* **1996,** 312, (7041), 1254-9.

12. Courtland, H. W.; Nasser, P.; Goldstone, A. B.; Spevak, L.; Boskey, A. L.; Jepsen, K. J., Fourier transform infrared imaging microspectroscopy and tissue-level mechanical testing reveal intraspecies variation in mouse bone mineral and matrix composition. *Calcified Tissue International* **2008,** 83, (5), 342-53.

13. Gourion-Arsiquaud, S.; Faibish, D.; Myers, E.; Spevak, L.; Compston, J.; Hodsman, A.; Shane, E.; Recker, R. R.; Boskey, E. R.; Boskey, A. L., Use of FTIR spectroscopic imaging to identify

parameters associated with fragility fracture. *Journal of Bone and Mineral Research* **2009,** 24, (9), 1565-71.

14. Ruppel, M. E.; Burr, D. B.; Miller, L. M., Chemical makeup of microdamaged bone differs from undamaged bone. *Bone* **2006,** 39, (2), 318-24.

15. Gupta, H. S.; Seto, J.; Wagermaier, W.; Zaslansky, P.; Boesecke, P.; Fratzl, P., Cooperative deformation of mineral and collagen in bone at the nanoscale. *Proceedings of the National Academy of Sciences* **2006,** 103, (47), 17741-6.

16. Summerlee, A. J. S., Bone formation and development. In *Bone in Clinical Orthopaedics: A Study in Comparative Osteology*, Sumner-Smith, G., Ed. AO Publishing: Dubendorf, 2002.

17. Ammann, P.; Rizzoli, R., Bone strength and its determinants. *Osteoporos International* **2003,** 14 Suppl 3, S13-8.

18. van der Meulen, M. C.; Jepsen, K. J.; Mikic, B., Understanding bone strength: size isn't everything. *Bone* **2001,** 29, (2), 101-4.

19. Boivin, G.; Meunier, P. J., The mineralization of bone tissue: a forgotten dimension in osteoporosis research. *Osteoporos International* **2003,** 14 Suppl 3, S19-24.

20. Ritchie, R. O., How does human bone resist fracture? *Annals of the New York Academy of Sciences* **2010,** 1192, (1), 72-80.

21. Parfitt, A. M., Misconceptions (2): turnover is always higher in cancellous than in cortical bone. *Bone* **2002,** 30, (6), 807-809.

22. Tommasini, S. M.; Trinward, A.; Acerbo, A. S.; De Carlo, F.; Miller, L. M.; Judex, S., Changes in intracortical microporosities induced by pharmaceutical treatment of osteoporosis as detected by high resolution micro-CT. *Bone* **2012,** 50, (3), 596-604.

23. Rho, J. Y.; Kuhn-Spearing, L.; Zioupos, P., Mechanical properties and the hierarchical structure of bone. *Medical Engineering & Physics* **1998,** 20, (2), 92-102.

24. Davison, K. S.; Siminoski, K.; Adachi, J. D.; Hanley, D. A.; Goltzman, D.; Hodsman, A. B.; Josse, R.; Kaiser, S.; Olszynski, W. P.; Papaioannou, A.; Ste-Marie, L.-G.; Kendler, D. L.; Tenenhouse, A.; Brown, J. P., Bone Strength: The Whole Is Greater Than the Sum of Its Parts. *Seminars in Arthritis and Rheumatism* **2006,** 36, (1), 22-31.

25. Rice, J. C.; Cowin, S. C.; Bowman, J. A., On the dependence of the elasticity and strength of cancellous bone on apparent density. *Journal of Biomechanics* **1988,** 21, (2), 155-68.

26. Rho, J. Y.; Ashman, R. B.; Turner, C. H., Young's modulus of trabecular and cortical bone material: ultrasonic and microtensile measurements. *Journal of Biomechanics* **1993,** 26, (2), 111-9.

27. Launey, M. E.; Buehler, M. J.; Ritchie, R. O., On the Mechanistic Origins of Toughness in Bone. *Annual Review of Materials Research* **2010,** 40, (1), 25-53.

28. Weiner, S.; Wagner, H. D., The Material Bone: Structure-Mechanical Function Relations. *Annual Review of Materials Science* **1998,** 28, (1), 271-298.

29. Liu, D.; Wagner, H. D.; Weiner, S., Bending and fracture of compact circumferential and osteonal lamellar bone of the baboon tibia. *Journal of Materials Science: Materials in Medicine* **2000,** 11, (1), 49-60.

30. Weiner, S.; Traub, W.; Wagner, H. D., Lamellar bone: structure-function relations. *Journal of Structural Biology* **1999,** 126, (3), 241-55.

31. Williams, J. L.; Lewis, J. L., Properties and an anisotropic model of cancellous bone from the proximal tibial epiphysis. *Journal of Biomechanical Engineering* **1982,** 104, (1), 50-6.

32. Hodgskinson, R.; Currey, J. D.; Evans, G. P., Hardness, an indicator of the mechanical competence of cancellous bone. *Journal of Orthopaedic Research* **1989,** 7, (5), 754-8.

33. Kuhn, J. L.; Goldstein, S. A.; Choi, K.; London, M.; Feldkamp, L. A.; Matthews, L. S., Comparison of the trabecular and cortical tissue moduli from human iliac crests. *Journal of Orthopaedic Research* **1989,** 7, (6), 876-84.

34. Liu, X. S.; Sajda, P.; Saha, P. K.; Wehrli, F. W.; Bevill, G.; Keaveny, T. M.; Guo, X. E., Complete volumetric decomposition of individual trabecular plates and rods and its morphological correlations with anisotropic elastic moduli in human trabecular bone. *Journal of Bone and Mineral Research* **2008,** 23, (2), 223-35.

35. Liu, X. S.; Sajda, P.; Saha, P. K.; Wehrli, F. W.; Guo, X. E., Quantification of the roles of trabecular microarchitecture and trabecular type in determining the elastic modulus of human trabecular bone. *Journal of Bone and Mineral Research* **2006,** 21, (10), 1608-17.

36. van Ruijven, L. J.; Giesen, E. B.; Mulder, L.; Farella, M.; van Eijden, T. M., The effect of bone loss on rod-like and plate-like trabeculae in the cancellous bone of the mandibular condyle. *Bone* **2005,** 36, (6), 1078-85.

37. Landis, W. J.; Hodgens, K. J.; Song, M. J.; Arena, J.; Kiyonaga, S.; Marko, M.; Owen, C.; McEwen, B. F., Mineralization of collagen may occur on fibril surfaces: evidence from conventional and high-voltage electron microscopy and three-dimensional imaging. *Journal of Structural Biology* **1996,** 117, (1), 24-35.

38. Burger, C.; Zhou, H. W.; Wang, H.; Sics, I.; Hsiao, B. S.; Chu, B.; Graham, L.; Glimcher, M. J., Lateral packing of mineral crystals in bone collagen fibrils. *Biophysics Journal* **2008,** 95, (4), 1985-92.

39. Saito, M.; Marumo, K., Collagen cross-links as a determinant of bone quality: a possible explanation for bone fragility in aging, osteoporosis, and diabetes mellitus. *Osteoporos International* **2010,** 21, (2), 195-214.

40. Jager, I.; Fratzl, P., Mineralized collagen fibrils: a mechanical model with a staggered arrangement of mineral particles. *Biophysics Journal* **2000,** 79, (4), 1737-46.

41. Skedros, J. G.; Hunt, K. J., Does the degree of laminarity correlate with site-specific differences in collagen fibre orientation in primary bone? An evaluation in the turkey ulna diaphysis. *Journal of Anatomy* **2004,** 205, (2), 121-134.

42. Martin, R. B.; Boardman, D. L., The effects of collagen fiber orientation, porosity, density, and mineralization on bovine cortical bone bending properties. *Journal of Biomechanics* **1993,** 26, (9), 1047-54.

43. Martin, R. B.; Ishida, J., The relative effects of collagen fiber orientation, porosity, density, and mineralization on bone strength. *Journal of Biomechanics* **1989,** 22, (5), 419-26.

44. Skedros, J. G.; Dayton, M. R.; Sybrowsky, C. L.; Bloebaum, R. D.; Bachus, K. N., The influence of collagen fiber orientation and other histocompositional characteristics on the mechanical properties of equine cortical bone. *Journal of Experimental Biology* **2006,** 209, (Pt 15), 3025-42.

45. Bunger, M. H.; Oxlund, H.; Hansen, T. K.; Sorensen, S.; Bibby, B. M.; Thomsen, J. S.; Langdahl, B. L.; Besenbacher, F.; Pedersen, J. S.; Birkedal, H., Strontium and bone nanostructure in normal and ovariectomized rats investigated by scanning small-angle X-ray scattering. *Calcified Tissue International* **2010,** 86, (4), 294-306.

46. Fratzl, P.; Gupta, H. S.; Paschalis, E. P.; Roschger, P., Structure and mechanical quality of the collagen-mineral nano-composite in bone. *Journal of Materials Chemistry* **2004,** 14, 2115-2123.

47. Ji, B.; Gao, H., Mechanical Principles of Biological Nanocomposites. *Annual Review of Materials Research* **2010,** 40, (1), 77-100.

48. Nordin, B. E. C.; Speed, R.; Aaron, J.; Crilly, R. G., Bone formation and resorption as the determinants of trabecular bone volume in postmenopausal osteoporosis. *The Lancet* **1981,** 318, (8241), 277-279.

49. Vesterby, A.; Mosekilde, L.; Gundersen, H. J.; Melsen, F.; Mosekilde, L.; Holme, K.; Sorensen, S., Biologically meaningful determinants of the in vitro strength of lumbar vertebrae. *Bone* **1991,** 12, (3), 219-24.

50. Ritzel, H.; Amling, M.; Posl, M.; Hahn, M.; Delling, G., The thickness of human vertebral cortical bone and its changes in aging and osteoporosis: a histomorphometric analysis of the complete spinal column from thirty-seven autopsy specimens. *Journal of Bone and Mineral Research* **1997,** 12, (1), 89-95.

51. Nalla, R. K.; Kruzic, J. J.; Kinney, J. H.; Ritchie, R. O., Effect of aging on the toughness of human cortical bone: evaluation by R-curves. *Bone* **2004,** 35, (6), 1240-6.

52. Ciarelli, T. E.; Fyhrie, D. P.; Schaffler, M. B.; Goldstein, S. A., Variations in three-dimensional cancellous bone architecture of the proximal femur in female hip fractures and in controls. *Journal of Bone and Mineral Research* **2000,** 15, (1), 32-40.

53. Parfitt, A. M.; Mathews, C. H.; Villanueva, A. R.; Kleerekoper, M.; Frame, B.; Rao, D. S., Relationships between surface, volume, and thickness of iliac trabecular bone in aging and in osteoporosis. Implications for the microanatomic and cellular mechanisms of bone loss. *Journal of Clinical Investigations* **1983,** 72, (4), 1396-409.

54. Geusens, P. P.; Roux, C. H.; Reid, D. M.; Lems, W. F.; Adami, S.; Adachi, J. D.; Sambrook, P. N.; Saag, K. G.; Lane, N. E.; Hochberg, M. C., Drug Insight: choosing a drug treatment strategy for women with osteoporosis-an evidence--based clinical perspective. *Nature Clinical Practice Rheumatology* **2008,** 4, (5), 240-8.

55. Theriault, R. L., Biology of bone metastases. *Cancer Control* **2012,** 19, (2), 92-101.

56. Valenta, A.; Roschger, P.; Fratzl-Zelman, N.; Kostenuik, P. J.; Dunstan, C. R.; Fratzl, P.; Klaushofer, K., Combined treatment with PTH (1-34) and OPG increases bone volume and uniformity of mineralization in aged ovariectomized rats. *Bone* **2005,** 37, (1), 87-95.

57. Glass, D. A., 2nd; Bialek, P.; Ahn, J. D.; Starbuck, M.; Patel, M. S.; Clevers, H.; Taketo, M. M.; Long, F.; McMahon, A. P.; Lang, R. A.; Karsenty, G., Canonical Wnt signaling in differentiated osteoblasts controls osteoclast differentiation. *Dev Cell* **2005,** 8, (5), 751-64.

58. Blair, H. C.; Zaidi, M.; Schlesinger, P. H., Mechanisms balancing skeletal matrix synthesis and degradation. *The Biochemical Journal* **2002,** 364, (Pt 2), 329-41.

59. Jilka, R. L., Molecular and cellular mechanisms of the anabolic effect of intermittent PTH. *Bone* **2007,** 40, (6), 1434-46.

60. Dempster, D. W.; Cosman, F.; Kurland, E. S.; Zhou, H.; Nieves, J.; Woelfert, L.; Shane, E.; Plavetic, K.; Muller, R.; Bilezikian, J.; Lindsay, R., Effects of daily treatment with parathyroid hormone on bone microarchitecture and turnover in patients with osteoporosis: a paired biopsy study. *Journal of Bone and Mineral Research* **2001,** 16, (10), 1846-53.

61. Misof, B. M.; Roschger, P.; Cosman, F.; Kurland, E. S.; Tesch, W.; Messmer, P.; Dempster, D. W.; Nieves, J.; Shane, E.; Fratzl, P.; Klaushofer, K.; Bilezikian, J.; Lindsay, R., Effects of Intermittent Parathyroid Hormone Administration on Bone Mineralization Density in Iliac Crest Biopsies from Patients with Osteoporosis: A Paired Study before and after Treatment. *Journal of Clinical Endocrinology & Metabolism* **2003,** 88, (3), 1150-1156.

62. Liberman, U. A.; Weiss, S. R.; Broll, J.; Minne, H. W.; Quan, H.; Bell, N. H.; Rodriguez-Portales, J.; Downs, R. W., Jr.; Dequeker, J.; Favus, M., Effect of oral alendronate on bone mineral density and the incidence of fractures in postmenopausal osteoporosis. The Alendronate Phase III Osteoporosis Treatment Study Group. *N Engl J Med* **1995,** 333, (22), 1437-43.

63. Fisher, J. E.; Rogers, M. J.; Halasy, J. M.; Luckman, S. P.; Hughes, D. E.; Masarachia, P. J.; Wesolowski, G.; Russell, R. G.; Rodan, G. A.; Reszka, A. A., Alendronate mechanism of action: geranylgeraniol, an intermediate in the mevalonate pathway, prevents inhibition of osteoclast formation, bone resorption, and kinase activation in vitro. *Proc Natl Acad Sci U S A* **1999,** 96, (1), 133-8.

64. Bergstrom, J. D.; Bostedor, R. G.; Masarachia, P. J.; Reszka, A. A.; Rodan, G., Alendronate is a specific, nanomolar inhibitor of farnesyl diphosphate synthase. *Arch Biochem Biophys* **2000,** 373, (1), 231-41.

65. Black, D. M.; Greenspan, S. L.; Ensrud, K. E.; Palermo, L.; McGowan, J. A.; Lang, T. F.; Garnero, P.; Bouxsein, M. L.; Bilezikian, J. P.; Rosen, C. J., The effects of parathyroid hormone and alendronate alone or in combination in postmenopausal osteoporosis. *New England Journal of Medicine* **2003,** 349, (13), 1207-15.

66. Roschger, P.; Rinnerthaler, S.; Yates, J.; Rodan, G. A.; Fratzl, P.; Klaushofer, K., Alendronate increases degree and uniformity of mineralization in cancellous bone and decreases the porosity in cortical bone of osteoporotic women. *Bone* **2001,** 29, (2), 185-91.

67. Roschger, P.; Fratzl, P.; Klaushofer, K.; Rodan, G., Mineralization of cancellous bone after alendronate and sodium fluoride treatment: a quantitative backscattered electron imaging study on minipig ribs. *Bone* **1997,** 20, (5), 393-7.

68. Aaron, J. E.; de Vernejoul, M. C.; Kanis, J. A., The effect of sodium fluoride on trabecular architecture. *Bone* **1991,** 12, (5), 307-10.

69. Lau, K. H.; Baylink, D. J., Molecular mechanism of action of fluoride on bone cells. *J Bone Miner Res* **1998,** 13, (11), 1660-7.

70. Grynpas, M. D., Fluoride effects on bone crystals. *Journal of Bone and Mineral Research* **1990,** 5 Suppl 1, S169-75.

71. Cummings, S. R.; Bates, D.; Black, D. M., Clinical Use of Bone Densitometry: Scientific Review. *The Journal of the American Medical Association* **2002,** 288, (15), 1889-1897.

72. Burr, D. B.; Milgrom, C.; Fyhrie, D.; Forwood, M.; Nyska, M.; Finestone, A.; Hoshaw, S.; Saiag, E.; Simkin, A., In vivo measurement of human tibial strains during vigorous activity. *Bone* **1996,** 18, (5), 405-10.

73. Lanyon, L. E.; Hampson, W. G.; Goodship, A. E.; Shah, J. S., Bone deformation recorded in vivo from strain gauges attached to the human tibial shaft. *Acta Orthop Scand* **1975,** 46, (2), 256-68.

74. Sharir, A.; Barak, M. M.; Shahar, R., Whole bone mechanics and mechanical testing. *The Veterinary Journal* **2008,** 177, (1), 8-17.

75. Beaupied, H.; Lespessailles, E.; Benhamou, C.-L., Evaluation of macrostructural bone biomechanics. *Joint Bone Spine* **2007,** 74, (3), 233-239.

76. Oliver, W. C.; Pharr, G. M., An improved technique for determining hardness and elastic modulus using load and displacement sensing indentation experiments. *Journal of Materials Research* **1992,** 7, (6), 1564-1583.

77. Oliver, W. C.; Pharr, G. M., Measurement of hardness and elastic modulus by instrumented indentation: Advances in understanding and refinements to methodology. *Journal of Material Research* **2004,** 19, (1), 3-20.

78. Currey, J. D.; Brear, K., Hardness, Young's modulus and yield stress in mammalian mineralized tissues. *Journal of Materials Science: Materials in Medicine* **1990,** 1, (1), 14-20.

79. Paschalis, E. P.; Verdelis, K.; Doty, S. B.; Boskey, A. L.; Mendelsohn, R.; Yamauchi, M., Spectroscopic characterization of collagen cross-links in bone. *Journal of Bone and Mineral Research* **2001,** 16, (10), 1821-8.

80. Aparicio, S.; Doty, S. B.; Camacho, N. P.; Paschalis, E. P.; Spevak, L.; Mendelsohn, R.; Boskey, A. L., Optimal methods for processing mineralized tissues for Fourier transform infrared microspectroscopy. *Calcified Tissue International* **2002,** 70, (5), 422-9.

81. Paschalis, E. P.; DiCarlo, E.; Betts, F.; Sherman, P.; Mendelsohn, R.; Boskey, A. L., FTIR microspectroscopic analysis of human osteonal bone. *Calcified Tissue International* **1996,** 59, (6), 480-7.

82. Camacho, N. P.; Carroll, P.; Raggio, C. L., Fourier transform infrared imaging spectroscopy (FT-IRIS) of mineralization in bisphosphonate-treated oim/oim mice. *Calcified Tissue International* **2003,** 72, (5), 604-9.

83. Otomo, H.; Sakai, A.; Ikeda, S.; Tanaka, S.; Ito, M.; Phipps, R. J.; Nakamura, T., Regulation of mineral-to-matrix ratio of lumbar trabecular bone in ovariectomized rats treated with risedronate in combination with or without vitamin K2. *Journal of Bone and Mineral Metabolism* **2004,** 22, (5), 404-14.

84. Akkus, O.; Adar, F.; Schaffler, M. B., Age-related changes in physicochemical properties of mineral crystals are related to impaired mechanical function of cortical bone. *Bone* **2004,** 34, (3), 443-53.

85. Akkus, O.; Polyakova-Akkus, A.; Adar, F.; Schaffler, M. B., Aging of microstructural compartments in human compact bone. *Journal of Bone and Mineral Research* **2003,** 18, (6), 1012-9.

86. Timlin, J. A.; Carden, A.; Morris, M. D., Chemical Microstructure of Cortical Bone Probed by Raman Transects. *Applied Spectroscopy* **1999,** 53, (11), 1429-1435.

87. Smith, R.; Rehman, I., Fourier transform Raman spectroscopic studies of human bone. *Journal of Materials Science: Materials in Medicine* **1994,** 5, (9), 775-778.

88. Kubisz, L.; Połomska, M., FT NIR Raman studies on γ-irradiated bone. *Spectrochimica Acta Part A: Molecular and Biomolecular Spectroscopy* **2007,** 66, (3), 616-625.

89. Howell, P. G. T.; Davy, K. M. W.; Boyde, A., Mean atomic number and backscattered electron coefficient calculations for some materials with low mean atomic number. *Scanning* **1998,** 20, (1), 35-40.

90. Ferguson, V. L.; Bushby, A. J.; Boyde, A., Nanomechanical properties and mineral concentration in articular calcified cartilage and subchondral bone. *Journal of Anatomy* **2003,** 203, (2), 191-202.

91. Boyde, A.; Travers, R.; Glorieux, F. H.; Jones, S. J., The Mineralization Density of Iliac Crest Bone from Children with Osteogenesis Imperfecta. *Calcified Tissue International* **1999,** 64, (3), 185-190.

92. Buie, H. R.; Campbell, G. M.; Klinck, R. J.; MacNeil, J. A.; Boyd, S. K., Automatic segmentation of cortical and trabecular compartments based on a dual threshold technique for in vivo micro-CT bone analysis. *Bone* **2007,** 41, (4), 505-15.

93. Jiang, Y.; Zhao, J.; Liao, E. Y.; Dai, R. C.; Wu, X. P.; Genant, H. K., Application of micro-CT assessment of 3-D bone microstructure in preclinical and clinical studies. *Journal of Bone and Mineral Metabolism* **2005,** 23 Suppl, 122-31.

94. Schneider, P.; Meier, M.; Wepf, R.; Müller, R., Towards quantitative 3D imaging of the osteocyte lacuno-canalicular network. *Bone* **2010,** 47, (5), 848-858.

95. Andrews, J. C.; Almeida, E.; van der Meulen, M. C. H.; Alwood, J. S.; Lee, C.; Liu, Y.; Chen, J.; Meirer, F.; Feser, M.; Gelb, J.; Rudati, J.; Tkachuk, A.; Yun, W.; Pianetta, P., Nanoscale X-Ray Microscopic Imaging of Mammalian Mineralized Tissue. *Microscopy and Microanalysis* **2010,** 16, (03), 327-336.

96. Rubin, M. A.; Jasiuk, I.; Taylor, J.; Rubin, J.; Ganey, T.; Apkarian, R. P., TEM analysis of the nanostructure of normal and osteoporotic human trabecular bone. *Bone* **2003,** 33, (3), 270-282.

97. Tracy, B. M.; Doremus, R. H., Direct electron microscopy studies of the bone—hydroxylapatite interface. *Journal of Biomedical Materials Research* **1984,** 18, (7), 719-726.

98. Ebenstein, D. M.; Pruitt, L. A., Nanoindentation of biological materials. *Nano Today* **2006,** 1, (3), 26-33.

99. Judex, S.; Boyd, S.; Qin, Y. X.; Miller, L.; Muller, R.; Rubin, C., Combining high-resolution micro-computed tomography with material composition to define the quality of bone tissue. *Curr Osteoporos Rep* **2003,** 1, (1), 11-9.

100. Miller, L. M.; Little, W.; Schirmer, A.; Sheik, F.; Busa, B.; Judex, S., Accretion of bone quantity and quality in the developing mouse skeleton. *Journal of Bone and Mineral Research* **2007,** 22, (7), 1037-45.

101. Donnelly, E.; Chen, D. X.; Boskey, A. L.; Baker, S. P.; van der Meulen, M. C., Contribution of Mineral to Bone Structural Behavior and Tissue Mechanical Properties. *Calcified Tissue International* **2010**.

102. Isaksson, H.; Malkiewicz, M.; Nowak, R.; Helminen, H. J.; Jurvelin, J. S., Rabbit cortical bone tissue increases its elastic stiffness but becomes less viscoelastic with age. *Bone* **2010,** 47, (6), 1030-1038.

103. Burket, J.; Gourion-Arsiquaud, S.; Havill, L. M.; Baker, S. P.; Boskey, A. L.; van der Meulen, M. C., Microstructure and nanomechanical properties in osteons relate to tissue and animal age. *Journal of Biomechanics* **2011,** 44, (2), 277-84.

104. Gourion-Arsiquaud, S.; Burket, J. C.; Havill, L. M.; DiCarlo, E.; Doty, S. B.; Mendelsohn, R.; van der Meulen, M. C.; Boskey, A. L., Spatial variation in osteonal bone properties relative to tissue and animal age. *Journal of Bone and Mineral Research* **2009,** 24, (7), 1271-81.

105. Bala, Y.; Farlay, D.; Delmas, P. D.; Meunier, P. J.; Boivin, G., Time sequence of secondary mineralization and microhardness in cortical and cancellous bone from ewes. *Bone* **2010,** 46, (4), 1204-12.

106. Brennan, O.; Kennedy, O. D.; Lee, T. C.; Rackard, S. M.; O'Brien, F. J.; McNamara, L. M., The effects of estrogen deficiency and bisphosphonate treatment on tissue mineralisation and stiffness in an ovine model of osteoporosis. *Journal of Biomechanics* **2011,** 44, (3), 386-90.

107. Boskey, A. L.; Spevak, L.; Weinstein, R. S., Spectroscopic markers of bone quality in alendronate-treated postmenopausal women. *Osteoporos International* **2009,** 20, (5), 793-800.

108. Pleshko, N. L.; Boskey, A. L.; Mendelsohn, R., An FT-IR microscopic investigation of the effects of tissue preservation on bone. *Calcified Tissue International* **1992,** 51, (1), 72-7.

109. Ou-Yang, H.; Paschalis, E. P.; Mayo, W. E.; Boskey, A. L.; Mendelsohn, R., Infrared microscopic imaging of bone: spatial distribution of CO3(2-). *Journal of Bone and Mineral Research* **2001,** 16, (5), 893-900.

110. Paschalis, E. P.; Betts, F.; DiCarlo, E.; Mendelsohn, R.; Boskey, A. L., FTIR microspectroscopic analysis of human iliac crest biopsies from untreated osteoporotic bone. *Calcif Tissue Int* **1997,** 61, (6), 487-92.

111. Lucarini, V.; Saarinen, J. J.; Peiponen, K.-E.; Vartiainen, E. M., *Kramers-Kronig Relations in Optical Materials Research*. Springer: Berlin, 2005; Vol. 110.

112. Allara, D. L.; Baca, A.; Pryde, C. A., Distortions of Band Shapes in External Reflection Infrared Spectra of Thin Polymer Films on Metal Substrates. *Macromolecules* **1978,** 11, (6), 1215-1220.

113. Davis, B. J.; Carney, P. S.; Bhargava, R., Theory of mid-infrared absorption microspectroscopy: II. Heterogeneous samples. *Analytical Chemistry* **2010,** 82, (9), 3487-99.

114. Ahrenkiel, R. K., Modified Kramers-Kronig Analysis of Optical Spectra. *J. Opt. Soc. Am.* **1971,** 61, (12), 1651-1655.

115. Palmer, K. F.; Williams, M. Z.; Budde, B. A., Multiply Subtractive Kramers-Kronig Analysis of Optical Data. *Appl. Opt.* **1998,** 37, (13), 2660-2673.

116. Vartiainen, E. M.; Peiponen, K.-E.; Asakura, T., Phase Retrieval in Optical Spectroscopy: Resolving Optical Constants from Power Spectra. *Applied Spectroscopy* **1996,** 50, (10), 1283-1289.

117. Jansen, G. J.; Mansfield, S. P.; Miedl, G., A leveling device for polished microsections. *The American Mineralogist* **1971,** 56, 380-381.

118. Kanis, J. A.; McCloskey, E. V.; Johansson, H.; Oden, A.; Melton, L. J., 3rd; Khaltaev, N., A reference standard for the description of osteoporosis. *Bone* **2008,** 42, (3), 467-75.

119. Chappard, D.; Basle, M. F.; Legrand, E.; Audran, M., New laboratory tools in the assessment of bone quality. *Osteoporos International* **2011,** 22, (8), 2225-40.

120. Morris, M. D.; Mandair, G. S., Raman assessment of bone quality. *Clininical Orthopaedics Related Research* **2011,** 469, (8), 2160-9.

121. Buckwalter, J. A.; Glimcher, M. J.; Cooper, R. R.; Recker, R., Bone biology. I: Structure, blood supply, cells, matrix, and mineralization. *The Journal of Bone & Joint Surgery* **1995,** 77, (8), 1256-1275.

122. Buckwalter, J. A.; Glimcher, M. J.; Cooper, R. R.; Recker, R., Bone biology. II: Formation, form, modeling, remodeling, and regulation of cell function. *The Journal of Bone & Joint Surgery* **1995,** 77, (8), 1276-1289.

123. Holtorf, H. L.; Jansen, J. A.; Mikos, A. G., Modulation of cell differentiation in bone tissue engineering constructs cultured in a bioreactor. *Advances in Experimental Medicine and Biology* **2007,** 585, 225-41.

124. Currey, J. D., The many adaptations of bone. *Journal of Biomechanics* **2003,** 36, (10), 1487-95.

125. Seto, J.; Gupta, H. S.; Zaslansky, P.; Wagner, H. D.; Fratzl, P., Tough Lessons From Bone: Extreme Mechanical Anisotropy at the Mesoscale. *Advanced Functional Materials* **2008,** 18, (13), 1905-1911.

126. Turner, C. H.; Forwood, M. R.; Rho, J. Y.; Yoshikawa, T., Mechanical loading thresholds for lamellar and woven bone formation. *Journal of Bone and Mineral Research* **1994,** 9, (1), 87-97.

127. Schaffler, M. B.; Radin, E. L.; Burr, D. B., Long-term fatigue behavior of compact bone at low strain magnitude and rate. *Bone* **1990,** 11, (5), 321-6.

128. McKenzie, J. A.; Silva, M. J., Comparing histological, vascular and molecular responses associated with woven and lamellar bone formation induced by mechanical loading in the rat ulna. *Bone* **2011,** 48, (2), 250-8.

129. Feng, L.; Jasiuk, I., Multi-scale characterization of swine femoral cortical bone. *Journal of Biomechanics* **2011,** 44, (2), 313-20.

130. Busa, B.; Miller, L. M.; Rubin, C. T.; Qin, Y. X.; Judex, S., Rapid establishment of chemical and mechanical properties during lamellar bone formation. *Calcified Tissue International* **2005,** 77, (6), 386-94.

131. Fuchs, R. K.; Allen, M. R.; Ruppel, M. E.; Diab, T.; Phipps, R. J.; Miller, L. M.; Burr, D. B., In situ examination of the time-course for secondary mineralization of Haversian bone using synchrotron Fourier transform infrared microspectroscopy. *Matrix Biology* **2008,** 27, (1), 34-41.

132. Pleshko, N.; Boskey, A.; Mendelsohn, R., Novel infrared spectroscopic method for the determination of crystallinity of hydroxyapatite minerals. *Biophysics Journal* **1991,** 60, (4), 786-93.

133. Boskey, A. L.; Mendelsohn, R., Infrared spectroscopic characterization of mineralized tissues. *Vibrational Spectroscopy* **2005,** 38, (1-2), 107-114.

134. Paschalis, E. P.; Burr, D. B.; Mendelsohn, R.; Hock, J. M.; Boskey, A. L., Bone mineral and collagen quality in humeri of ovariectomized cynomolgus monkeys given rhPTH(1-34) for 18 months. *Journal of Bone and Mineral Research* **2003,** 18, (4), 769-75.

135. Kazanci, M.; Roschger, P.; Paschalis, E. P.; Klaushofer, K.; Fratzl, P., Bone osteonal tissues by Raman spectral mapping: orientation-composition. *Journal of Structural Biology* **2006,** 156, (3), 489-96.

136. Kazanci, M.; Wagner, H. D.; Manjubala, N. I.; Gupta, H. S.; Paschalis, E.; Roschger, P.; Fratzl, P., Raman imaging of two orthogonal planes within cortical bone. *Bone* **2007,** 41, (3), 456-61.

137. Acerbo, A. S.; Carr, G. L.; Judex, S.; Miller, L. M., Imaging the Material Properties of Bone Specimens Using Reflection-Based Infrared Microspectroscopy. *Analytical Chemistry* **2012,** 84, (8), 3607-3613.

138. Mehta, S.; Reed, B.; Antich, P., Effects of high levels of fluoride on bone formation: an in vitro model system. *Biomaterials* **1995,** 16, (2), 97-102.

139. Narita, N.; Kato, K.; Nakagaki, H.; Ohno, N.; Kameyama, Y.; Weatherell, J. A., Distribution of fluoride concentration in the rat's bone. *Calcified Tissue International* **1990,** 46, (3), 200-4.

140. Santos, R. V.; Clayton, R. N., The carbonate content in high-temperature apatite; an analytical method applied to apatite from the Jacupiranga alkaline complex. *American Mineralogist* **1995,** 80, (3-4), 336-344.

141. Penel, G.; Leroy, G.; Rey, C.; Sombret, B.; Huvenne, J. P.; Bres, E., Infrared and Raman microspectrometry study of fluor-fluor-hydroxy and hydroxy-apatite powders. *J Mater Sci Mater Med* **1997,** 8, (5), 271-6.

142. Tai, K.; Qi, H.; Ortiz, C., Effect of mineral content on the nanoindentation properties and nanoscale deformation mechanisms of bovine tibial cortical bone. *Journal of Materials Science: Materials in Medicine* **2005,** 16, (10), 947-959.

143. Jepsen, K. J., Systems analysis of bone. *Wiley Interdisciplinary Reviews: Systems Biology and Medicine* **2009,** 1, (1), 73-88.

144. Wronski, T. J.; Walsh, C. C.; Ignaszewski, L. A., Histologic evidence for osteopenia and increased bone turnover in ovariectomized rats. *Bone* **1986,** 7, (2), 119-23.

145. Sontag, W., Quantitative measurement of periosteal and cortical-endosteal bone formation and resorption in the midshaft of female rat femur. *Bone* **1986,** 7, (1), 55-62.

146. Jiang, Y.; Zhao, J.; Van Audekercke, R.; Dequeker, J.; Geusens, P., Effects of low-dose long-term sodium fluoride preventive treatment on rat bone mass and biomechanical properties. *Calcified Tissue International* **1996,** 58, (1), 30-9.

147. Jee, W. S.; Yao, W., Overview: animal models of osteopenia and osteoporosis. *Journal of Musculoskeletal and Neuronal Interactions* **2001,** 1, (3), 193-207.

148. Grynpas, M. D.; Cheng, P. T., Fluoride reduces the rate of dissolution of bone. *Bone and Mineral* **1988,** 5, (1), 1-9.

149. Mousny, M.; Omelon, S.; Wise, L.; Everett, E. T.; Dumitriu, M.; Holmyard, D. P.; Banse, X.; Devogelaer, J. P.; Grynpas, M. D., Fluoride effects on bone formation and mineralization are influenced by genetics. *Bone* **2008,** 43, (6), 1067-74.

150. Odvina, C. V.; Zerwekh, J. E.; Rao, D. S.; Maalouf, N.; Gottschalk, F. A.; Pak, C. Y. C., Severely Suppressed Bone Turnover: A Potential Complication of Alendronate Therapy. *Journal of Clinical Endocrinology & Metabolism* **2005,** 90, (3), 1294-1301.

151. Kneissel, M.; Boyde, A.; Gasser, J. A., Bone tissue and its mineralization in aged estrogen-depleted rats after long-term intermittent treatment with parathyroid hormone (PTH) analog SDZ PTS 893 or human PTH(1-34). *Bone* **2001,** 28, (3), 237-250.

152. Compston, J. E., Skeletal actions of intermittent parathyroid hormone: Effects on bone remodelling and structure. *Bone* **2007,** 40, (6), 1447-1452.

153. Rubin, C. T.; Lanyon, L. E., Regulation of bone mass by mechanical strain magnitude. *Calcif Tissue Int* **1985,** 37, (4), 411-7.

154. Fratzl, P.; Paris, O.; Klaushofer, K.; Landis, W. J., Bone mineralization in an osteogenesis imperfecta mouse model studied by small-angle x-ray scattering. *Journal of Clinical Investigations* **1996,** 97, (2), 396-402.

155. Almer, J. D.; Stock, S. R., Internal strains and stresses measured in cortical bone via high-energy X-ray diffraction. *Journal of Structural Biology* **2005,** 152, (1), 14-27.

156. Wagermaier, W.; Gupta, H. S.; Gourrier, A.; Paris, O.; Roschger, P.; Burghammer, M.; Riekel, C.; Fratzl, P., Scanning texture analysis of lamellar bone using microbeam synchrotron X-ray radiation. *Journal of Applied Crystallography* **2007,** 40, (1), 115-120.

157. Zizak, I.; Roschger, P.; Paris, O.; Misof, B. M.; Berzlanovich, A.; Bernstorff, S.; Amenitsch, H.; Klaushofer, K.; Fratzl, P., Characteristics of mineral particles in the human bone/cartilage interface. *Journal of Structural Biology* **2003,** 141, (3), 208-17.

158. Gourrier, A.; Wagermaier, W.; Burghammer, M.; Lammie, D.; Gupta, H. S.; Fratzl, P.; Riekel, C.; Wess, T. J.; Paris, O., Scanning X-ray imaging with small-angle scattering contrast. *Journal of Applied Crystallography* **2007,** 40, (s1), s78-s82.

159. Allaire, M.; Yang, L., Biomolecular solution X-ray scattering at the National Synchrotron Light Source. *Journal of Synchrotron Radiation* **2011,** 18, (1), 41-4.

160. Fratzl, P.; Schreiber, S.; Klaushofer, K., Bone mineralization as studied by small-angle x-ray scattering. *Connective Tissue Research* **1996,** 34, (4), 247-54.

161. Camacho, N. P.; Rinnerthaler, S.; Paschalis, E. P.; Mendelsohn, R.; Boskey, A. L.; Fratzl, P., Complementary information on bone ultrastructure from scanning small angle X-ray scattering and Fourier-transform infrared microspectroscopy. *Bone* **1999,** 25, (3), 287-93.

162. Lange, C.; Li, C.; Manjubala, I.; Wagermaier, W.; Kuhnisch, J.; Kolanczyk, M.; Mundlos, S.; Knaus, P.; Fratzl, P., Fetal and postnatal mouse bone tissue contains more calcium than is present in hydroxyapatite. *Journal of Structural Biology* **2011,** 176, (2), 159-67.

163. Rinnerthaler, S.; Roschger, P.; Jakob, H. F.; Nader, A.; Klaushofer, K.; Fratzl, P., Scanning small angle X-ray scattering analysis of human bone sections. *Calcif Tissue Int* **1999,** 64, (5), 422-9.

164. Hauge Bunger, M.; Foss, M.; Erlacher, K.; Bruun Hovgaard, M.; Chevallier, J.; Langdahl, B.; Bunger, C.; Birkedal, H.; Besenbacher, F.; Skov Pedersen, J., Nanostructure of the neurocentral growth plate: Insight from scanning small angle X-ray scattering, atomic force microscopy and scanning electron microscopy. *Bone* **2006,** 39, (3), 530-41.

165. Price, R. I.; Lees, S.; Kirschner, D. A., X-ray diffraction analysis of tendon collagen at ambient and cryogenic temperatures: role of hydration. *Int J Biol Macromol* **1997,** 20, (1), 23-33.

166. Handschin, R. G.; Stern, W. B., Crystallographic lattice refinement of human bone. *Calcif Tissue Int* **1992,** 51, (2), 111-20.

167. Burnell, J. M.; Teubner, E. J.; Miller, A. G., Normal maturational changes in bone matrix, mineral, and crystal size in the rat. *Calcif Tissue Int* **1980,** 31, (1), 13-9.

168. Farlay, D.; Panczer, G.; Rey, C.; Delmas, P.; Boivin, G., Mineral maturity and crystallinity index are distinct characteristics of bone mineral. *Journal of Bone and Mineral Metabolism* **2010,** 28, (4), 433-445.

169. Sudarsanan, K.; Young, R. A., Significant precision in crystal structural details. Holly Springs hydroxyapatite. *Acta Crystallographica Section B* **1969,** 25, (8), 1534-1543.

170. Fratzl, P.; Fratzl-Zelman, N.; Klaushofer, K.; Vogl, G.; Koller, K., Nucleation and growth of mineral crystals in bone studied by small-angle X-ray scattering. *Calcif Tissue Int* **1991,** 48, (6), 407-13.

171. Mosekilde, L.; Thomsen, J. S.; Mackey, M. S.; Phipps, R. J., Treatment with risedronate or alendronate prevents hind-limb immobilization-induced loss of bone density and strength in adult female rats. *Bone* **2000,** 27, (5), 639-45.

172. Dobnig, H.; Turner, R. T., Evidence that intermittent treatment with parathyroid hormone increases bone formation in adult rats by activation of bone lining cells. *Endocrinology* **1995,** 136, (8), 3632-8.

173. Burr, D. B.; Hirano, T.; Turner, C. H.; Hotchkiss, C.; Brommage, R.; Hock, J. M., Intermittently administered human parathyroid hormone(1-34) treatment increases intracortical bone turnover and porosity without reducing bone strength in the humerus of ovariectomized cynomolgus monkeys. *Journal of Bone and Mineral Research* **2001,** 16, (1), 157-65.

174. Sloan, A. V.; Martin, J. R.; Li, S.; Li, J., Parathyroid hormone and bisphosphonate have opposite effects on stress fracture repair. *Bone* **2010,** 47, (2), 235-40.

175. Grynpas, M. D.; Rey, C., The effect of fluoride treatment on bone mineral crystals in the rat. *Bone* **1992,** 13, (6), 423-9.

176. Fratzl, P.; Roschger, P.; Eschberger, J.; Abendroth, B.; Klaushofer, K., Abnormal bone mineralization after fluoride treatment in osteoporosis: a small-angle x-ray-scattering study. *Journal of Bone and Mineral Research* **1994,** 9, (10), 1541-9.

177. Bhatia, A.; Albazzaz, M.; Espinoza Orías, A. A.; Inoue, N.; Miller, L. M.; Acerbo, A.; George, A.; Sumner, D. R., Overexpression of DMP1 accelerates mineralization and alters cortical bone biomechanical properties in vivo. *Journal of the Mechanical Behavior of Biomedical Materials* **2012,** 5, (1), 1-8.

178. Fratzl, P.; Schreiber, S.; Roschger, P.; Lafage, M. H.; Rodan, G.; Klaushofer, K., Effects of sodium fluoride and alendronate on the bone mineral in minipigs: a small-angle X-ray scattering and backscattered electron imaging study. *Journal of Bone and Mineral Research* **1996,** 11, (2), 248-53.

179. Mercurio, A. D.; Motta, T.; Green, E.; Noble, G.; Hart, R. T.; Allen, M. J., Effects of extensive circumferential periosteal stripping on the microstructure and mechanical properties of the murine femoral cortex. *Journal of Orthopaedic Research* **2012,** 30, (4), 561-568.

180. Kalu, D. N., The ovariectomized rat model of postmenopausal bone loss. *Bone and Mineral* **1991,** 15, (3), 175-191.

181. Ito, M.; Nishida, A.; Koga, A.; Ikeda, S.; Shiraishi, A.; Uetani, M.; Hayashi, K.; Nakamura, T., Contribution of trabecular and cortical components to the mechanical properties of bone and their regulating parameters. *Bone* **2002,** 31, (3), 351-358.

182. Miller, L. M.; Dumas, P., Chemical imaging of biological tissue with synchrotron infrared light. *Biochimica et Biophysica Acta (BBA) - Biomembranes* **2006,** 1758, (7), 846-857.

183. Miller, L. M.; Smith, R. J., Synchrotrons versus globars, point-detectors versus focal plane arrays: Selecting the best source and detector for specific infrared microspectroscopy and imaging applications. *Vibrational Spectroscopy* **2005,** 38, (1-2), 237-240.

184. Nguyen, T. Computational tools for the Fourier transform infrared (FT-IR) spectroscopic imaging. University of Illinois at Urbana-Champaign, 2012.

185. Levin, A.; Weiss, Y.; Durand, F.; Freeman, W. T., Understanding Blind Deconvolution Algorithms. *Pattern Analysis and Machine Intelligence, IEEE Transactions on* **2011,** 33, (12), 2354-2367.

186. Fish, D. A.; Brinicombe, A. M.; Pike, E. R.; Walker, J. G., Blind deconvolution by means of the Richardson?Lucy algorithm. *Journal of the Optical Society of America A* **1995,** 12, (1), 58-65.

187. Idris, A.; Rojas, J.; Greig, I.; van't Hof, R.; Ralston, S., Aminobisphosphonates Cause Osteoblast Apoptosis and Inhibit Bone Nodule Formation In Vitro. *Calcified Tissue International* **2008,** 82, (3), 191-201.

188. Orriss, I. R.; Key, M. L.; Colston, K. W.; Arnett, T. R., Inhibition of osteoblast function in vitro by aminobisphosphonates. *Journal of Cellular Biochemistry* **2009,** 106, (1), 109-118.

189. Barbara, A.; Delannoy, P.; Denis, B. G.; Marie, P. J., Normal matrix mineralization induced by strontium ranelate in MC3T3-E1 osteogenic cells. *Metabolism* **2004,** 53, (4), 532-7.

190. Reszka, A. A.; Rodan, G. A., Mechanism of action of bisphosphonates. *Current Osteoporosis Reports* **2003,** 1, (2), 45-52.

191. McRae, R.; Lai, B.; Vogt, S.; Fahrni, C. J., Correlative microXRF and optical immunofluorescence microscopy of adherent cells labeled with ultrasmall gold particles. *Journal of Structural Biology* **2006,** 155, (1), 22-9.

192. Narayanan, K.; Srinivas, R.; Ramachandran, A.; Hao, J.; Quinn, B.; George, A., Differentiation of embryonic mesenchymal cells to odontoblast-like cells by overexpression of dentin matrix protein 1. *Proceedings of the National Academy of Sciences* **2001,** 98, (8), 4516-4521.

193. He, G.; Dahl, T.; Veis, A.; George, A., Nucleation of apatite crystals in vitro by self-assembled dentin matrix protein 1. *Nature Materials* **2003,** 2, (8), 552-558.

194. Davis, J.; Cook, N. D.; Pither, R. J., Biologic mechanisms of 89SrCl2 incorporation into type I collagen during bone mineralization. *J Nucl Med* **2000,** 41, (1), 183-8.

Appendix A. IR measurement considerations

MCT detector responsivity

The responsivity and spectral response range of commonly used IR detectors are shown in Figure 7-1. For imaging of biological specimens, MCT detectors provide a suitable spectral response range with sufficient sensitivity. To accurately measure the IR spectrum of bone in the far and mid-IR range, a bolometer and GeCu detector were used to supplement mid-IR measurements from a MCT detector with far-IR measurements.

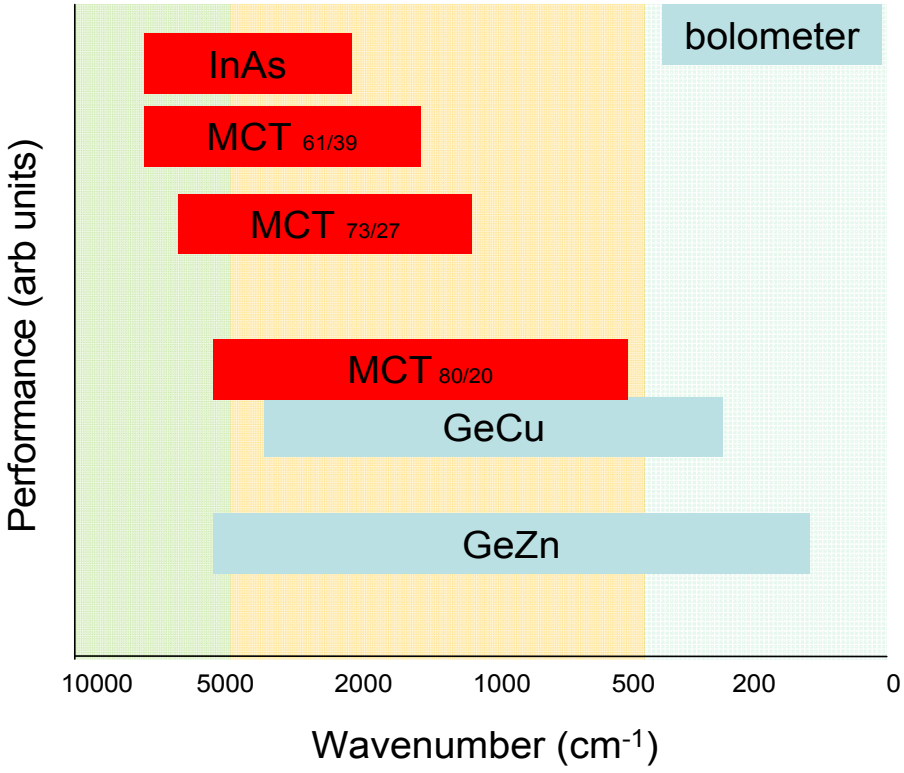

Figure 7-1: Responsivity and spectral response range of commonly used IR detectors. MCT detectors are commonly used in the imaging of biological specimens as it covers the spectral range of biologically relevant vibrational modes, such as phosphates and amides (protein).

MCT non-linearity

Aside from detector sensitivity and spectral response range, detector non-linearity should be carefully considered if the magnitude of the response between sample and reference, or between samples is drastically different. Ideally, the sample and reference response are as close as possible. To illustrate, Figure shows that the reflectivity of gold is near 100%, while KRS-5 reflects 17% and CsI reflects 6%. With a specimen reflectivity of 3% for bone, the ideal reference material is thus CsI.

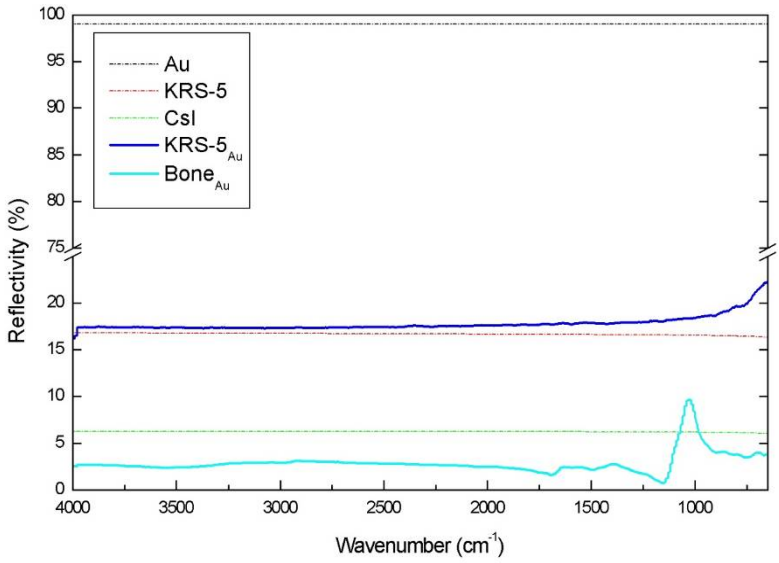

Figure 7-2: MCT response illustrated using materials with low, medium and high reflectivity. Dotted lines are theoretical values, solid lines are measured values. Due to small non-linearities, a highly reflective material is not suitable as a reference material for bone specimens.

IR polarization

In most reflectance measurements where the Kramers-Kronig transform is used to obtain optical properties of a material, the polarization of IR light should be predominantly s-polarized. The polarization at the sample stage of beam line u2b is nearly 90%.

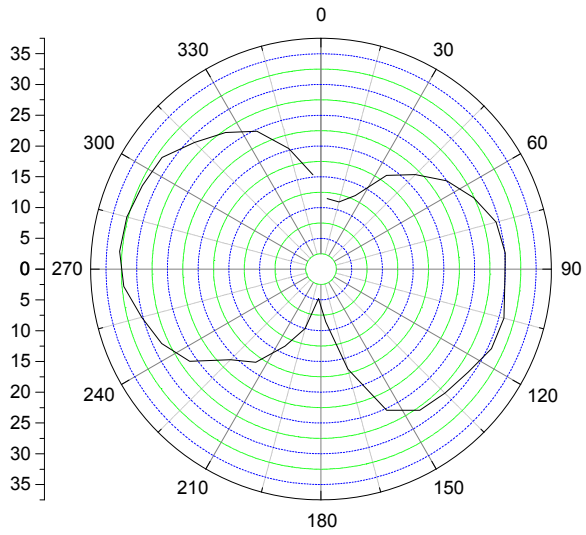

Figure 7-3: Polar plot of the IR polarization at the sample location of beamline U2b. Polarization is greatest at 100 and 280 °.

Appendix B. IR spectral appending implementation

Retrieval of Spectral Data from OPUS into MATLAB

The transfer of spectral data from OPUS to MATLAB occurs via the Windows Dynamic Data Exchange (DDE) protocol using custom written MATLAB code. Initiating of a communication session involves setting up a DDE channel as shown in lines 1-8. Afterwards, various settings related to the transfer of data are set, including word length, transfer mode, floating point precision. In the example on lines 9-12, the data transfer mode is set to binary.

```
Initiate DDE channel with OPUS
 1 disp('Initiating DDE conversation with OPUS ... ')
 2 channel = ddeinit('OPUS','OPUS|System');
 3 if (channel == 0)
 5     error('Could not establish DDE channel link with OPUS');
 6 else
 7     disp([char(8) 'OK'])
 8 end
```

```
Sets transfer mode to BINARY (or ASCII)
 9 item = 'BINARY';
10 disp(['Setting transfer mode to ' item  ' ... '])
11 out = ddereq(channel, item, [1,1]);
12 CheckResult(out, output);
```

With similar logic, DDE commands from MATLAB instruct OPUS to load a specific data file, read header information and finally transmit specific spectral information to MATLAB. The maximum size per DDE request is limited to less than 512 Kbytes (line 2), but the total amount of spectral data that is to be transferred is on the order of 50 to 100 Mbytes (line 3). As such, the spectral data is retrieved from OPUS by several small DDE requests (by line 4-7). A for-loop is used to retrieve the spectral data using the DDE session (lines 9-16), and is stored in a pre-allocated output array. Finally, a frequency column is added to the data array (lines 18-19).

```
Read 3D data
 1 disp('Reading data ... ')
 2 ddesize = 100;
 3 total = str2num(NPX)*str2num(NPY);
 4 num_ddereq = (total - mod(total, ddesize)) / ddesize;
 5 arr(1) = 0;
 6 arr(2:num_ddereq+1) = (1:num_ddereq) * ddesize;
 7 arr(num_ddereq+2) = (num_ddereq * ddesize) + mod(total, ddesize);
 8
 9 for k = 1:num_ddereq+(~(mod(total, ddesize) == 0))
10     item = ['READ_DATA * ',num2str(arr(k)+1),'-',num2str(arr(k+1))];
11     out = ddereq(channel, item, [1,0]);
12     out = out(8:end-1);
13     out = reshape(out, str2num(NPT)+1, arr(k+1)-arr(k));
14     out = out(2:end,:);
15     data(:,arr(k)+1:arr(k+1)) = out;
16 end
17
18 data(:,2:total+1) = data(:,:);
19 data(:,1) = FREQHI:-(FREQHI-FREQLO)/NPT:FREQLO;
19 disp([char(8) 'OK'])
```

Appending far-IR Spectral Data to Sample Spectra

The procedure to append a-priori far-IR spectral data to the sample spectral data in the mid-IR domain involves first normalizing the data spacing to 1 cm^{-1}. The data structure is a 2-dimensional array, with column 1 holding the spectral frequency information and columns 2 to the end holding spectral data. Spectral frequency normalization is performed using the MATLAB interp1 command on the first column, using FREQ_RES as the target data spacing with upper and lower boundaries FREQ_LO and FREQ_HI.

Normalize data spacing to 1 cm^{-1}

```
1 data_normalized = interp1(data(:,1), data, FREQ_LO:FREQ_RES:FREQ_HI);
2 data_normalized(:,1) = int16(data_normalized(:,1));
```

The intensities of several key locations on the specimen spectrum are used to translate and scale the template spectrum. In a series of steps, peaks are located and their height calculated. As an example, the following pseudocode finds the phosphate peak location and height located at approximately 1025 cm^{-1} in the reflection spectrum:

Find location and height of phosphate peak (max @ ~1025 cm^{-1})

```
1 p0900_relative = find(spectrum >= 0900, 1, 'first');
2 p1300_relative = find(spectrum >= 1300, 1, 'first');
3 [C I] = max(spectrum( p0900_relative : p1300_relative , 2));
4 p1025_absolute = I + p0900_relative - 1;
5 p1025_absolute_height = mean(spectrum(p1025_absolute-
1:p1025_absolute+1,2));
```

The specimen and template spectrum overlap over the spectral range from 850 to 900 cm^{-1}. To ensure a smooth continuation between the two spectra, spectral data from both spectra are taken into account using a weighted average with respect to spectral frequency. In lines 1-4, the indices for 850 and 900 cm^{-1} are found for both the specimen and template spectra.

Compute 850-900 overlap region … [0…1]*sample + [1…0]*template

```
 1 template_p0850_relative = find(template(:,1) >= 0850, 1, 'first');
 2 template_p0900_relative = find(template(:,1) >= 0900, 1, 'first');
 3 specimen_p0850_relative = find(specimen(:,1) >= 0850, 1, 'first');
 4 specimen_p0900_relative = find(specimen(:,1) >= 0900, 1, 'first');
 5
 6 overlap1 =templt(templat_p0850_relatv:templt_p0900_relatv,2:end);
 7 scaling1 = repmat((1:-1/(size(overlap1,1)-1):0)', 1, NPXY-1);
 8 overlap1_scaled = overlap1 .* scaling1;
 9
10 overlap2 =specimen(specimn_p0850_relatv:specimn_p0900_relatv,2:end);
11 scaling2 = repmat((0: 1/(size(overlap2,1)-1):1)', 1, NPXY-1);
12 overlap2_scaled = overlap2 .* scaling2;
13 overlap = overlap1_scaled + overlap2_scaled;
```

A graphical representation of the appending procedure is displayed in Figure and Figure , the template bone spectrum (blue) is scaled and translated to match the specimen spectrum. Afterwards, the overlap region is computed and the final, extended spectrum is constructed.

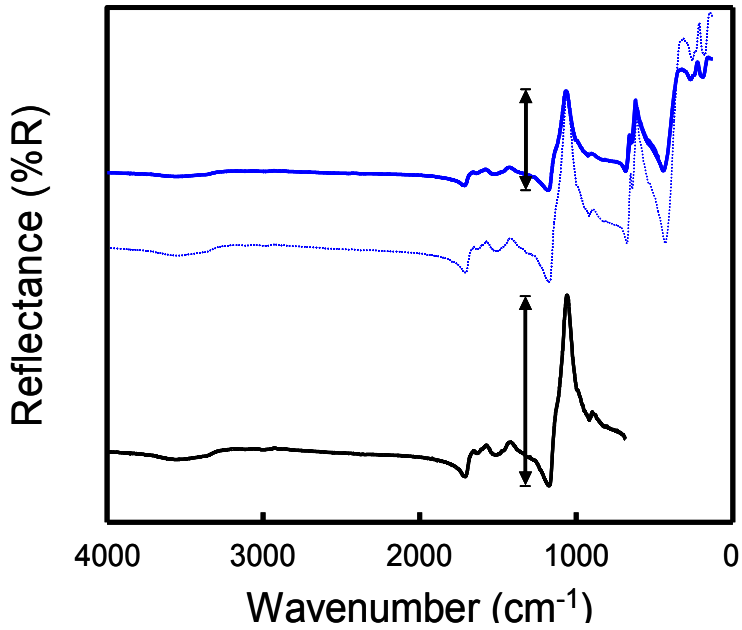

Figure 7-4: The template bone spectrum (solid blue) is scaled so that the range between the maximum and minimum of the v_1v_3 PO_4^{3-} peak (indicated by black arrows) matches that of the target bone spectrum (black). The result is a scaled template bone spectrum (dotted blue).

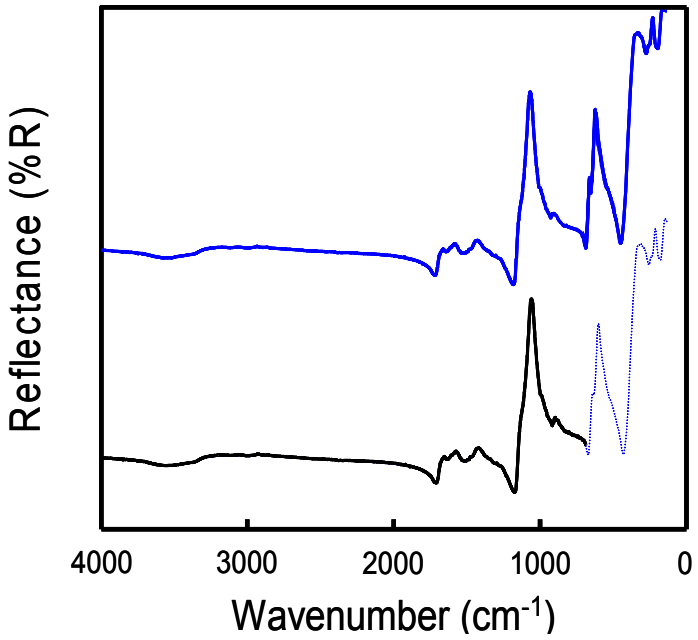

Figure 7-5: The scaled template bone spectrum (solid blue) is translated to overlap the target bone spectrum (black), based on the height of the baseline between 4000 and 2500 cm^{-1}. Then the template bone spectrum is truncated from 850 - 70 cm^{-1}. The target bone spectrum is then extended (dotted blue) with the now scaled and translate template bone spectrum. The 900 - 850 - cm^{-1} regions of both the target bone spectrum and template bone spectrum are averaged and used in the final extended bone spectrum.

In the case were the farIR (bolometer and Cu:Ge detectors) and midIR (MCT detector) spectra are collected from the same location on a single specimen, the spectra should already align and as such no scaling and translating is required. This is demonstrated in Figure where farIR and midIR spectra appear to overlap, and no significant corrections are required to merge the spectra into a full, extended spectrum.

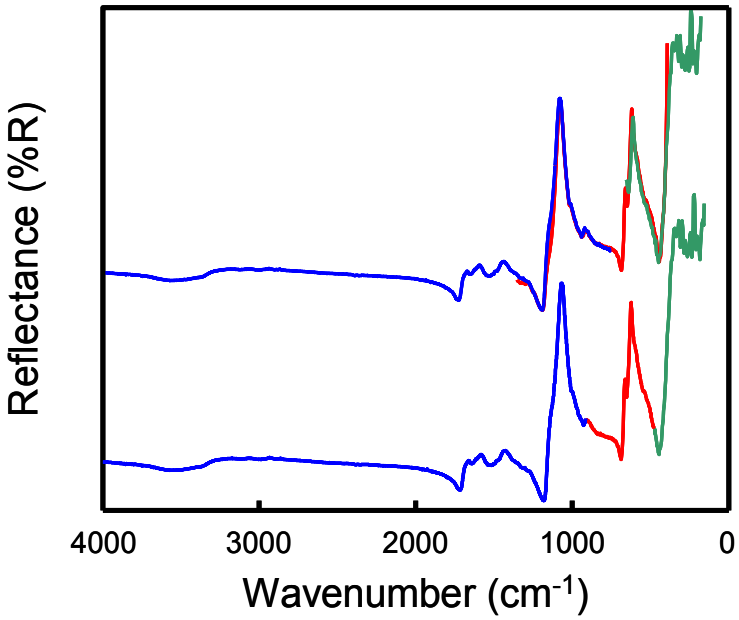

Figure 7-6: Top: Three overlapping spectra from the same spot on a mature mouse femur taken with a bolometer (green), Cu:Ge (red) and MCT detector (blue). Bottom: The three individual spectra were truncated to remove overlapping ends, and were subsequently appended into a single spectrum spanning 4000 - 70 cm^{-1}. No corrections were necessary for appending these spectra.

Appendix C. IR Automated Region-of-Interest

Noise Removal in Integration Maps

A MATLAB program was written for the automated, unbiased placement of regions of interest onto IR integration maps. The input is in the form of a collection of HDF files, each containing an individual integration map. Based on the mineralization map, all input are filtered to remove noise. First, a structured element is used to perform the mathematical erode function, which effectively removes noisy pixels that are not part of the cortical bone (line 1-2). Afterwards, the bwareaopen function is used to remove any isolated objects that have fewer than 5000 pixels, such as small fragments of bone that are isolated and distance from the cortical shell, or parts of a subsequent specimen that may be in view (line 3). The result is then inverted and a second bwareaopen call is made, but this time on objects small than 50 pixels (lines 4-5). This step effectively removes small resorption cavities that may be present within the intracortical region of the cortical shell. Then result is again inverted and dilated, thereby reverting the size of the cortical shell back what it was originally (lines 6-7).

```
Clean up integration maps
1 se = strel('square', 5);
2 image = imerode(image, se);
3 image = bwareaopen(image,5000);
4 image = not(image);
5 image = bwareaopen(image,50);
6 image = not(image);
7 image = imdilate(image, se);
```

Resolving the Orientation of the Cortical Shell

In order to place regions of interest in each quadrant of the cortical shell, its orientation needs to be resolved. In this process, a custom written, automated MATLAB program uses the binary integration maps that were previously cleaned from noise. First, the MATLAB function regionprops is used to determine the centroid of the cortical shell (lines 1-4). Also, the outer circumference of the cortical shell is determined using the MATLAB bwboundaries function (lines 6-7). From there, the distance from the centroid to the outer circumference is determined as a function of angle (lines 9-12). The shape of the graph plotting this distance as a function of angle is then used to determine the orientation of the cortical shell. More specifically, the angle at which this distance is greatest is defined as the lateral quadrant. Manual refinement of the orientation is possible.

```
Calculate Cortical Shell Orientation
 1 s = regionprops(double(image), 'Centroid');
 2 centroid = cat(1, s.Centroid);
 3 x = round(centroid(1));
 4 y = round(centroid(2));
 5
 6 bound = bwboundaries(image);
 7 outer = bound[100];
```

```
 8
 9 outer_count = size(outer, 1);
10 for i=1:outer_count
11   [outer(i,3) outer(i,4)] = get_angdist4(x, y, outer(i,2), outer(i,1));
12 end
13
14 outer = sortrows(outer,4);
15 angle = outer(end,3);
16 angle = 360 - (angle * 180/pi) + 110;
17 RI = imrotate(image, angle);
```

Placement of Regions of Interest

Due to the varying shape of the cortical shell from specimen to specimen, a MATLAB program was developed to automatically place rectangular regions of interest into specific locations of the cortical shell. With the cortical shell being several hundred microns in diameter, seven zones were defined to divide the width cortical shell (line 1). The outer edge zones *E* were defined to be 50 μm each. The five remaining zones were alternates of three rectangles with a width *W* of 100 μm and two spacer zones filling with a width *M* defined by the remaining cortical width (line 2). The angular orientation of the three rectangles were defined by the angle of the nearest surface; the angle of the outer two rectangles was set to the angle of their respective surface, while the angle of the remaining rectangle was set to the average angle of both surfaces (lines 3-10).

Placement of a Region of Interest in the Posterior Periosteum

```
 1 width_of_bone = edge2 - edge1;
 2 M = (width_of_bone - (3*W+2*E))/2;
 3 [angle_x3, distance] = get_angdist( x3a, y+H/2, x3b, y-H/2 );
 4 [angle_x4, distance] = get_angdist( x4a, y+H/2, x4b, y-H/2 );
 5 angle_x34 = (angle_x3+angle_x4)/2;
 6 diagonal = sqrt( (W/2)^2 + (H/2)^2 );
 7 cub_angle.tr = atand( (W/2)  / (H/2)  );
 8 cub_angle.br = 180 - cub_angle.tr;
 9 cub_angle.bl = 180 + cub_angle.tr;
10 cub_angle.tl = 360 - cub_angle.tr;
```

Appendix D. Small and Wide Angle X-ray Scattering Analysis

Data Processing of Raster Scanned SAXS and WAXS Patterns

The raster scanning of bone thin sections using simultaneous SAXS and WAXS detectors produced individual SAXS and WAXS image files per point on the raster scanned specimen. The file naming convention included the x- and y-location of individual patterns. Although data analysis software is available for the analysis of SAXS and WAXS patterns, the analysis is large manual and does not include specific analysis strategies that were required for this project. As such, a MATLAB program was custom written to read in and analyze SAXS and WAXS patterns in an automated fashion. Using a for-loop, all SAXS and WAXS patterns in a user defined directory were analyzed, according to the following code (lines 1-10). The x- and y-location of individual patterns were read out using a regular expression (line 5).

Extracting spatial location of individual scattering patterns

```
 1 files_list = dir([folder '\*_SAXS']);
 2
 3 for i=1:num_files
 4   file  = files_list(i).name;
 5   [a b] = regexp(file, '[-]?\d\d?(.)\d{1}', 'start', 'end');
 6   x_loc = str2num(file(a(1):b(1)));
 7   x_r   = round(((x_loc - x_min) / x_step) + 1);
 8   z_loc = str2num(file(a(2):b(2)));
 9   z_r   = round(((z_loc - z_min) / z_step) + 1);
10 end
11
12 call to SAXS analysis function
13 call to WAXS analysis function
```

SAXS Pattern Analysis

Analysis of SAXS patterns did not require specialized transformations, as the SAXS camera was oriented perpendicular to and centered on the incident beam. The analysis involved the conversion of SAXS patterns plotted on a polar coordinate system to a 2-dimensional intensity plot of angle ψ versus q. Two strategies were identified, namely the "direct mapping" of individual pixels in the SAXS pattern to their corresponding location in the 2-dimensional array, and the "lookup mapping", where the intensity of points in the 2-dimensional array are back calculated based on the SAXS pattern (Figure). While the first approach unavoidably has empty pixels in the low q region due to the low angular resolution ψ, the second approach does a better job at producing a "clean" image. However, since the second approach does not correctly conserves the "amount" of scattering, this approach can lead to inaccuracies in later steps. As such, the "direct mapping" approach was used.

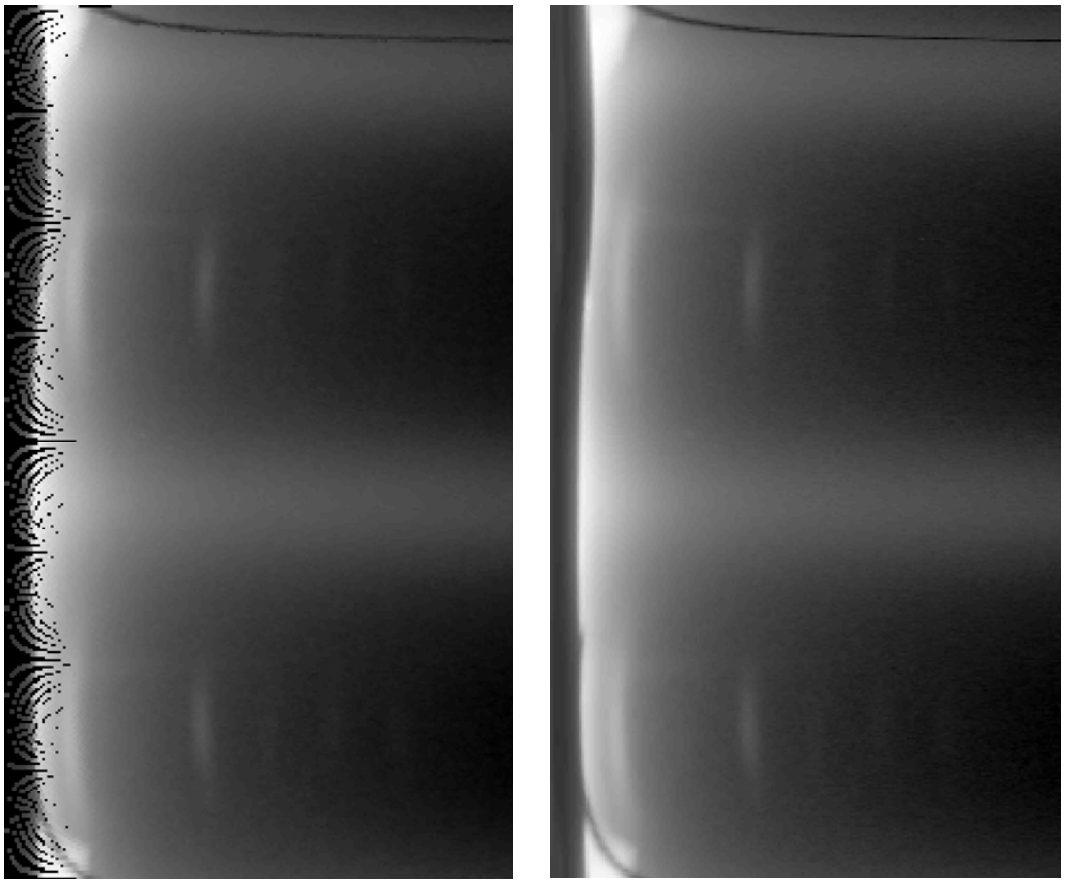

Figure 7-7: Comparison of "direct mapping" and "lookup mapping" strategies in the conversion of SAXS patterns plotted on a polar coordinate system to Cartesian coordinates.

The SAXS patterns plotted on a Cartesian coordinate system are readily integrated over either axis to produce plots of I(ψ) and I(q). In the I(ψ) plot, the predominant orientation of the collagen fibrils can be determined by the angle of the peak maximum. Two peak maxima offset by 180° are searched, and their angular location is a direct estimate of the orientation of the collagen fibrils. In a second step, the area between the peaks and the baseline formed by the peak minima is ratioed to the total integrated area of the I(ψ). This value between 0 and 1 indicates the degree of orientation, with values closer to 1 indicating highly aligned collagen.

The plot of I(q) is used to calculate the *D*-spacing of the collagens within collagen fibrils. In order to amplify the strength of the signal, the intensity is multiplied byq^2 to produce a plot of I(q) * q^2. A cubic spline is first fit, spanning both edges of the 3rd harmonic but not the peak itself (lines 1-5). The spline is then subtracted from the data (lines 7-9).

Fitting of a piecewise cubic spine to the 3rd harmonic collagen peak

```
1 xc = [sx(loc1) sx(loc2) sx(loc3) sx(loc4) sx(loc5) sx(loc6)];
2 yc = [sy(loc1) sy(loc2) sy(loc3) sy(loc4) sy(loc5) sy(loc6)];
3 con = struct('xc',xc,'yc',yc);
4 p = splinefit(sx,sy,3,con);
5 f = ppval(p,sx);
6
7 y_diff = sy-f;
8 xi = min(sx):0.00001:max(sx);
9 yi = interp1(sx,y_diff,xi,'spline');
```

Afterwards, a peak search finds the q-location of the peak, which is converted to nanometers using Bragg's law.

WAXS Pattern Analysis

Prior to the analysis, WAXS patterns should be corrected for detector tilt and roll, as described in Chapter 5.7. Afterwards, the patterns are radially transformed into 2-dimensional matrix plotting I(q) versus q. The accuracy of the detector tilt and roll correction is easily verified in this plot, as diffraction lines from either the standard of specimen should appear perfectly vertical (Figure).

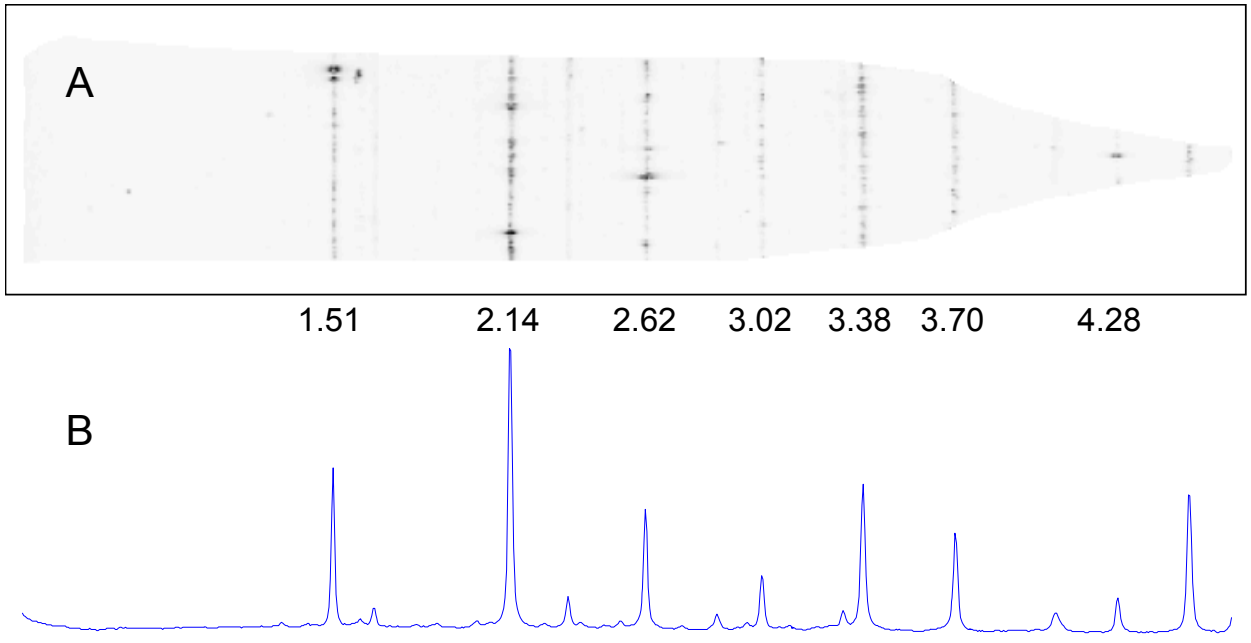

Figure 7-8: (A) The transformed, 2-dimensional WAXS plot showing vertical scattering lines at q-ranges associated with the standard LaB_4. (B) Integration of A showing distinct peaks and a flat baseline.

The MATLAB pseudocode that implements the above radial integration first calculates the minimum and maximum q-values that the WAXS pattern holds (lines 1-4). Afterwards, a 2-dimensional array is pre-allocated with the x-dimension accounting for the q-range and q-resolution and the y-dimension containing 360 degree increments (line 5). The main portion of the routine involves re-assigning pixels from the WAXS pattern into this 2-dimensional array. To

accomplish this, the angle and q-value for each pixel in the WAXS pattern is first calculated (lines 9-19). Subsequently, based on the angle and q-value fractions the total intensity of that pixel is subdivided into a 2 x 2 array and added into the 2-dimensional array (lines 21-29).

WAXS transform to q versus ψ

```
 1 theta = 0.5 * atand( distance ./ (WAXS_Dd*sizeX - pattern) );
 2 pattern = (4*pi/WAXS_lambda) .* sind(theta);
 3 q_min = min(WAXS_pattern);
 4 q_max = max(WAXS_pattern);
 5 IvQ_array = zeros( 360 , q-range and resolution );
 6
 7 [intensity, q-value] = WAXS_pattern;
 8
 9 angle_lo = floor(angle(i));
10 angle_hi = angle_lo + 1;
11 q_lo_ind = floor(q/qbin);
12 q_hi_ind = q_lo_ind + 1;
13 q_lo     = qbin * q_lo_ind;
14 q_hi     = q_lo + qbin;
15
16 angle_fraction_lo = angle(i) - angle_lo;
17 angle_fraction_hi = 1 - angle_fraction_lo;
18 q_fraction_lo     = (q_hi-q)/qbin;
19 q_fraction_hi     = 1 - q_fraction_lo;
20
21 IvQ_array(angle_lo,q_lo_ind) = IvQ_array(angle_lo,q_lo_ind) + value *
      (angle_fraction_lo*q_fraction_lo);
22 IvQ_array(angle_lo,q_hi_ind) = IvQ_array(angle_lo,q_hi_ind) + value *
      (angle_fraction_lo*q_fraction_hi);
23 IvQ_array(angle_hi,q_lo_ind) = IvQ_array(angle_hi,q_lo_ind) + value *
      (angle_fraction_hi*q_fraction_lo);
24 IvQ_array(angle_hi,q_hi_ind) = IvQ_array(angle_hi,q_hi_ind) + value *
      (angle_fraction_hi*q_fraction_hi);
25
26 weight_array(angle_lo,q_lo_ind) = weight_array(angle_lo,q_lo_ind) +
      (angle_fraction_lo*q_fraction_lo);
27 weight_array(angle_lo,q_hi_ind) = weight_array(angle_lo,q_hi_ind) +
      (angle_fraction_lo*q_fraction_hi);
28 weight_array(angle_hi,q_lo_ind) = weight_array(angle_hi,q_lo_ind) +
      (angle_fraction_hi*q_fraction_lo);
29 weight_array(angle_hi,q_hi_ind) = weight_array(angle_hi,q_hi_ind) +
      (angle_fraction_hi*q_fraction_hi);
```